ANGULAR ACCELERATION ASSISTED STABILIZATION OF A 2-DOF GIMBAL PLATFORM

A THESIS SUBMITTED TO
THE GRADUATE SCHOOL OF NATURAL AND APPLIED SCIENCES
OF
MIDDLE EAST TECHNICAL UNIVERSITY

BY

TAHA ÖZTÜRK

IN PARTIAL FULFILLMENT OF THE REQUIREMENTS
FOR
THE DEGREE OF MASTER OF SCIENCE
IN
ELECTRICAL AND ELECTRONICS ENGINEERING

SEPTEMBER 2010

Approval of the thesis:

ANGULAR ACCELERATION ASSISTED STABILIZATION OF A 2-DOF GIMBAL PLATFORM

submitted by **TAHA ÖZTÜRK** in partial fulfillment of the requirements for the degree of **Master of Science in Electrical and Electronics Engineering Department, Middle East Technical University** by,

Prof. Dr. Canan Özgen _____
Dean, Graduate School of **Natural and Applied Sciences**

Prof. Dr. İsmet Erkmen _____
Head of Department, **Electrical and Electronics Engineering**

Prof. Dr. Kemal Leblebicioğlu _____
Supervisor, **Electrical and Electronics Engineering Dept., METU**

Examining Committee Members:

Prof. Dr. Aydan M. Erkmen
Electrical and Electronics Engineering Department, METU _____

Prof. Dr. Kemal Leblebicioğlu
Electrical and Electronics Engineering Department, METU _____

Prof. Dr. M. Kemal Özgören
Mechanical Engineering Department, METU _____

Asst. Prof. Yiğit Yazıcıoğlu
Mechanical Engineering Department, METU _____

Bülent Bilgin, M. Sc.
Manager, Unmanned Systems Department, ASELSAN _____

Date: _____

I hereby declare that all information in this document has been obtained and presented in accordance with academic rules and ethical conduct. I also declare that, as required by these rules and conduct, I have fully cited and referenced all material and results that are not original to this work.

Name, Last Name: TAHA ÖZTÜRK

Signature :

ABSTRACT

ANGULAR ACCELERATION ASSISTED STABILIZATION OF A 2-DOF GIMBAL PLATFORM

Öztürk, Taha
M.S., Department of Electrical and Electronics Engineering
Supervisor : Prof. Dr. Kemal Leblebicioğlu

September 2010, 168 pages

In this thesis work construction of the angular acceleration signal of a 2-DOF gimbal platform and use of this signal for improving the stabilization performance is aimed. This topic can be divided into two subtopics, first being the construction of angular acceleration and the second being the use of this information in a way to improve system performance. Both problems should be tackled in order to get satisfactory results. The most important output of this work is defined as the demonstration of the improvements obtained both theoretically and on experimental setup. Although the system to be studied is a two axis gimbal platform, the results obtained can be applied to other servo control problems. It is possible to define different performance criteria for a servo control problem and different techniques will be addressed with different control objectives. For this thesis work, the performance criterion is defined as the stabilization performance of the platform. As a result, disturbance rejection characteristics of the controller emerges as the main topic and methods for rejecting these disturbances such as the friction torques and externally applied moments are focused on throughout the studies. As expected, remarkable improvement is achieved

as a result of the use of acceleration feedback.

Keywords: acceleration feedback, angular acceleration measurement, platform stabilization, disturbance rejection, Kalman filtering

ÖZ

İKİ SERBESTLİK DERECELİ BİR PLATFORMUN AÇISAL İVME DESTEKLİ STABİLİZASYONU

Öztürk, Taha
Yüksek Lisans, Elektrik ve Elektronik Mühendisliği Bölümü
Tez Yöneticisi : Prof. Dr. Kemal Leblebicioğlu

Eylül 2010, 168 sayfa

Bu çalışmada iki serbestlik dereceli bir platformun ivme bilgisinin üretilmesi ve bu bilginin stabilizasyon performansını iyileştirmede kullanılması hedeflenmiştir. Bu konu iki ana başlık altında değerlendirilebilir; ivme bilgisinin gereken kalitede üretilmesi ve bu bilginin performansı arttıracak şekilde kullanılabilmesi. Her iki problemin de ayrı ayrı çözülmesi ve elde edilen çözümlerin birlikte kullanılması iyileşme elde edilmesi açısından gereklidir. Yapılacak çalışmalarda ortaya çıkacak sonuçların gerçek sistem üzerinde doğrulanmasın ve hedeflenen iyileşmelerin gerçek sistem üzerinde görülebilmesin bu çalışmanın en önemli sonuçlarından biri olması gerektiği kabul edilmiştir. Üzerinde çalışılan sistem iki serbestlik dereceli bir platform olsa da elde edilecek sonuçların diğer servo kontrol problemlerine de kolayca uygulanabileceği sonucuna varılmıştır. Yukarıda tanımlanan iki serbestlik dereceli platformun kontrolü için çeşitli performans ölçütleri tanımlanabileceği ve farklı performans ölçütleri için iyileştirme yöntemlerinin farklılık göstereceği görülmüştür. Bu çalışmada performans kriteri olarak sistemin stabilizasyon performansı kabul edilmiştir. Bunun sonucu olarak sistemin bozucu etki düzeltme karakteristiği önem kazanmıştır. Beklendiği

gibi ivme geri beslemesi sonucunda stabilizasyon hassasiyetinde önemli iyileşme sağlanmıştır.

Anahtar Kelimeler: ivme geribeslemesi, açısal ivme ölçümü, platform stabilizasyonu, bozucu etki giderme, Kalman filtreleme

To My Family

ACKNOWLEDGMENTS

I wish to express my deepest gratitude to my supervisor Prof. Dr. Kemal Leblebicioğlu for his helpful criticism, guidance and patience in the progress and preparation of this thesis.

I would like to express my thanks to my friends and colleagues for their support and fellowship.

I appreciate the support and facilities provided by ASELSAN for the completion of this thesis, especially in the application of experimental studies that would otherwise be impossible.

I would also like to thank TÜBİTAK for its support on scientific and technological research.

Finally, I wish to express my special thanks and gratitude to my mother Meral ÖZTÜRK, my father Cavit ÖZTÜRK, and my sister Merve ÖZTÜRK for their help and support not only during my thesis preparation but also throughout my life.

TABLE OF CONTENTS

ABSTRACT iv

ÖZ vi

ACKNOWLEDGMENTS ix

TABLE OF CONTENTS x

LIST OF TABLES xv

LIST OF FIGURES xvi

LIST OF SYMBOLS xxiii

LIST OF ABBREVIATIONS xxvi

CHAPTERS

1 INTRODUCTION 1

1.1 Background and Motivations 1

1.2 Objectives and Contributions of the Thesis 5

1.3 Outline of the Thesis 5

2 THEORETICAL BACKGROUND 7

2.1 Construction of Inertial Angular Acceleration Information of a Platform 7

2.1.1 Preliminaries on Kinematics and Acceleration in 3-D Space 9

2.1.2 Determination of Angular Velocity and Angular Acceleration of a Body From Linear Accelerometer Readings 11

2.1.3 Method Used in this Thesis Work 17

2.2 Mathematical Model of the 2-DOF Gimbal Platform Including Base Disturbances 19

2.2.1 Simplification of the Mathematical Model 28

2.2.1.1 Validation of the Uncoupled Rotation Axes Assumption 28

2.2.1.2 Simplification of the Azimuth Axis Equation of Motion 33

2.2.1.3 Simplification of the Elevation Axis Equation of Motion 36

2.3 Preliminaries on Kalman Filtering 39

2.3.1 The Discrete Time Kalman Filter 40

2.4 On the Use of Acceleration Information in Servo Control Applications 42

2.4.1 Definition of the Standard Controller and Overview of Expectations from Using Acceleration Feedback 42

2.4.2 Load Torque Estimator 46

2.4.3 Inner Acceleration Loop Method 49

2.4.4 State Derivative Feedback LQR Method 51

3 MODELING, SIMULATION AND CONTROL USING ACCELERATION FEEDBACK 57

3.1 Identification of the Parameters of the 2-DOF Gimbal Platform 58

3.1.1 Identification of the Azimuth and Elevation Axis Plant Transfer Functions 59

3.1.1.1 Azimuth Axis Plant Bode Plot 60

3.1.1.2 Elevation Axis Plant Bode Plot 61

3.1.2 Identification of the Azimuth and Elevation Axis Inertial Parameters 61

3.1.2.1 Azimuth Axis Inertial Parameters . . . 62

3.1.2.2 Elevation Axis Inertial Parameters . . 62

3.1.2.3 Correction of Inertia Values Using Information Obtained from Bode Plots . 62

3.1.3 Identification of Azimuth and Elevation Axis Friction Torques 63

3.1.3.1 Azimuth Axis Friction Torque 64

3.1.3.2 Elevation Axis Friction Torque 65

3.1.4 Identification of ”‘Friction to System Inertia Ratio”’ as an Important Parameter for Stabilized Platforms 66

3.2 Sensor Fusion and Filtering 67

3.2.1 Identification of the Amount of Sensor Noise for Sensors Used 67

3.2.2 Analysis of Validity Conditions for Kalman Filter Optimality 68

3.2.3 Implementation and Tuning of the Kalman Filter Used 72

3.2.4 Assessment of Feedback Quality Improvement Achieved with the Additional Measurement of Angular Acceleration 77

3.3 Construction of the Simulation Model 81

3.3.1 A Review of SimMechanics Blockset 82

3.3.2 Mechanical Bodies 84

3.3.3 Friction 85

3.3.4 Sensor Noise and Delay 86

3.3.5 Motor and Driver Dynamics 87

3.3.6 Compliances in Mechanical Structure 88

3.3.7 6-DOF Motion Simulator 90

3.4 Controller Implementation and Tuning 92

3.4.1 Standard Controller 93

3.4.1.1 Azimuth Axis 93

3.4.1.2 Elevation Axis 94

3.4.2 Controller With Load Torque Estimator 94

3.4.2.1 Azimuth Axis 95

3.4.2.2 Elevation Axis 95

3.4.3 Controller with Inner Acceleration Loop 96

3.4.3.1 Azimuth Axis 96

3.4.3.2 Elevation Axis 97

3.4.4 State Derivative Feedback LQR 97

3.4.4.1 Azimuth Axis 98
3.4.4.2 Elevation Axis 98
3.5 Simulation Test Results 100
3.5.1 Azimuth Axis Tests 101
3.5.1.1 The Standard Controller 101
3.5.1.2 Controller with Load Torque Estimator 103
3.5.1.3 Controller with Inner Acceleration Loop 104
3.5.1.4 State Derivative Feedback LQR 106
3.5.2 Elevation Axis Tests 107
3.5.2.1 The Standard Controller 107
3.5.2.2 Controller with Load Torque Estimator 109
3.5.2.3 Controller with Inner Acceleration Loop 110
3.5.2.4 State Derivative Feedback LQR 112
3.5.3 Summary of the Simulation Test Results 113
4 EXPERIMENTAL WORK 115
4.1 Design of the Test Setup 115
4.1.1 Gimbal Mechanic 116
4.1.2 Motors 117
4.1.3 Motor Drivers 118
4.1.4 Rotary Sensors: Encoders 119
4.1.5 Inertial Sensors: Rate Gyros 120
4.1.6 Inertial Sensors: Accelerometer Array 120
4.1.7 Data Acquisition Hardware: Serial Interface Card . 121
4.1.8 Data Acquisition Hardware: Digital/Analog I/O Card 121
4.1.9 Real Time Control and Monitoring Hardware and Software 122
4.1.10 Mechanical Interface Parts 122
4.1.11 6-DOF Motion Simulator Platform 123
4.2 Experimental Method and Procedure 124

4.3 Experimental Results 128
4.3.1 Azimuth Axis Tests 128
4.3.1.1 The Standard Controller 129
4.3.1.2 Controller with Load Torque Estimator 133
4.3.1.3 Controller with Inner Acceleration Loop 136
4.3.1.4 State Derivative Feedback LQR Controller 139
4.3.2 Elevation Axis Tests 143
4.3.2.1 The Standard Controller 143
4.3.2.2 Controller with Load Torque Estimator 147
4.3.2.3 Controller with Inner Acceleration Loop 150
4.3.2.4 State Derivative Feedback LQR Controller 153
4.4 Conclusion 157
5 DISCUSSION, CONCLUSION AND FUTURE WORK 159
5.1 Discussion and Conclusion 159
5.2 Future Work 165
REFERENCES 166

LIST OF TABLES

TABLES

Table 3.1 Table showing the disturbances that are going to applied to the base of the gimbal in yaw and pitch directions in stabilization tests 101

Table 3.2 Table showing the standard deviation stabilization errors achieved with all four controllers for both axes under different disturbances 114

Table 4.1 Table showing some properties and limits of the 6-DOF motion simulator used throughout the experiments 125

Table 4.2 Table showing the standard deviation stabilization errors achieved with all four controllers for both axes under different disturbances 157

LIST OF FIGURES

FIGURES

Figure 1.1 ASELFLIR 300T Stabilized Electro Optic Platform Developed and Manufactured by ASELSAN 3

Figure 2.1 Position of a Point P Relative to a Moving Reference Frame [1] . . 9

Figure 2.2 Description of Rigid Body Motion Using Different Coordinate Frames 12

Figure 2.3 Coordinate Frames Used and Rotational Relations Between Those . 20

Figure 2.4 Important Unit Vector Directions on the 2-DOF Gimbal 21

Figure 2.5 Plant Azimuth Axis Block Diagram 35

Figure 2.6 Plant Elevation Axis Block Diagram 39

Figure 2.7 Timeline Showing *a priori* and *a posteriori* State Estimates and Estimation Error Covariances [14] 41

Figure 2.8 Overall System Block Diagram, Plant and Controller Combined. . . 43

Figure 2.9 Driver and Motor Dynamics Combined in a Single Transfer Function 43

Figure 2.10 Block Diagram After the Motor-Controller Simplification 44

Figure 2.11 Control Structure With Speed Controller and Load Torque Estimator 47

Figure 2.12 Block Diagram Showing the Effective Result of Using a Load Torque Estimator to Compensate Disturbance Torques 49

Figure 2.13 Control Structure With Cascaded Speed and Acceleration Loops . . 50

Figure 2.14 Terms Involved in the Dynamic Stiffness Expression and the Effects of Increasing Controller Gains on Dynamic Stiffness [7] 52

Figure 3.1 Picture of the Gimbal Platform to be Stabilized 58

Figure 3.2 Azimuth Axis Plant Bode Plot Between Torque Command and Angular Acceleration 60

Figure 3.3 Elevation Axis Plant Bode Plot Between Torque Command and Angular Acceleration 61

Figure 3.4 Azimuth Axis Friction Torque Plot 64

Figure 3.5 Elevation Axis Friction Torque Plot 65

Figure 3.6 Sample Accelerometer Array and Gyroscope Noises Collected from the System in the Absence of any Motion 68

Figure 3.7 Artificially Created Accelerometer Array and Gyroscope Noises to be Used in the Simulation Model 69

Figure 3.8 Power Density Spectrum Computed for Angular Acceleration Signal Collected for y-axis of the Gimbal 71

Figure 3.9 Power Density Spectrum Computed for Angular Velocity Signal Collected for y-axis of the Gimbal 72

Figure 3.10 Histogram of the Sample Angular Velocity Measurement for y-axis 73

Figure 3.11 Histogram of the Sample Angular Acceleration Measurement for y-axis 74

Figure 3.12 Variation of the Kalman Filter Transfer Function Between Input Velocity and Output Velocity for Different Values of the Modeling Noise Covariance 75

Figure 3.13 Variation of the Kalman Filter Transfer Function Between Input Acceleration and Output Acceleration for Different Values of the Modeling Noise Covariance 76

Figure 3.14 Input Acceleration-Output Acceleration Transfer Functions of the Two Kalman Filters Compared; The One With Acceleration and Velocity Input and the One With Only Velocity Input 79

Figure 3.15 Input Velocity-Output Velocity Transfer Functions of the Two Kalman Filters Compared; The One With Acceleration and Velocity Input and the One With Only Velocity Input 80

Figure 3.16 Simulation Model of the System Built in Simulink 83

Figure 3.17 SimMechanics Body Blocks and Joints Used for Modeling the Physical Bodies in the System 84

Figure 3.18 Joint Stiction Actuator Block of SimMechanics Which is Used to Simulate the Friction Torques in Mechanical System 85

Figure 3.19 Inclusion of Mechanical Structure Compliance Effects in the Simulation Model 89

Figure 3.20 Bode Plot Showing the Simulation of Structural Compliances in Azimuth Axis 90

Figure 3.21 Bode Plot Showing the Simulation of Structural Compliances in Elevation Axis 91

Figure 3.22 Gimbal Joint Which Simulates the Rotational Degrees of Freedom of the 6-DOF Motion Simulator Used 92

Figure 3.23 Standard Controller Azimuth Axis Open Loop Transfer Function . 93

Figure 3.24 Standard Controller Elevation Axis Open Loop Transfer Function . 94

Figure 3.25 Controller with Load Torque Estimator Azimuth Axis Open Loop Transfer Function 95

Figure 3.26 Controller with Load Torque Estimator Elevation Axis Open Loop Transfer Function 96

Figure 3.27 Controller with Inner Acceleration Loop Azimuth Axis Open Loop Transfer Function 97

Figure 3.28 Controller with Inner Acceleration Loop Elevation Axis Open Loop Transfer Function 98

Figure 3.29 State Derivative Feedback LQR Azimuth Axis Open Loop Transfer Function 99

Figure 3.30 State Derivative Feedback LQR Elevation Axis Open Loop Transfer Function 99

Figure 3.31 Azimuth Axis, Standard Controller, freq. 1Hz, amp. 9.5° 102

Figure 3.32 Azimuth Axis, Standard Controller, freq. 5Hz, amp. 0.65° 102

Figure 3.33 Azimuth Axis, Controller with Load Torque Estimator, freq. 1Hz, amp. 9.5° 103

Figure 3.34 Azimuth Axis, Controller with Load Torque Estimator, freq. 5Hz, amp. 0.65° 104
Figure 3.35 Azimuth Axis, Controller with Inner Acceleration Loop, freq. 1Hz, amp. 9.5° 105
Figure 3.36 Azimuth Axis, Controller with Inner Acceleration Loop, freq. 5Hz, amp. 0.65° 105
Figure 3.37 Azimuth Axis, State Derivative Feedback LQR, freq. 1Hz, amp. 9.5° 106
Figure 3.38 Azimuth Axis, State Derivative Feedback LQR, freq. 5Hz, amp. 0.65° 107
Figure 3.39 Elevation Axis, Standard Controller, freq. 1Hz, amp. 8° 108
Figure 3.40 Elevation Axis, Standard Controller, freq. 5Hz, amp. 0.6° 108
Figure 3.41 Elevation Axis, Controller with Load Torque Estimator, freq. 1Hz, amp. 8° 109
Figure 3.42 Elevation Axis, Controller with Load Torque Estimator, freq. 5Hz, amp. 0.6° 110
Figure 3.43 Elevation Axis, Controller with Inner Acceleration Loop, freq. 1Hz, amp. 8° 111
Figure 3.44 Elevation Axis, Controller with Inner Acceleration Loop, freq. 5Hz, amp. 0.6° 111
Figure 3.45 Elevation Axis, State Derivative Feedback LQR, freq. 1Hz, amp. 8° 112
Figure 3.46 Elevation Axis, State Derivative Feedback LQR, freq. 5Hz, amp. 0.6° 113

Figure 4.1 Aerotech Gimbal Platform Used in the Experimental Setup [37] . . 116
Figure 4.2 Elmo Digital Servo Drive Unit Used in the Experimental Setup [38] 118
Figure 4.3 Computer Aided Drawing Model of the Gimbal Assembly 123
Figure 4.4 6-DOF Motion Simulator Used in the Experiments 124
Figure 4.5 Azimuth Axis, Standard Controller, freq. 0.5 Hz, amp. 20° 130
Figure 4.6 Azimuth Axis, Standard Controller, freq. 1 Hz, amp. 9.5° 131
Figure 4.7 Azimuth Axis, Standard Controller, freq. 2 Hz, amp. 4° 131

Figure 4.8 Azimuth Axis, Standard Controller, freq. 5 Hz, amp. 0.65° 132

Figure 4.9 Azimuth Axis, Standard Controller, freq. 10 Hz, amp. 0.08° 132

Figure 4.10 Disturbance Torque Predicted by the Load Torque Estimator of Azimuth Axis 133

Figure 4.11 Azimuth Axis, Controller with Load Torque Estimator, freq. 0.5 Hz, amp. 20° 134

Figure 4.12 Azimuth Axis, Controller with Load Torque Estimator, freq. 1 Hz, amp. 9.5° 134

Figure 4.13 Azimuth Axis, Controller with Load Torque Estimator, freq. 2 Hz, amp. 4° 135

Figure 4.14 Azimuth Axis, Controller with Load Torque Estimator, freq. 5 Hz, amp. 0.65° 135

Figure 4.15 Azimuth Axis, Controller with Load Torque Estimator, freq. 10 Hz, amp. 0.08° 136

Figure 4.16 Azimuth Axis, Controller with Inner Acc. Loop, freq. 0.5 Hz, amp. 20° 137

Figure 4.17 Azimuth Axis, Controller with Inner Acc. Loop, freq. 1 Hz, amp. 9.5° 137

Figure 4.18 Azimuth Axis, Controller with Inner Acc. Loop, freq. 2 Hz, amp. 4° 138

Figure 4.19 Azimuth Axis, Controller with Inner Acc. Loop, freq. 5 Hz, amp. 0.65° 138

Figure 4.20 Azimuth Axis, Controller with Inner Acc. Loop, freq. 10 Hz, amp. 0.08° 139

Figure 4.21 Azimuth Axis, State Derivative Feedback LQR, freq. 0.5 Hz, amp. 20° 140

Figure 4.22 Azimuth Axis, State Derivative Feedback LQR, freq. 1 Hz, amp. 9.5° 141

Figure 4.23 Azimuth Axis, State Derivative Feedback LQR, freq. 2 Hz, amp. 4° 141

Figure 4.24 Azimuth Axis, State Derivative Feedback LQR, freq. 5 Hz, amp. 0.65° 142

Figure 4.25 Azimuth Axis, State Derivative Feedback LQR, freq. 10 Hz, amp. 0.08° 142

Figure 4.26 Elevation Axis, Standard Controller, freq. 0.5 Hz, amp. 17° 144

Figure 4.27 Elevation Axis, Standard Controller, freq. 1 Hz, amp. 8° 145

Figure 4.28 Elevation Axis, Standard Controller, freq. 2 Hz, amp. 3.5° 145

Figure 4.29 Elevation Axis, Standard Controller, freq. 5 Hz, amp. 0.6° 146

Figure 4.30 Elevation Axis, Standard Controller, freq. 10 Hz, amp. 0.1° 146

Figure 4.31 Disturbance Torque Predicted by the Load Torque Estimator of Elevation Axis 147

Figure 4.32 Elevation Axis, Controller with Load Torque Estimator, freq. 0.5 Hz, amp. 17° 148

Figure 4.33 Elevation Axis, Controller with Load Torque Estimator, freq. 1 Hz, amp. 8° 148

Figure 4.34 Elevation Axis, Controller with Load Torque Estimator, freq. 2 Hz, amp. 3.5° 149

Figure 4.35 Elevation Axis, Controller with Load Torque Estimator, freq. 5 Hz, amp. 0.6° 149

Figure 4.36 Elevation Axis, Controller with Load Torque Estimator, freq. 10 Hz, amp. 0.1° 150

Figure 4.37 Elevation Axis, Controller with Inner Acc. Loop, freq. 0.5 Hz, amp. 17° 151

Figure 4.38 Elevation Axis, Controller with Inner Acc. Loop, freq. 1 Hz, amp. 8° 151

Figure 4.39 Elevation Axis, Controller with Inner Acc. Loop, freq. 2 Hz, amp. 3.5° 152

Figure 4.40 Elevation Axis, Controller with Inner Acc. Loop, freq. 5 Hz, amp. 0.6° 152

Figure 4.41 Elevation Axis, Controller with Inner Acc. Loop, freq. 10 Hz, amp. 0.1° 153

Figure 4.42 Elevation Axis, State Derivative Feedback LQR, freq. 0.5 Hz, amp. 17° 154
Figure 4.43 Elevation Axis, State Derivative Feedback LQR, freq. 1 Hz, amp. 8° 155
Figure 4.44 Elevation Axis, State Derivative Feedback LQR, freq. 2 Hz, amp. 3.5° 155
Figure 4.45 Elevation Axis, State Derivative Feedback LQR, freq. 5 Hz, amp. 0.6° 156
Figure 4.46 Elevation Axis, State Derivative Feedback LQR, freq. 10 Hz, amp. 0.1° 156

LIST OF SYMBOLS

A description of the notation used in Section 2.2 is given first. This notation is adopted from lecture notes of ME502 Advanced Dynamics course given by Prof. Dr. Kemal Özgören in METU Mechanical Engineering Department in Fall 2008.

$\vec{r}$: the vector $\vec{r}$, which is independent of any reference frame

$\vec{r}^{(F)} = \bar{r}^{(F)}$: column matrix representation of the vector $\vec{r}$ in reference frame F

$\breve{D}$: the tensor $\breve{D}$, which is independent of any reference frame

$\breve{D}^{(F)} = \hat{D}^{(F)}$: matrix representation of the tensor $\breve{D}$ in reference frame F

$\hat{C}^{(a,b)}$: (component) transformation matrix from coordinate frame F_b to coordinate frame F_b

$\vec{r}_{P/O}$: position vector of point P with respect to point O

$\vec{v}_{P/O}$: velocity of point P with respect to point O obtained by differentiating in inertial coordinate frame

$\vec{a}_{P/O}$: acceleration of point P with respect to point O obtained by differentiating in inertial coordinate frame

$\vec{\omega}_{b/a}$: relative angular velocity of coordinate frame F_b with respect to F_a

$\vec{\alpha}_{b/a}$: relative angular acceleration of coordinate frame F_b with respect to F_a

$\bar{u}_1^{(a/b)}$: first unit vector of coordinate frame F_a represented in coordinate frame F_b

$\vec{a}_{C_I}$: acceleration vector of the COG of inner gimbal

$\vec{a}_{C_O}$: acceleration vector of the COG of outer gimbal

$\vec{g}$: gravity vector

m_I: mass of inner gimbal

m_O: mass of outer gimbal

u_k: Kalman input vector at time k

x_k: Kalman state vector at time k

y_k: Kalman output vector at time k

$\hat{C}^{(e,m)}$: coordinate frame transformation matrix relating frame (e) to (m)

$\vec{D}_I$: disturbance moment vector acting on the inner gimbal

$\vec{D}_O$: disturbance moment vector acting on the outer gimbal

$\vec{F}_{BO}$: force vector applied by base on outer gimbal

$\vec{F}_{IO}$: force vector applied by inner gimbal on outer gimbal

$\vec{F}_{OI}$: force vector applied by outer gimbal on inner gimbal

G_{md}: motor and driver combined transfer function

$\check{J}_I$: inertia tensor of the inner gimbal

$\check{J}_O$: inertia tensor of the outer gimbal

K: optimal gain vector

K_a: acceleration loop proportional gain

K_i: velocity loop integral gain

K_p: velocity loop proportional gain

K_t: torque constant

K_v: velocity loop double-integral gain

L: motor inductance

P_k: covariance matrix belonging to state vector x_k

R: motor resistance

$\vec{M}_{BO}$: moment applied by gimbal base on outer gimbal

$\vec{M}_{IO}$: moment applied by inner gimbal base on outer gimbal

$\vec{M}_{OI}$: moment applied by outer gimbal base on inner gimbal

$T_{fr_{BO}}$: friction torque applied to outer gimbal (azimuth axis)

$T_{fr_{OI}}$: friction torque applied to inner gimbal (elevation axis)

$T_{m_{BO}}$: motor torque applied to outer gimbal (azimuth axis)

$T_{m_{OI}}$: motor torque applied to inner gimbal (elevation axis)

$\vec{\alpha}_I$: angular acceleration vector of the coordinate frame fixed to the inner gimbal (elevation axis)

$\vec{\alpha}_O$: angular acceleration vector of the coordinate frame fixed to the outer gimbal (azimuth axis)

ϵ: elevation axis angle

η: azimuth axis angle

θ: platform pitch angle

υ_k: Kalman measurement noise matrix at time k

ϕ: platform roll angle

ψ: platform yaw angle

$\vec{\omega}_I$: angular velocity vector of the coordinate frame fixed to the inner gimbal (elevation axis)

ω_k: Kalman modeling noise matrix at time k

$\vec{\omega}_O$: angular velocity vector of the coordinate frame fixed to the outer gimbal (azimuth axis)

LIST OF ABBREVIATIONS

3-D: Three Dimensional

ARE: Algebraic Riccati Equation

COG: Center of Gravity

DOF: Degree of Freedom

FPGA: Field Programmable Gate Array

I/O: Input/Output

KF: Kalman Filter

LQR: Linear Quadratic Regulator

PI: Proportional-Integral

PII^2: Proportional-Integral-Double Integral

RTWT: Real-Time Windows Target

CHAPTER 1

INTRODUCTION

1.1 Background and Motivations

Stabilized platforms are rapidly populating different areas of application as sensor and actuator technology develops and more accurate, robust sensors and actuators are available for much cheaper prices. While stabilization may refer to different tasks and applications in different areas, in motion control the term refers to stabilizing the angular position of a moving platform relative to earth frame [1]. The objective of motion stabilization is to decouple the stabilized payload from vehicle motion disturbances [2, 3] and at the same time reject forces and moments acting on the platform. Depending on the type of platform that is stabilized, different names such as line-of-sight stabilization for optics, radar, laser beam etc. stabilization applications or line-of-fire stabilization for weapon platform stabilization are also used in the literature. From here on, stabilization term is used to refer to its correspondence in motion control area described above.

As mentioned above, different payloads ranging from a small laser beam reflecting mirrors weighting only a couple hundred grams to an anti-air gun platform or a main battle tank turret weighting more than 10 tons can be the subject of stabilization application. As a general trend, for bigger masses some limitations start to become more prominent and stabilization performances degrade. The most important of these limitations are actuator and driver power saturation issues and compliances in both transmission elements and mechanical structure due to the very high amounts of torque and force transmitted. As a result while good stabilization can be achieved for bigger

platforms with clever mechanical design and sensor and actuator selection, smaller platforms can achieve much better performances.

Although the methods developed in this thesis work are applicable to both smaller and bigger platforms, smaller and more agile platforms can benefit much more since these methods tend to create very dynamic and high bandwidth controllers whose implementation on bigger platforms may lead to actuator saturation problems or excessive loading in transmission and structural elements as mentioned above. In agreement with this fact, the experimental setup which is going to be used is a low payload gimbal platform developed originally for stabilizing small payloads such as mirrors or small optics.

These high performance small stabilized platforms find a very broad usage area in military industry and are used for many mission-critical battlefield applications such as electro-optic platforms with day and night vision cameras, small tracking radars, laser beam directors used for target designation, seeker head directors used on missiles and many others. As one can suggest, all of these application require very accurate positioning and stabilization of the platform in the order of micro-radians since even very small angular displacements result in big position errors when a target kilometers away is being tracked or pointed to. In Figure 1.1 ASELFLIR 300T of ASELSAN can be seen, which is a high performance stabilized electro-optic platform also used for target designation.

For achieving very small stabilization errors required for these platforms, top quality components and special techniques are used. Navigation grade sensors and actuators, low friction bearings, slip rings and other components are placed on specially designed and manufactured mechanical structures. High cost techniques such as double stage stabilization are used for achieving even higher accuracies. The method of using angular acceleration feedback, which is going to be the topic of this thesis work, may be considered as one of these techniques trying to achieve higher accuracy stabilization.

Motion controllers of stabilized platforms try to tackle different problems in the course of operation. Most of the time these problems can be separated as the problem of stabilization, and the problem of positioning and tracking and these two problems

Figure 1.1: ASELFLIR 300T Stabilized Electro Optic Platform Developed and Manufactured by ASELSAN

must be handled using different approaches. While positioning and tracking can be identified as a servo tracking problem and high performance can be achieved with high quality sensors and algorithms such as trajectory planners or target estimators, the problem of stabilization can be classified as a regulator problem and the use of proper disturbance rejection algorithms plays a crucial role for high performance applications. It is important to note that this thesis work focuses on the second problem stated above; namely the problem of regulating the position of the platform by rejecting disturbances coming from various sources.

The sources of disturbances acting on a stabilized platform may vary greatly, however when the overall picture is analyzed a short list of the most common sources can be populated as follows;

- By far the most common and most important of these sources is the friction

torques originating from the relative motion in platform axes of rotation. The reason why friction is located on the top of the list is that, friction is an inevitable phenomenon and no matter how small it is, it always exists. Furthermore, as long as stabilization is being done under angular motion of the base platform friction torques always exist disturbing the system constantly.

- Another common source of disturbance originates from unbalanced mass center of a platform axis meaning that the center of gravity and center of rotation of the axis do not coincide. In the presence of linear accelerations, unbalanced masses result in a net disturbance torque around the center of rotation. However this can be avoided by designing the mechanical structure such that the centers of gravity of all axes are located on the centers of rotation of corresponding axes.

- The last sources of disturbance on the list are external torques and forces acting on the platform as a result of interactions with the environment or actions such as firing of weapons or missiles. This source of disturbance can only be seen on a limited number of stabilization applications such as weapon platforms and may be avoided or minimized with proper placement of line-of-fire, etc.

Throughout the course of studies, the effects of the first disturbance source defined above, namely the friction forces are focused upon. However disturbances due to unbalanced mass centers also showed up in experimental tests but it is considered that regardless of the source of disturbance tested, improvements should be applicable to rejection of disturbances from all sources.

In the light of these discussions, the main motivation of this thesis is to improve disturbance rejection and stabilization performances of smaller more agile stabilized platforms. It is important to note that the usage of accelerometers as additional sensors is required for the proposed methods. While the usage of additional sensors brings cost and complexity further improvement of the stabilization accuracy is near impossible for these already high performance platforms without further instrumentation. Furthermore, the cost and complexity of using accelerometers is nowhere near the cost and complexity of other methods such as two stage stabilization or replacing the already expensive gyroscopes mounted on the platform with better ones, price of which exponentially grows for better grade sensors.

1.2 Objectives and Contributions of the Thesis

For achieving better stabilization accuracies, many different disturbance rejection algorithms are proposed in the literature and a subclass of these methods use acceleration feedback. The use of acceleration feedback indeed proves to be effective for the purpose of disturbance rejection in industrial applications such as the servo control of machines, conveyors, robot arms etc, that continuously interact with the environment and work under varying loads. There exists quite a few number of publications focusing on different ways of utilizing acceleration feedback for such applications. However, extension of these methods to the stabilization problem, where disturbance rejection is of paramount importance, haven't seen enough attention.

The main objective of this thesis work is to apply several different disturbance rejection algorithms utilizing acceleration feedback, which include newly formulated ones together with the previously developed methods, to the platform stabilization problem for improving the disturbance rejection properties and therefore the overall stabilization accuracy. Accomplishment of these objectives will enable improvement of stabilization even for already built systems with the addition of a linear accelerometer array together with some modifications in the control software.

While the above defined goal is being achieved, several different problems are addressed. To start with, the problem of calculating all three angular accelerations of a platform using linear accelerometer readings is addressed. Then, improvements that can be achieved in signal quality with the addition of another measurement, in our case addition of acceleration measurement to the already measured velocity, is assessed. Finally a new optimal controller using the acceleration feedback for improving stabilization performance is developed starting from a similar controller concept using the "Reciprocal State Space" framework defined in the literature.

1.3 Outline of the Thesis

In this first chapter, background information and motivations for carrying out this thesis work is given together with the objectives and contributions.

Chapter 2 presents the theoretical background for various problems that needs to be tackled throughout the course of studies such as the calculation of angular acceleration from linear acceleration measurements, mathematical modeling of the 2-DOF gimbal platform starting from Newton-Euler equations of motion, a quick review of Kalman filtering and usage of different acceleration feedback methods for improving stabilization performance.

In Chapter 3, a detailed explanation of the simulation model built is given and controller implementation issues are discussed. The chapter starts with the explanation of identification work done on the experimental setup. Justification of Kalman filter usage and other issued related to sensor fusion and filtering is given next. Last part of the chapter is devoted to the presentation of the simulation model built and simulation tests done on this model.

Chapter 4 starts with a brief description of the experimental setup. The rest of this chapter is devoted to the presentation of experimental test results.

Finally, Chapter 5 includes an overall discussion of the work done and concluding remarks. Possible future work that could not be covered inside the scope of this thesis is also given.

CHAPTER 2

THEORETICAL BACKGROUND

In this chapter, theoretical background of the thesis work is laid down. Several topics that are investigated in the course of studies that deserve attention are covered here. Survey of the literature about these topics and the extensions of this literature to our application are combined in order to have a seamless flow and better understanding of the methods discussed. Following chapters will build on this background and will be the implementation of the ideas developed here in simulation environment and on experimental setup.

This chapter starts with the literature survey done on the methods of constructing angular acceleration information by using linear accelerometers. In the next section, a derivation of the dynamic equations of motion of the 2-DOF gimbal moving on a motion simulator are carried out starting from Newton-Euler equations. In the third section, a quick review of Kalman filtering is given. Final chapter is devoted to the investigation and development of controllers that can make use of the acceleration information of the platform in order to improve the stabilization performance of the system. A standard controller for comparison purposes and three other controllers that utilize acceleration feedback are presented.

2.1 Construction of Inertial Angular Acceleration Information of a Platform

The main objective of this thesis work, which is the use of angular acceleration information to improve the stabilization performance of a stabilized platform, makes it necessary to obtain a good quality angular acceleration signal by either directly mea-

suring it or constructing it from other measurements. Furthermore, this information is needed relative to inertial reference frame since stabilization requires the control of the platform in the earth-fixed inertial reference frame.

However, both of the above mentioned methods for obtaining an angular acceleration signal have different drawbacks of their own [4]. For example the most straightforward method, being the direct measurement of inertial angular acceleration requires angular accelerometers, which are very special sensors that are manufactured by a very limited number of manufacturers, quite hard to obtain even from these limited number of manufacturers due to export restrictions and significantly expensive, especially because of the fact that there are no cheap options on the market for these sensors. The method of obtaining an angular acceleration signal from angular velocity or position measurements suffers from noise amplification problems. Obtaining acceleration this way requires the differentiation of velocity and position signals using one of the several methods proposed in the literature. However regardless of the method used, noise always remains problem to be solved. Although it is proposed in papers [5, 6, 7, 8], it is seen that obtaining acceleration information from position signal with double differentiation or using an observer produces extremely poor results. Single differentiation of a high quality velocity signal on the other hand, with careful noise filtering, can lead to a somehow usable signal, but marginal performance improvement should be expected as a benefit of using this signal.

A third way of constructing angular acceleration signal which seems not to suffer from the drawbacks of the methods above is the use of linear accelerometers. Linear accelerometers are widely used sensors that can be found very easily. Furthermore, since no differentiation but only algebraic operations are carried out to obtain the angular acceleration, this method does not suffer from noise amplification problem mentioned above. Being a viable solution, methods of obtaining angular acceleration from linear accelerometer measurements has been investigated by many authors and found to be an effective aproach. A literature survey on this method and development of this method follows in the coming section.

2.1.1 Preliminaries on Kinematics and Acceleration in 3-D Space

Here, some preliminary information about three-dimensional kinematics is given on which the following derivations are based on. A more detailed information can be found in [9], from where the following derivation is adopted.

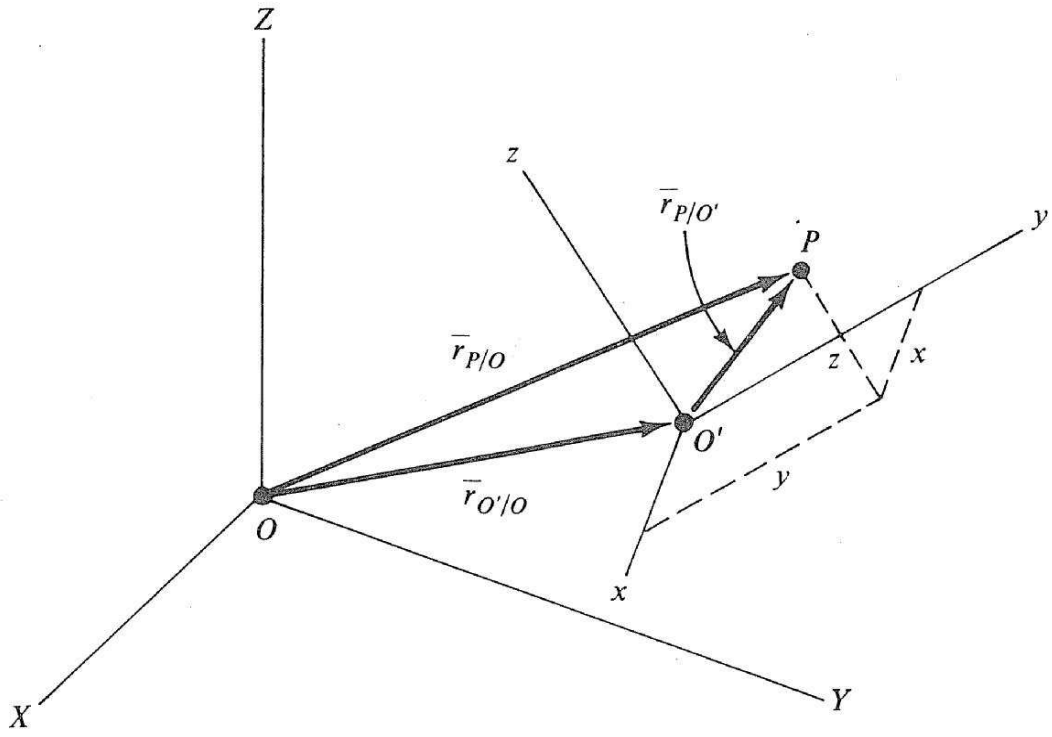

Figure 2.1: Position of a Point P Relative to a Moving Reference Frame [1]

$$\bar{a}_P = \bar{a}_{O'} + (\bar{a}_P)_{xyz} + \bar{\alpha} \times \bar{r}_{P/O'} + \bar{\omega} \times (\bar{\omega} \times \bar{r}_{P/O'}) + 2\bar{\omega} \times (\bar{v}_P)_{xyz} \tag{2.1}$$

Above equation is the famous acceleration relation that can be written between two points P and O' in space, which are shown in Figure 2.1. Here ω and α are the angular velocity and angular acceleration of the body fixed coordinate frame depicted in the figure. It is also the starting point for our efforts of constructing angular acceleration information from linear accelerometer readings and therefore needs some attention. The derivation of the equation is as follows;

Position of the point P relative to the origin of inertial reference frame O can be

written as follows

$$\bar{r}_{P/O} = \bar{r}_{O'/O} + \bar{r}_{P/O'} \tag{2.2}$$

By definition, the absolute velocity is the time derivative of the position with respect to the fixed reference frame. Differentiating 2.2 gives

$$\bar{v}_P = \bar{v}_{O'} + \frac{d}{dt}\bar{r}_{P/O'} \tag{2.3}$$

Most probably, the (moving) *xyz* reference frame is chosen for its convenience in describing the position of P

$$\bar{r}_{P/O'} = x\bar{i} + y\bar{j} + z\bar{k} \tag{2.4}$$

Differentiating with superposing the effects of the changing coordinate values and the rotation of the vectors gives

$$\frac{d}{dt}\bar{r}_{P/O'} = \dot{x}\bar{i} + \dot{y}\bar{j} + \dot{z}\bar{k} + \bar{\omega} \times \bar{r}_{P/O'} \tag{2.5}$$

Combining 2.3 and 2.5, we have

$$\bar{v}_P = \bar{v}_{O'} + (\bar{v}_P)_{xyz} + \bar{\omega} \times \bar{r}_{P/O'} \tag{2.6}$$

where

$$(\bar{v}_P)_{xyz} = \frac{\partial}{\partial t}\bar{r}_{P/O'} = \dot{x}\bar{i} + \dot{y}\bar{j} + \dot{z}\bar{k} \tag{2.7}$$

The above equation 2.6 is the expression for the velocity of point P. Note that the reference frame specification are omitted when indicating an absolute velocity or acceleration.

The derivation continues with acceleration. Note that time differentiation of both sides of equation 2.6 will give the acceleration of point P. Hence we differentiate the terms on the right hand side of the equation one-by-one. The derivative of the velocity of origin O' is its acceleration. Since the term $(\bar{v}_P)_{xyz}$ gives relative velocity in terms of components in moving frame

$$\frac{d}{dt}(\bar{v}_P)_{xyz} = (\bar{a}_P)_{xyz} + \bar{\omega} \times (\bar{v}_P)_{xyz} \tag{2.8}$$

The third term is $\bar{\omega} \times \bar{r}_{P/O'}$, the derivative of angular velocity ω is the angular acceleration α and derivative of the term $\bar{r}_{P/O'}$ is already given above; so that

$$\frac{d}{dt}(\bar{\omega} \times \bar{r}_{P/O'}) = \bar{\alpha} \times \bar{r}_{P/O'} + \bar{\omega} \times [(\bar{v}_P)_{xyz} + \bar{\omega} \times \bar{r}_{P/O'}] \tag{2.9}$$

Summation of the last three terms leads to equation 2.1, which is rewritten below. Terms known with the special names, centripetal acceleration and Coriolis acceleration, are pointed out in the equation below.

$$\bar{a}_P = \bar{a}_{O'} + (\bar{a}_P)_{xyz} + \bar{\alpha} \times \bar{r}_{P/O'} + \overbrace{\bar{\omega} \times (\bar{\omega} \times \bar{r}_{P/O'})}^{\text{centripetal acc.}} + \overbrace{2\bar{\omega} \times (\bar{v}_P)_{xyz}}^{\text{Coriolis acc.}}$$

At this point, it is important to note that for a point P on a rigid body, both the velocity term $(\bar{v}_P)_{xyz}$ and the acceleration term $(\bar{a}_P)_{xyz}$ become zero. Therefore, if we assume that O' is the origin of a reference frame fixed to a rigid body and P is a point on the same rigid body, the expression for the acceleration of point P in inertial reference frame simplifies to Equation 2.10 below

$$\bar{a}_P = \bar{a}_{O'} + \bar{\alpha} \times \bar{r}_{P/O'} + \bar{\omega} \times (\bar{\omega} \times \bar{r}_{P/O'}) \tag{2.10}$$

2.1.2 Determination of Angular Velocity and Angular Acceleration of a Body From Linear Accelerometer Readings

In Figure 2.2, four points which are located on the same rigid body are shown together with inertial and body fixed coordinate frames. Starting from where we left off in the previous subsection, for the two points P_1 and O on the rigid body, we can write

$$\bar{a}_{P_1} = \bar{a}_O + \bar{\alpha} \times (\bar{r}_{P_1/O}) + \bar{\omega} \times (\bar{\omega} \times (\bar{r}_{P_1/O})) \tag{2.11}$$

with all components in inertial coordinate frame except $\bar{r}_{P_1/O}$ whose components are presented in body fixed reference frame defined above. This equation can also be written as

$$\bar{a}_{P_1} - \bar{a}_O = \dot{\bar{\mathrm{W}}}(\bar{r}_{P_1/O}) + \bar{\mathrm{W}}^2(\bar{r}_{P_1/O}) \tag{2.12}$$

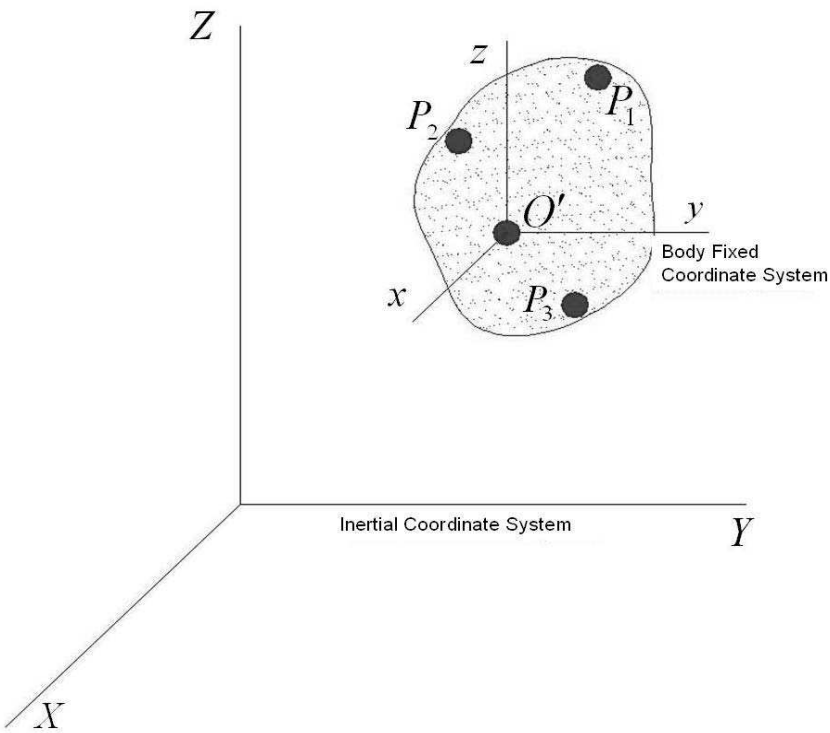

Figure 2.2: Description of Rigid Body Motion Using Different Coordinate Frames

where

$$\bar{\omega} = \begin{bmatrix} \omega_x \\ \omega_y \\ \omega_z \end{bmatrix}$$

and

$$\bar{\mathrm{W}} = \begin{bmatrix} 0 & -\omega_z & \omega_y \\ \omega_z & 0 & -\omega_x \\ -\omega_y & \omega_x & 0 \end{bmatrix}$$

In open form, Equation 2.12 can be written as follows

$$\begin{bmatrix} (a_{P_1})_x \\ (a_{P_1})_y \\ (a_{P_1})_z \end{bmatrix} - \begin{bmatrix} (a_O)_x \\ (a_O)_y \\ (a_O)_z \end{bmatrix} = \begin{bmatrix} -\omega_y{}^2 - \omega_z{}^2 & \omega_x\omega_y - \dot{\omega}_z & \omega_x\omega_z + \dot{\omega}_y \\ \omega_x\omega_y + \dot{\omega}_z & -\omega_z{}^2 - \omega_x{}^2 & \omega_y\omega_z - \dot{\omega}_x \\ \omega_x\omega_z - \dot{\omega}_y & \omega_y\omega_z + \dot{\omega}_x & -\omega_x{}^2 - \omega_y{}^2 \end{bmatrix} \begin{bmatrix} (r_{P_1/O})_x \\ (r_{P_1/O})_y \\ (r_{P_1/O})_z \end{bmatrix} \tag{2.13}$$

Equation 2.13 is important for the fact that it groups the terms as the left side of the equation being the linear accelerations which can be measured with linear accelerom-

eters, the 3x3 matrix on the right containing the unknown angular velocity and acceleration terms and the 3x1 vector on the right is the known vector of distance between the two points. Our goal will be to find the total of six unknown angular acceleration and angular velocity terms, all contained in the 3x3 matrix on the right-hand side of the Equation 2.13.

There has been many methods proposed in order to find the angular velocity and angular acceleration terms appearing in Equation 2.13. Some of these methods make use of numerical differentiation as well as numerical integration [10] and are therefore omitted in the foregoing analysis for the reason that these methods will most likely give poor results in a real-time applications such as this one. On the other hand, many other methods try to extract the nonlinear angular velocity terms appearing in the above equation by making use of symmetric and skew symmetric matrices and methods such as change of coordinate frames as in [11]. A classification of these methods and corresponding accelerometer placements is given in [12].

However, the emphasis of this work is not on the construction of angular velocity terms which most of these methods focus on since angular velocities are already measured with gyroscopes mounted on the system. Therefore, we do not dive too much into these different methods and stick with one class that gives angular acceleration terms directly. Angular velocity terms are obtained as by-products, which is also good for comparing with the measured signals from gyros, but not strictly necessary.

As shown in [13], the minimum number of sensors required to identify all angular velocity and angular acceleration terms is nine. However, it should be noted that identification of these terms are used in the meaning of identifying the magnitudes, as sign ambiguities persist in most solutions. From here on, “uniquely identifying” will be used for finding both magnitude and sign of these components.

With nine sensors, all angular acceleration terms are uniquely identified but angular velocity terms have ambiguities depending on the solution scheme. If we further restrict ourselves to the use of triaxial accelerometers, which will be the case in our work, then three triaxial accelerometers can only identify one angular acceleration term uniquely, leaving the remaining two angular accelerations and three angular velocities with sign ambiguities as shown in [14]. On the other hand, using four

triaxial accelerometers, we can uniquely identify the angular acceleration vector and identify the terms in angular velocity vector down to one sign ambiguity as shown in [15]. Note that the given equations has no means to distinguish between the two possible solutions (sign ambiguity) without additional auxiliary information.

In our studies, we will assume that the triaxial accelerometers are ideal, namely all three axes of measurement are done from the same point while we know that it is not the case since triaxial accelerometers are three uniaxial accelerometers packed together and some distance always exists among these three. However, very small size accelerometers that are going to be used makes this assumption reasonable. The case in which these accelerometers are considered non-ideal is further discussed in [16].

Going back to Equation 2.13, assuming we have 4 triaxial accelerometers placed such that one of them is at the center and the three other are placed such that

$$\bar{r}_{P_1/O} = \begin{bmatrix} 1 \\ 0 \\ 0 \end{bmatrix}, \bar{r}_{P_2/O} = \begin{bmatrix} 0 \\ 1 \\ 0 \end{bmatrix}, \bar{r}_{P_3/O} = \begin{bmatrix} 0 \\ 0 \\ 1 \end{bmatrix}$$

Three independent matrix equations can be written for the four triaxial accelerometers, between O and P_1, O and P_2, and the last one between O and P_3. These three matrix equations can be decomposed into the following nine scalar equations starting from 2.14 through 2.22.

$$(a_{P_1})_x - (a_O)_x = -\omega_y{}^2 - \omega_z{}^2 \tag{2.14}$$

$$(a_{P_1})_y - (a_O)_y = \omega_x\omega_y + \dot{\omega}_z \tag{2.15}$$

$$(a_{P_1})_z - (a_O)_z = \omega_x\omega_z - \dot{\omega}_y \tag{2.16}$$

$$(a_{P_2})_x - (a_O)_x = \omega_x\omega_y - \dot{\omega}_z \tag{2.17}$$

$$(a_{P_2})_y - (a_O)_y = -\omega_z{}^2 - \omega_x{}^2 \tag{2.18}$$

$$(a_{P_2})_z - (a_O)_z = \omega_y\omega_z + \dot{\omega}_x \tag{2.19}$$

$$(a_{P_3})_x - (a_O)_x = \omega_x\omega_z + \dot{\omega}_y \tag{2.20}$$

$$(a_{P_3})_y - (a_O)_y = \omega_y\omega_z - \dot{\omega}_x \tag{2.21}$$

$$(a_{P_3})_z - (a_O)_z = -{\omega_x}^2 - {\omega_y}^2 \tag{2.22}$$

Angular acceleration terms can be obtained as follows; from Equations 2.19 and 2.21 one can write

$$(a_{P_2})_z - (a_O)_z - (a_{P_3})_y + (a_O)_y = \omega_y\omega_z + \dot{\omega}_x - \omega_y\omega_z + \dot{\omega}_x$$

Therefore

$$\dot{\omega}_x = \frac{(a_{P_2})_z - (a_O)_z - (a_{P_3})_y + (a_O)_y}{2} \tag{2.23}$$

Doing similar calculations, from Equations 2.16 and 2.20

$$\dot{\omega}_y = \frac{(a_{P_3})_x - (a_O)_x - (a_{P_1})_z + (a_O)_z}{2} \tag{2.24}$$

And finally from Equations 2.15 and 2.17

$$\dot{\omega}_z = \frac{(a_{P_1})_y - (a_O)_y - (a_{P_2})_x + (a_O)_x}{2} \tag{2.25}$$

For the solution of the nonlinear velocity equations, we have the following from Equations 2.14, 2.18 and, 2.22;

$${\omega_x}^2 = \frac{(a_{P_1})_x - (a_O)_x - (a_{P_2})_y + (a_O)_y - (a_{P_3})_z + (a_O)_z}{2} \tag{2.26}$$

and;

$${\omega_y}^2 = \frac{(a_{P_2})_y - (a_O)_y - (a_{P_1})_x + (a_O)_x - (a_{P_3})_z + (a_O)_z}{2} \tag{2.27}$$

and finally;

$${\omega_z}^2 = \frac{(a_{P_3})_z - (a_O)_z - (a_{P_1})_x + (a_O)_x - (a_{P_2})_y + (a_O)_y}{2} \tag{2.28}$$

furthermore, these three additional equations can be written

from Equations 2.19 and 2.21

$$\omega_y\omega_z = \frac{(a_{P_2})_z - (a_O)_z + (a_{P_3})_y - (a_O)_y}{2} \tag{2.29}$$

from Equations 2.16 and 2.20

$$\omega_x\omega_z = \frac{(a_{P_3})_x - (a_O)_x + (a_{P_1})_z - (a_O)_z}{2} \tag{2.30}$$

from Equations 2.15 and 2.17

$$\omega_x\omega_y = \frac{(a_{P_1})_y - (a_O)_y + (a_{P_2})_x - (a_O)_x}{2} \tag{2.31}$$

As a result, determination of angular velocities problem becomes finding ω_x, ω_y and ω_z with ${\omega_x}^2$, ${\omega_y}^2$, ${\omega_z}^2$, $\omega_y\omega_z$, $\omega_x\omega_z$ and $\omega_x\omega_y$ known.

Magnitudes of ω_x, ω_y, and ω_z can be found by taking the square roots of ${\omega_x}^2$, ${\omega_y}^2$, and ${\omega_z}^2$, respectively. The signs on the other hand can be found from the remaining equations with one sign ambiguity, meaning that when a sign is assigned to any one of the three angular velocity terms, the rest can be determined from the equations.

For nine sensors that are not necessarily triaxial, different solution schemes are designed. These solutions eliminate the quadratic terms of the type $\omega_u\omega_v$ or of the type ${\omega_u}^2 + {\omega_v}^2$ $(u, v = x, y, z)$. In both cases, the system becomes linear in new auxiliary variables a, b, c or α, β, γ, where

$$a = \omega_y\omega_z$$

$$b = \omega_x\omega_z$$

$$c = \omega_x\omega_y$$

or

$$\alpha = {\omega_y}^2 + {\omega_z}^2$$

$$\beta = {\omega_x}^2 + {\omega_z}^2$$

$$\gamma = {\omega_x}^2 + {\omega_y}^2$$

from these two sets of auxiliary variables above, two different solutions are obtained for the angular velocity terms.

For the set a, b, c;

$$\omega_x = \pm\sqrt{\frac{bc}{a}} \tag{2.32}$$

$$\omega_y = \pm\sqrt{\frac{ac}{b}} \tag{2.33}$$

$$\omega_z = \pm\sqrt{\frac{ab}{c}} \tag{2.34}$$

And for the set α, β, γ;

$$\omega_x = \pm\sqrt{\frac{-\alpha+\beta+\gamma}{2}} \tag{2.35}$$

$$\omega_y = \pm\sqrt{\frac{\alpha-\beta+\gamma}{2}} \tag{2.36}$$

$$\omega_x = \pm\sqrt{\frac{\alpha+\beta-\gamma}{2}} \tag{2.37}$$

In the first case, the sign of one component of $\bar{\omega}$ must be arbitrarily assigned while the sign of others are determined from the equations. However, the equations become singular if $a, b, c = 0$. In the second case, eight different sign combinations are always found and there is no possibility to select the correct one.

2.1.3 Method Used in this Thesis Work

For the rest of this section, we are going to analyze the first of the cases above which is important in the sense that it is obtained with an accelerometer placement as discussed in [17], which is one of the former and most important works in the subject.

Consider the following sensor placement, with the point O being in the middle and P_1, P_2, and P_3 being placed as

$$\bar{r}_{P_1/O} = \begin{bmatrix} 1 \\ 0 \\ 0 \end{bmatrix}, \text{at } P_1, y \text{ and } z \text{ accelerations are measured}$$

$$\bar{r}_{P_2/O} = \begin{bmatrix} 0 \\ 1 \\ 0 \end{bmatrix}, \text{at } P_2, x \text{ and } z \text{ accelerations are measured}$$

$$\bar{r}_{P_3/O} = \begin{bmatrix} 0 \\ 0 \\ 1 \end{bmatrix}, \text{at } P_3, x \text{ and } y \text{ accelerations are measured}$$

Resulting equations does not include any diagonal terms of the unknown matrix, namely the terms $(-\omega_y{}^2 - \omega_z{}^2)$, $(-\omega_z{}^2 - \omega_x{}^2)$, and $(-\omega_x{}^2 - \omega_y{}^2)$. Six scalar equations, which is a subset of the former nine equations, can be written as follows

$$(a_{P_1})_y - (a_O)_y = \omega_x\omega_y + \dot{\omega}_z \tag{2.38}$$

$$(a_{P_1})_z - (a_O)_z = \omega_x\omega_z - \dot{\omega}_y \tag{2.39}$$

$$(a_{P_2})_x - (a_O)_x = \omega_x\omega_y - \dot{\omega}_z \tag{2.40}$$

$$(a_{P_2})_z - (a_O)_z = \omega_y\omega_z + \dot{\omega}_x \tag{2.41}$$

$$(a_{P_3})_x - (a_O)_x = \omega_x\omega_z + \dot{\omega}_y \tag{2.42}$$

$$(a_{P_3})_y - (a_O)_y = \omega_y\omega_z - \dot{\omega}_x \tag{2.43}$$

Solutions for $\dot{\omega}_x$, $\dot{\omega}_y$ and $\dot{\omega}_z$ are obtained as in Equations 2.23 through 2.25. The solutions for angular velocities can be obtained as given in Equations 2.32 through 2.34. Below, you can find these solutions together for all angular acceleration and angular velocity terms in equations 2.44 through 2.49.

$$\dot{\omega}_x = \frac{(a_{P_2})_z - (a_O)_z - (a_{P_3})_y + (a_O)_y}{2} \tag{2.44}$$

$$\dot{\omega}_y = \frac{(a_{P_3})_x - (a_O)_x - (a_{P_1})_z + (a_O)_z}{2} \tag{2.45}$$

$$\dot{\omega}_z = \frac{(a_{P_1})_y - (a_O)_y - (a_{P_2})_x + (a_O)_x}{2} \tag{2.46}$$

and

$$\omega_x = \pm\sqrt{\frac{bc}{a}} \tag{2.47}$$

$$\omega_y = \pm\sqrt{\frac{ac}{b}} \tag{2.48}$$

$$\omega_z = \pm\sqrt{\frac{ab}{c}} \tag{2.49}$$

2.2 Mathematical Model of the 2-DOF Gimbal Platform Including Base Disturbances

In order to be able to identify the plant to be controlled more clearly and base the controller architecture design work on it, a dynamic model of the 2-DOF gimbal platform together with the kinematic disturbances applied to the base of the platform needs to be constructed. Several models for such platforms are present in the literature that employs Newtonian [18, 19] or Lagrangian [20] formulation in the derivation. However, none of these is a satisfactory model that models the kinematic disturbance applied to the base of the platform in addition to the 2-DOF gimbal itself.

Therefore, in this section, the mathematical model of the gimbal platform is derived starting from Newton-Euler equations written for azimuth and elevation axes separately. Mathematical model of the physical system is important as it is necessary for the design of different control architectures. Later in Chapter 3, a simulation model of the system will be constructed and tuning of these controllers will be done on the simulation model. For the mathematical model, at the beginning a model for the most general case will be developed and later some assumptions and simplifications that apply to our system will be carried out in order to obtain a simpler model which the designed controllers can be based upon.

This model will include the 2-DOF gimbal platform with outer (azimuth) and inner (elevation) gimbals and the base motion which is assumed to be a pure rotational motion around the intersection of center of rotations of the two gimbal axes. The base motion is described as a yaw-pitch-roll sequence. Following reference frames are used throughout the analysis.

(e)**:** Coordinate frame fixed to earth (Inertial frame)

$(m), (n)$**:** Intermediate coordinate frames used in describing the platform base motion

(B)**:** Coordinate frame fixed to the gimbal base

(O)**:** Coordinate frame fixed to the outer gimbal (azimuth axis)

(I)**:** Coordinate frame fixed to the inner gimbal (elevation axis)

Relations of these frames with respect to each other in terms of rotation directions and angles can be shown as in Figure 2.3: below;

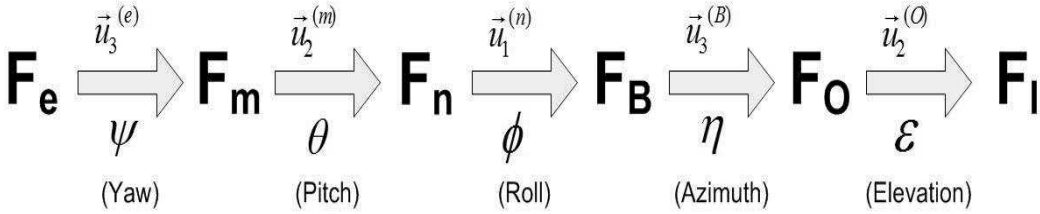

Figure 2.3: Coordinate Frames Used and Rotational Relations Between Those

In addition, coordinate frame transformation matrices relating these coordinate frames are as follows

$$\hat{C}^{(e,m)} = e^{\tilde{u}_3\psi} = \begin{bmatrix} \cos(\psi) & -\sin(\psi) & 0 \\ \sin(\psi) & \cos(\psi) & 0 \\ 0 & 0 & 1 \end{bmatrix} \tag{2.50}$$

$$\hat{C}^{(m,n)} = e^{\tilde{u}_2\theta} = \begin{bmatrix} \cos(\theta) & 0 & \sin(\theta) \\ 0 & 1 & 0 \\ -\sin(\theta) & 0 & \cos(\theta) \end{bmatrix} \tag{2.51}$$

$$\hat{C}^{(n,B)} = e^{\tilde{u}_1\phi} = \begin{bmatrix} 1 & 0 & 0 \\ 0 & \cos(\phi) & -\sin(\phi) \\ 0 & sin(\phi) & cos(\phi) \end{bmatrix} \tag{2.52}$$

$$\hat{C}^{(B,O)} = e^{\tilde{u}_3\eta} = \begin{bmatrix} \cos(\eta) & -\sin(\eta) & 0 \\ \sin(\eta) & \cos(\eta) & 0 \\ 0 & 0 & 1 \end{bmatrix} \tag{2.53}$$

$$\hat{C}^{(O,I)} = e^{\tilde{u}_2\epsilon} = \begin{bmatrix} \cos(\epsilon) & 0 & \sin(\epsilon) \\ 0 & 1 & 0 \\ -\sin(\epsilon) & 0 & \cos(\epsilon) \end{bmatrix} \tag{2.54}$$

Figure 2.4 below shows some unit vectors of these coordinate frames on the gimbal;

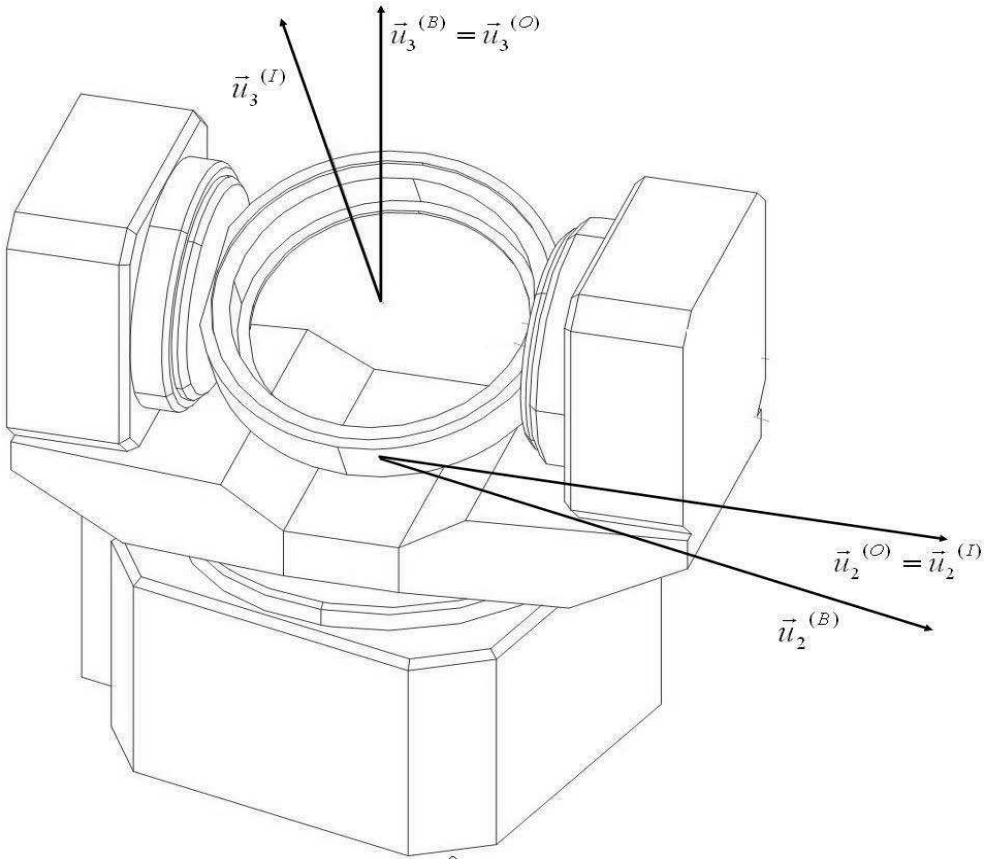

Figure 2.4: Important Unit Vector Directions on the 2-DOF Gimbal

Now, in order to obtain the equations of motion, we write the Newton-Euler equations for inner and outer gimbal axes;

Newton's equation for inner gimbal

$$m_I \vec{a}_{C_I} = \vec{F}_{OI} + m_I \vec{g} \tag{2.55}$$

where;

m_I: mass of inner gimbal

$\vec{a}_{C_I}$: acceleration of the COG of inner gimbal

$\vec{F}_{OI}$: force applied by outer gimbal on inner gimbal

$\vec{g}$: gravity vector

Newton's equation for outer gimbal

$$m_O \vec{a}_{C_O} = \vec{F}_{BO} + \vec{F}_{IO} + m_O \vec{g} \tag{2.56}$$

where;

m_O: mass of outer gimbal

$\vec{a}_{C_O}$: acceleration of the COG of outer gimbal

$\vec{F}_{BO}$: force applied by gimbal base on outer gimbal

$\vec{F}_{IO}$: force applied by inner gimbal on outer gimbal

Euler's equation for inner gimbal about point O (intersection of rotation axes of inner and outer gimbal)

$$\breve{J}_I \cdot \vec{\alpha}_I + \vec{\omega}_I \times \breve{J}_I \cdot \vec{\omega}_I = \vec{M}_{OI} + \vec{r}_{OC_I} \times (m_I \vec{g}) + \vec{D}_I \tag{2.57}$$

where;

$\breve{J}_I$: inertia tensor of the inner gimbal

$\vec{\alpha}_I$: angular acceleration of the inner gimbal frame with respect to inertial frame

$\vec{\omega}_I$: angular velocity of the inner gimbal frame with respect to inertial frame

$\vec{M}_{OI}$: moment applied by outer gimbal on inner gimbal

$\vec{r}_{OC_I}$: position vector from point O to the COG of inner gimbal

$\vec{D}_I$: disturbance moments effecting on the inner gimbal

Euler's equation for outer gimbal about point O (intersection of rotation axes of inner and outer gimbal)

$$\breve{J}_O \cdot \vec{\alpha}_O + \vec{\omega}_O \times \breve{J}_O \cdot \vec{\omega}_O = \vec{M}_{BO} + \vec{M}_{IO} + \vec{r}_{OC_O} \times (m_O \vec{g}) + \vec{D}_O \tag{2.58}$$

where;

$\breve{J}_O$: inertia tensor of the outer gimbal

$\vec{\alpha}_O$: angular acceleration of the outer gimbal frame with respect to inertial frame

$\vec{\omega}_O$: angular velocity of the outer gimbal frame with respect to inertial frame

$\vec{M}_{BO}$: moment applied by gimbal base on outer gimbal

$\vec{M}_{IO}$: moment applied by inner gimbal on outer gimbal

$\vec{r}_{OC_O}$: position vector from point O to the COG of outer gimbal

$\vec{D}_O$: disturbance moments effecting on the outer gimbal

In our analysis from here on we will assume that the principal axes of inner and outer gimbals coincide with rotation directions, therefore the product of inertia terms in inertia matrices are zero and inertia matrices are diagonal for both inner and outer gimbals. In fact, this assumption is quite reasonable since the product of inertia terms of the inner and outer gimbals obtained from CAD models of the axes are very small.

Equations 2.55 and 2.56 can be used to obtain forces transferred through gimbal bearings as given below once the accelerations of COG's of inner and outer gimbals are obtained.

$$\vec{F}_{OI} = m_I \vec{a}_{C_I} - m_I \vec{g} \tag{2.59}$$

$$\vec{F}_{BO} = m_O \vec{a}_{C_O} - \vec{F}_{IO} - m_O \vec{g} \tag{2.60}$$

However, we are not interested in these force equations in our analysis and will not make use of Equations 2.59 and 2.60 above because these linear forces do not create any net torque in neither azimuth nor elevation axis since they act through the center of rotations in both axes.

On the other hand, Equations 2.57 and 2.58 can be decomposed into 6 scalar equations, four of which will give reaction moments on gimbal bearings in directions the bearings are not allowed to turn. These equations can be useful for strength calculations of the bearings but are not relevant for our analysis. The other two equations give the equations of motion for inner and outer gimbals, which we are after.

For the solution of equations of motion, all vector and matrix quantities in both equation 2.57 and 2.58 have to be represented in a single coordinate frame chosen for that equation. Therefore, we make this selection as follows; all terms of equation 2.57 in inner gimbal coordinate frame and all terms in equation 2.58 in outer gimbal coordinate frame. As a result of this coordinate frame selection, inertia matrices for both gimbal axes will remain constant since they are represented in their own respective coordinate frames.

First, we start with representing the angular velocity of outer gimbal coordinate frame relative to inertial frame $\vec{\omega}_{O/e}$, represented in outer gimbal coordinate frame (O).

$$\vec{\omega}_{O/e} = \vec{\omega}_{O/B} + \vec{\omega}_{B/n} + \vec{\omega}_{n/m} + \vec{\omega}_{m/e}$$

$$\{\vec{\omega}_{O/e}\}^{(O)} = \overline{\omega}_{O/e}^{(O)} = \dot{\eta}\overline{u}_3^{(O/O)} + \dot{\phi}\overline{u}_1^{(B/O)} + \dot{\theta}\overline{u}_2^{(n/O)} + \dot{\psi}\overline{u}_3^{(m/O)}$$

Therefore

$$\overline{\omega}_{O/e}^{(O)} = \dot{\eta}\overline{u}_3^{(O/O)} + \dot{\phi}\hat{C}^{(O,B)}\overline{u}_1^{(B/B)} + \dot{\theta}\hat{C}^{(O,n)}\overline{u}_2^{(n/n)} + \dot{\psi}\hat{C}^{(O,m)}\overline{u}_1^{(m/m)}$$

where

$$\hat{C}^{(O,n)} = \hat{C}^{(O,B)}\hat{C}^{(B,n)}$$

$$\hat{C}^{(O,m)} = \hat{C}^{(O,B)}\hat{C}^{(B,n)}\hat{C}^{(n,m)}$$

Therefore;

$$\overline{\omega}_{O/e}^{(O)} = \dot{\eta}\overline{u}_3 + \dot{\phi}\hat{C}^{(O,B)}\overline{u}_1 + \dot{\theta}\hat{C}^{(O,B)}\hat{C}^{(B,n)}\overline{u}_2 + \dot{\psi}\hat{C}^{(O,B)}\hat{C}^{(B,n)}\hat{C}^{(n,m)}\overline{u}_3 \tag{2.61}$$

$$\hat{C}^{(O,B)} = \hat{C}^{(B,O)^T} = \begin{bmatrix} \cos(\eta) & \sin(\eta) & 0 \\ -\sin(\eta) & \cos(\eta) & 0 \\ 0 & 0 & 1 \end{bmatrix}$$

$$\hat{C}^{(B,n)} = \hat{C}^{(n,B)^T} = \begin{bmatrix} 1 & 0 & 0 \\ 0 & \cos(\phi) & \sin(\phi) \\ 0 & -\sin(\phi) & \cos(\phi) \end{bmatrix}$$

$$\hat{C}^{(n,m)} = \hat{C}^{(m,n)^T} = \begin{bmatrix} \cos(\theta) & 0 & -\sin(\theta) \\ 0 & 1 & 0 \\ \sin(\theta) & 0 & \cos(\theta) \end{bmatrix}$$

Second, we continue with representing the angular velocity of the inner gimbal coordinate frame relative to inertial frame $\overline{\omega_{I/e}}$, represented in inner gimbal coordinate frame (I).

$$\vec{\omega}_{I/e} = \vec{\omega}_{I/O} + \vec{\omega}_{O/e}$$

$$\{\vec{\omega}_{I/e}\}^{(I)} = \overline{\omega}_{I/e}^{(I)} = \dot{\epsilon}\overline{u}_2^{(I/I)} + \hat{C}^{(I,O)}\overline{\omega}_{O/e}^{(O)}$$

$$\begin{aligned}\overline{\omega}_{I/e}^{(I)} &= \dot{\epsilon}\overline{u}_2 + \dot{\eta}\hat{C}^{(I,O)}\overline{u}_3 + \dot{\phi}\hat{C}^{(I,O)}\hat{C}^{(O,B)}\overline{u}_1 + \dot{\theta}\hat{C}^{(I,O)}\hat{C}^{(O,B)}\hat{C}^{(B,n)}\overline{u}_2 \\ &+\dot{\psi}\hat{C}^{(I,O)}\hat{C}^{(O,B)}\hat{C}^{(B,n)}\hat{C}^{(n,m)}\overline{u}_3 \end{aligned} \tag{2.62}$$

$$\hat{C}^{(I,O)} = \hat{C}^{(O,I)^T} = \begin{bmatrix} \cos(\epsilon) & 0 & -\sin(\epsilon) \\ 0 & 1 & 0 \\ \sin(\epsilon) & 0 & \cos(\epsilon) \end{bmatrix}$$

Now we can proceed with the angular acceleration terms appearing in the equations. Acceleration terms can be obtained by taking time derivative of angular velocity terms, starting with the outer gimbal equation

$$\vec{\alpha}_{O/e} = D_O\vec{\omega}_{O/e} = D_e\vec{\omega}_{O/e}$$

Since the angular velocity term for outer gimbal is obtained in outer gimbal reference frame, outer gimbal frame will be chosen for its simplicity. Taking the time derivative in outer gimbal reference frame results in

$$\begin{aligned}\overline{\alpha}_{O/e}^{(O)} &= \ddot{\eta}\overline{u}_3 + \ddot{\phi}\hat{C}^{O,B}\overline{u}_1 + \dot{\phi}\dot{\hat{C}}^{O,B}\overline{u}_1 + \ddot{\theta}\hat{C}^{(O,B)}\hat{C}^{(B,n)}\overline{u}_2 + \dot{\theta}\dot{\hat{C}}^{(O,B)}\hat{C}^{(B,n)}\overline{u}_2 \\ &+\dot{\theta}\hat{C}^{(O,B)}\dot{\hat{C}}^{(B,n)}\overline{u}_2 + \ddot{\psi}\hat{C}^{(O,B)}\hat{C}^{(B,n)}\hat{C}^{(n,m)}\overline{u}_3 + \dot{\psi}\dot{\hat{C}}^{(O,B)}\hat{C}^{(B,n)}\hat{C}^{(n,m)}\overline{u}_3 \\ &+\dot{\psi}\hat{C}^{(O,B)}\dot{\hat{C}}^{(B,n)}\hat{C}^{(n,m)}\overline{u}_3 + \dot{\psi}\hat{C}^{(O,B)}\hat{C}^{(B,n)}\dot{\hat{C}}^{(n,m)}\overline{u}_3 \end{aligned} \tag{2.63}$$

Next, we obtain the angular acceleration term for the inner gimbal by taking the time derivative of angular velocity term for it

$$\vec{\alpha}_{I/e} = D_I\vec{\omega}_{I/e} = D_e\vec{\omega}_{I/e}$$

Likewise, since the angular velocity term for inner gimbal is obtained in inner gimbal reference frame, inner gimbal frame will be chosen for its simplicity. Taking the

time derivative in inner gimbal reference frame results in the following rather lengthy equation

$$\begin{aligned}\bar{\alpha}_{I/e}^{(I)} = {} & \ddot{\epsilon}\bar{u}_2 + \ddot{\eta}\hat{C}^{(I,O)}\bar{u}_3 + \dot{\eta}\dot{\hat{C}}^{(I,O)}\bar{u}_3 + \ddot{\phi}\hat{C}^{(I,O)}\hat{C}^{(O,B)}\bar{u}_1 + \dot{\phi}\dot{\hat{C}}^{(I,O)}\hat{C}^{(O,B)}\bar{u}_1 \\ & + \dot{\phi}\hat{C}^{(I,O)}\dot{\hat{C}}^{(O,B)}\bar{u}_1 + \ddot{\theta}\hat{C}^{(I,O)}\hat{C}^{(O,B)}\hat{C}^{(B,n)}\bar{u}_2 + \dot{\theta}\dot{\hat{C}}^{(I,O)}\hat{C}^{(O,B)}\hat{C}^{(B,n)}\bar{u}_2 \\ & + \dot{\theta}\hat{C}^{(I,O)}\dot{\hat{C}}^{(O,B)}\hat{C}^{(B,n)}\bar{u}_2 + \dot{\theta}\hat{C}^{(I,O)}\hat{C}^{(O,B)}\dot{\hat{C}}^{(B,n)}\bar{u}_2 + \ddot{\psi}\hat{C}^{(I,O)}\hat{C}^{(O,B)}\hat{C}^{(B,n)}\hat{C}^{(n,m)}\bar{u}_3 \\ & + \dot{\psi}\dot{\hat{C}}^{(I,O)}\hat{C}^{(O,B)}\hat{C}^{(B,n)}\hat{C}^{(n,m)}\bar{u}_3 + \dot{\psi}\hat{C}^{(I,O)}\dot{\hat{C}}^{(O,B)}\hat{C}^{(B,n)}\hat{C}^{(n,m)}\bar{u}_3 \\ & + \dot{\psi}\hat{C}^{(I,O)}\hat{C}^{(O,B)}\dot{\hat{C}}^{(B,n)}\hat{C}^{(n,m)}\bar{u}_3 + \dot{\psi}\hat{C}^{(I,O)}\hat{C}^{(O,B)}\hat{C}^{(B,n)}\dot{\hat{C}}^{(n,m)}\bar{u}_3 \end{aligned} \tag{2.64}$$

With this, the terms on the left hand side of the equations are represented in their corresponding coordinate frames. We continue with the terms on the right hand side.

Gravity vector is defined in the inertial coordinate frame as

$$\{\vec{g}\}^{(e)} = -g\bar{u}_3^{(e/e)} = -g\bar{u}_3 \tag{2.65}$$

However, this vector needs to be presented in (O) and (I) coordinate frames for Euler equations for outer and inner gimbals, respectively. Transformations to these coordinate frames can be done as follows, starting with outer gimbal coordinate frame

$$\{\vec{g}\}^{(O)} = \bar{g}^{(O)} = -g\bar{u}_3^{(e/O)} = -g\hat{C}^{(O,B)}\hat{C}^{(B,n)}\hat{C}^{(n,m)}\hat{C}^{(m,e)}\bar{u}_3^{(e,e)}$$

$$\bar{g}^{(O)} = -g\begin{bmatrix} -\cos(\eta)\sin(\theta) + \sin(\eta)\sin(\phi)\cos(\theta) \\ \sin(\eta)\sin(\theta) + \cos(\eta)\sin(\phi)\cos(\theta) \\ \cos(\phi)\cos(\theta) \end{bmatrix} \tag{2.66}$$

and carrying on with inner gimbal coordinate frame

$$\{\vec{g}\}^{(I)} = \bar{g}^{(I)} = \hat{C}^{(I,O)}\bar{g}^{(O)} = -g\hat{C}^{(I,O)}\hat{C}^{(O,B)}\hat{C}^{(B,n)}\hat{C}^{(n,m)}\hat{C}^{(m,e)}\bar{u}_3^{(e,e)}$$

$$\bar{g}^{(O)} = -g\begin{bmatrix} -\cos(\eta)\sin(\theta)\cos(\epsilon) + \sin(\eta)\sin(\phi)\cos(\theta)\cos(\epsilon) - \cos(\phi)\cos(\theta)\sin(\epsilon) \\ \sin(\eta)\sin(\theta) + \cos(\eta)\sin(\phi)\cos(\theta) \\ -\cos(\eta)\sin(\theta)\sin(\epsilon) + \sin(\eta)\sin(\phi)\cos(\theta)\sin(\epsilon) + \cos(\phi)\cos(\theta)\cos(\epsilon) \end{bmatrix} \tag{2.67}$$

Gravity vector is transformed to relevant coordinate frames above, we continue with the distance vectors $\vec{r}_{OC_O}$ and $\vec{r}_{OC_I}$. These distance vectors will be constant vectors if

they are represented in their corresponding body frames, namely $\vec{r}_{OC_O}$ in outer gimbal coordinate frame and $\vec{r}_{OC_I}$ in inner gimbal coordinate frame. The reason for this is, the fact that they represent the distance between the two points on the same rigid body and when a coordinate frame fixed to this same body is used, this vector remains the same as long as the rigidity assumption for the body holds true. Therefore we define $\vec{r}_{OC_O}$ and $\vec{r}_{OC_I}$ as follows

$$\{\vec{r}_{OC_O}\}^{(O)} = \begin{bmatrix} l_1 \\ l_2 \\ l_3 \end{bmatrix} \tag{2.68}$$

$$\{\vec{r}_{OC_I}\}^{(I)} = \begin{bmatrix} k_1 \\ k_2 \\ k_3 \end{bmatrix} \tag{2.69}$$

Next, disturbance terms are defined based on the assumption that the only components that exist are the ones acting in the directions of rotation of the corresponding gimbal axis; therefore

$$\{\vec{D}_O\}^{(O)} = D_O \bar{u}_3 \tag{2.70}$$

$$\{\vec{D}_I\}^{(I)} = D_I \bar{u}_2 \tag{2.71}$$

Finally, the terms $\vec{M}_{BO}$ and $\vec{M}_{OI}$ will be defined as follows; since the joint between the base and the outer gimbal is rotating in $\bar{u}_3^{(B)} = \bar{u}_3^{(O)}$ direction, the torque transferred in this direction is the motor torque plus bearing friction, which can be modeled as $T_{m_{BO}} + T_{fr_{BO}}$ where $T_{m_{BO}}$ is the motor torque transmitted and $T_{fr_{BO}}$ is the friction torque between base and outer gimbal. In the remaining two directions, reaction moments are transferred. Likewise, the joint between outer gimbal and inner gimbal is rotating in $\bar{u}_2^{(O)} = \bar{u}_2^{(I)}$ direction and in this direction a torque equal to motor torque plus bearing friction is transferred. In a similar manner, this torque can be represented as $T_{m_{OI}} + T_{fr_{OI}}$ where $T_{m_{OI}}$ is the motor torque transmitted and $T_{fr_{OI}}$ is the friction torque between outer and inner gimbals. The moments transferred in the remaining two directions are reaction moments.

$$\{\vec{M}_{BO}\}^{(O)} = \begin{bmatrix} M_{BO_1} \\ M_{BO_2} \\ T_{m_{BO}} + T_{fr_{BO}} \end{bmatrix} \tag{2.72}$$

$$\{\vec{M}_{OI}\}^{(I)} = \begin{bmatrix} M_{OI_1} \\ T_{m_{OI}} + T_{fr_{OI}} \\ M_{OI_3} \end{bmatrix} \tag{2.73}$$

2.2.1 Simplification of the Mathematical Model

The mathematical model obtained in the previous section fully describes the gimbal platform taking into account all possible terms including rotational base movements in all directions, unbalance effects, inertial terms that develop as a result of relative motions of the two gimbal axes and external disturbances. Although this detailed model including all the above terms will be constructed in Matlab/Simulink and Sim-Mechanics for simulation purposes, a simpler model is needed in order to be used in analytical work for developing the required theoretical background. In the following subsections, decoupling assumption of the equations of motion belonging to the two rotation axes will be justified first and once this assumption is validated, these simpler mathematical models will be obtained for azimuth and elevation axis stabilization problems separately.

2.2.1.1 Validation of the Uncoupled Rotation Axes Assumption

As discussed before, the gimbal platform that is going to be stabilized has two rotation axes which can be controlled separately. However, in order to see if two separate controllers can be implemented to control the two axes, these axes must be proven to be uncoupled from each other. This section discusses the validity of such an assumption.

For the sake of convenience let the following assumptions be valid;

- $\psi(t) = 0$, $\theta(t) = 0$, and $\phi(t) = 0$, meaning that there exists no disturbance of the base and both azimuth and elevation axes of the gimbal are free to move.

- $\vec{r}_{OC_O}$ and $\vec{r}_{OC_I}$ lengths are zero, meaning both outer and inner gimbal centers of rotation and centers of gravity are coincident, therefore no static or dynamic unbalance torque acts on both inner and outer gimbals.

- $\hat{J}_O^{(O)} = \begin{bmatrix} J_{O_1} & 0 & 0 \\ 0 & J_{O_2} & 0 \\ 0 & 0 & J_{O_3} \end{bmatrix}$

- $\hat{J}_I^{(I)} = \begin{bmatrix} J_{I_1} & 0 & 0 \\ 0 & J_{I_2} & 0 \\ 0 & 0 & J_{I_3} \end{bmatrix}$

- $\bar{M}_{BO}^{(O)} = \begin{bmatrix} M_{BO_1} \\ M_{BO_2} \\ T_{m_O} + T_{fr_O} \end{bmatrix}$

- $\bar{M}_{OI}^{(I)} = \begin{bmatrix} M_{OI_1} \\ T_{m_I} + T_{fr_I} \\ M_{OI_3} \end{bmatrix}$

- $\bar{M}_{IO}^{(O)} = \begin{bmatrix} M_{IO_1} \\ M_{IO_2} \\ M_{IO_3} \end{bmatrix}$

- $\bar{D}_O^{(O)} = \begin{bmatrix} 0 \\ 0 \\ D_O \end{bmatrix}$

- $\bar{D}_I^{(I)} = \begin{bmatrix} 0 \\ D_I \\ 0 \end{bmatrix}$

With these assumptions, angular velocity and angular acceleration terms for azimuth and elevation axes can be simplified as follows

$$\begin{aligned} \bar{\omega}_{O/e}^{(O)} &= \dot{\eta}\bar{u}_3 + \underbrace{\dot{\phi}\hat{C}^{(O,B)}\bar{u}_1}_{0} + \underbrace{\dot{\theta}\hat{C}^{(O,B)}\hat{C}^{(B,n)}\bar{u}_2}_{0} + \underbrace{\dot{\psi}\hat{C}^{(O,B)}\hat{C}^{(B,n)}\hat{C}^{(n,m)}\bar{u}_3}_{0} \\ &= \dot{\eta}\bar{u}_3 \end{aligned} \tag{2.74}$$

$$
\begin{aligned}
\bar{\alpha}^{(O)}_{O/e} &= \ddot{\eta}\bar{u}_3 + \underbrace{\ddot{\phi}\hat{C}^{O,B}\bar{u}_1}_{0} + \underbrace{\dot{\phi}\dot{\hat{C}}^{O,B}\bar{u}_1}_{0} + \underbrace{\ddot{\theta}\hat{C}^{(O,B)}\hat{C}^{(B,n)}\bar{u}_2}_{0} + \underbrace{\dot{\theta}\dot{\hat{C}}^{(O,B)}\hat{C}^{(B,n)}\bar{u}_2}_{0} \\
&\quad + \underbrace{\dot{\theta}\hat{C}^{(O,B)}\dot{\hat{C}}^{(B,n)}\bar{u}_2}_{0} + \underbrace{\ddot{\psi}\hat{C}^{(O,B)}\hat{C}^{(B,n)}\hat{C}^{(n,m)}\bar{u}_3}_{0} + \underbrace{\dot{\psi}\dot{\hat{C}}^{(O,B)}\hat{C}^{(B,n)}\hat{C}^{(n,m)}\bar{u}_3}_{0} \\
&\quad + \underbrace{\dot{\psi}\hat{C}^{(O,B)}\dot{\hat{C}}^{(B,n)}\hat{C}^{(n,m)}\bar{u}_3}_{0} + \underbrace{\dot{\psi}\hat{C}^{(O,B)}\hat{C}^{(B,n)}\dot{\hat{C}}^{(n,m)}\bar{u}_3}_{0} \\
&= \ddot{\eta}\bar{u}_3
\end{aligned}
$$

$$
\begin{aligned}
\bar{\omega}^{(I)}_{I/e} &= \dot{\epsilon}\bar{u}_2 + \dot{\eta}\hat{C}^{(I,O)}\bar{u}_3 + \underbrace{\dot{\phi}\hat{C}^{(I,O)}\hat{C}^{(O,B)}\bar{u}_1}_{0} + \underbrace{\dot{\theta}\hat{C}^{(I,O)}\hat{C}^{(O,B)}\hat{C}^{(B,n)}\bar{u}_2}_{0} \\
&\quad + \underbrace{\dot{\psi}\hat{C}^{(I,O)}\hat{C}^{(O,B)}\hat{C}^{(B,n)}\hat{C}^{(n,m)}\bar{u}_3}_{0} \\
&= \dot{\epsilon}\bar{u}_2 + \dot{\eta}\hat{C}^{(I,O)}\bar{u}_3
\end{aligned}
$$

$$
\begin{aligned}
\bar{\alpha}^{(I)}_{I/e} &= \ddot{\epsilon}\bar{u}_2 + \ddot{\eta}\hat{C}^{(I,O)}\bar{u}_3 + \dot{\eta}\dot{\hat{C}}^{(I,O)}\bar{u}_3 + \underbrace{\ddot{\phi}\hat{C}^{(I,O)}\hat{C}^{(O,B)}\bar{u}_1}_{0} + \underbrace{\dot{\phi}\dot{\hat{C}}^{(I,O)}\hat{C}^{(O,B)}\bar{u}_1}_{0} \\
&\quad + \underbrace{\dot{\phi}\hat{C}^{(I,O)}\dot{\hat{C}}^{(O,B)}\bar{u}_1}_{0} + \underbrace{\ddot{\theta}\hat{C}^{(I,O)}\hat{C}^{(O,B)}\hat{C}^{(B,n)}\bar{u}_2}_{0} + \underbrace{\dot{\theta}\dot{\hat{C}}^{(I,O)}\hat{C}^{(O,B)}\hat{C}^{(B,n)}\bar{u}_2}_{0} \\
&\quad + \underbrace{\dot{\theta}\hat{C}^{(I,O)}\dot{\hat{C}}^{(O,B)}\hat{C}^{(B,n)}\bar{u}_2}_{0} + \underbrace{\dot{\theta}\hat{C}^{(I,O)}\hat{C}^{(O,B)}\dot{\hat{C}}^{(B,n)}\bar{u}_2}_{0} + \underbrace{\ddot{\psi}\hat{C}^{(I,O)}\hat{C}^{(O,B)}\hat{C}^{(B,n)}\hat{C}^{(n,m)}\bar{u}_3}_{0} \\
&\quad + \underbrace{\dot{\psi}\dot{\hat{C}}^{(I,O)}\hat{C}^{(O,B)}\hat{C}^{(B,n)}\hat{C}^{(n,m)}\bar{u}_3}_{0} + \underbrace{\dot{\psi}\hat{C}^{(I,O)}\dot{\hat{C}}^{(O,B)}\hat{C}^{(B,n)}\hat{C}^{(n,m)}\bar{u}_3}_{0} \\
&\quad + \underbrace{\dot{\psi}\hat{C}^{(I,O)}\hat{C}^{(O,B)}\dot{\hat{C}}^{(B,n)}\hat{C}^{(n,m)}\bar{u}_3}_{0} + \underbrace{\dot{\psi}\hat{C}^{(I,O)}\hat{C}^{(O,B)}\hat{C}^{(B,n)}\dot{\hat{C}}^{(n,m)}\bar{u}_3}_{0} \\
&= \ddot{\epsilon}\bar{u}_2 + \ddot{\eta}\hat{C}^{(I,O)}\bar{u}_3 + \dot{\eta}\dot{\hat{C}}^{(I,O)}\bar{u}_3
\end{aligned}
$$

If we rewrite Euler's equation for azimuth axis

$$
\breve{J}_O \cdot \vec{\alpha_O} + \vec{\omega}_O \times \breve{J}_O \cdot \vec{\omega}_O = \vec{M}_{BO} + \vec{M}_{IO} + \vec{r}_{OC_O} \times (m_O\vec{g}) + \vec{D}_O
$$

and substitute the above terms into the equation, we obtain

$$
\begin{aligned}
&\begin{bmatrix} J_{O_1} & 0 & 0 \\ 0 & J_{O_2} & 0 \\ 0 & 0 & J_{O_3} \end{bmatrix}\begin{bmatrix} 0 \\ 0 \\ \ddot{\eta} \end{bmatrix} + \begin{bmatrix} 0 \\ 0 \\ \dot{\eta} \end{bmatrix} \times \begin{bmatrix} J_{O_1} & 0 & 0 \\ 0 & J_{O_2} & 0 \\ 0 & 0 & J_{O_3} \end{bmatrix}\begin{bmatrix} 0 \\ 0 \\ \dot{\eta} \end{bmatrix} \\
&\qquad = \begin{bmatrix} M_{BO_1} \\ M_{BO_2} \\ T_{m_O} + T_{fr_O} \end{bmatrix} + \begin{bmatrix} M_{IO_1} \\ M_{IO_2} \\ M_{IO_3} \end{bmatrix} + \begin{bmatrix} 0 \\ 0 \\ D_O \end{bmatrix} \qquad (2.75)
\end{aligned}
$$

This matrix equation can be decomposed into three scalar equations

$$M_{BO_1} + M_{IO_1} = 0 \tag{2.76}$$

$$M_{BO_2} + M_{IO_2} = 0 \tag{2.77}$$

$$J_{O_3}\ddot{\eta} = T_{m_O} + T_{fr_O} + M_{IO_3} + D_O \tag{2.78}$$

Equation 2.78 is the equation of motion for azimuth axis, however the term M_{IO_3} needs to be calculated from the elevation axis equations therefore we proceed with the elevation axis. If we rewrite the Euler's equation for elevation axis

$$\check{J}_I \cdot \vec{\alpha}_I + \vec{\omega}_I \times \check{J}_I \cdot \vec{\omega}_I = \vec{M}_{OI} + \vec{r}_{OC_I} \times (m_I\vec{g}) + \vec{D}_I$$

and substitute the above terms into the equation, we obtain

$$\begin{bmatrix} J_{I_1} & 0 & 0 \\ 0 & J_{I_2} & 0 \\ 0 & 0 & J_{I_3} \end{bmatrix} \begin{bmatrix} -\dot{\epsilon}\dot{\eta}\cos(\epsilon) - \ddot{\eta}\sin(\epsilon) \\ \ddot{\epsilon} \\ -\dot{\epsilon}\dot{\eta}\sin(\epsilon) + \ddot{\eta}\cos(\epsilon) \end{bmatrix} + \begin{bmatrix} -\dot{\eta}\sin(\epsilon) \\ \dot{\epsilon} \\ \dot{\eta}\cos(\epsilon) \end{bmatrix} \times \begin{bmatrix} J_{I_1} & 0 & 0 \\ 0 & J_{I_2} & 0 \\ 0 & 0 & J_{I_3} \end{bmatrix} \begin{bmatrix} -\dot{\eta}\sin(\epsilon) \\ \dot{\epsilon} \\ \dot{\eta}\cos(\epsilon) \end{bmatrix}$$
$$\begin{bmatrix} M_{OI_1} \\ T_{m_I} + T_{fr_I} \\ M_{OI_3} \end{bmatrix} + \begin{bmatrix} 0 \\ D_I \\ 0 \end{bmatrix} \tag{2.79}$$

This matrix equation can be decomposed into three scalar equations

$$-J_{I_1}(\dot{\epsilon}\dot{\eta}\cos\epsilon + \ddot{\eta}\sin\epsilon) + (J_{I_3} - J_{I_2})(\dot{\epsilon}\dot{\eta}\cos\epsilon) = M_{OI_1} \tag{2.80}$$

$$J_{I_2}\ddot{\epsilon} + \dot{\eta}^2\sin\epsilon\cos\epsilon(J_{I_3} - J_{I_1}) = T_{m_I} + T_{fr_I} + D_I \tag{2.81}$$

$$J_{I_3}(-\dot{\epsilon}\dot{\eta}\sin\epsilon + \ddot{\eta}\cos\epsilon) + (J_{I_1} - J_{I_2})(\dot{\epsilon}\dot{\eta}\sin\epsilon) = M_{OI_3} \tag{2.82}$$

Resulting Equation 2.81 is the equation of motion for the inner gimbal axis. Equations 2.80 and 2.82 will be used for determining M_{IO_3}.

Following can be written for the term $\bar{M}_{IO}$ using the third law of Newton.

$$-\bar{M}_{IO}^{O} = \hat{C}^{(O,I)}\bar{M}_{OI}^{I} \tag{2.83}$$

where

$$\hat{C}^{(O,I)} = \begin{bmatrix} \cos(\epsilon) & 0 & \sin(\epsilon) \\ 0 & 1 & 0 \\ -\sin(\epsilon) & 0 & \cos(\epsilon) \end{bmatrix}$$

The only term that needs to be found is the M_{IO_3} term, which can be written as follows using the above equations.

$$M_{IO_3} = -J_{I_1}(\dot{\epsilon}\dot{\eta}\cos(\epsilon) + \ddot{\eta}\sin(\epsilon))\sin(\epsilon) - J_{I_3}(-\dot{\epsilon}\dot{\eta}\sin(\epsilon) + \ddot{\eta}\cos(\epsilon))\cos(\epsilon)$$
$$+(J_{I_1} - J_{I_3})(\dot{\epsilon}\dot{\eta}\cos(\epsilon)\sin(\epsilon)) \tag{2.84}$$

It is important to note that this term represents the inertia of the elevation axis in the azimuth axis equation motion since when azimuth axis is being actuated, elevation axis also moves with it. To see this more clearly, let the elevation angle ϵ be zero. In this case M_{IO_3} becomes equal to $-J_{I_3}\ddot{\eta}$. Likewise, when elevation angle is set to be equal to $\frac{\pi}{2}$, M_{IO_3} becomes equal to $-J_{I_1}\ddot{\eta}$. At zero elevation axis, the third term of inner gimbal inertia matrix is directly added to the third term of the outer gimbal inertia matrix since both coordinate frame directions coincide. However, as the elevation angle changes, so does the contribution of the elevation inertial to the total inertia and at $\epsilon = \frac{\pi}{2}$, the outer gimbal third unit vector direction is coincident with inner gimbal first unit vector direction, therefore at this elevation angle the first diagonal of the inner gimbal inertia matrix is added to the third diagonal of the outer gimbal inertia matrix, as expected.

The M_{IO_3} term causes ϵ to show up in azimuth axis equations however this coupling effect, which is also described in the previous paragraph is very weak and can be neglected. Once this weak coupling effect is neglected, the following equation of motion belonging to the azimuth axis becomes independent of the elevation axis motion.

$$\ddot{\eta} = \frac{T_{m_O} + T_{fr_O} + M_{IO_3} + D_O}{J_{O_3}} \tag{2.85}$$

Likewise, when equation of motion of the elevation axis given in 2.86 is analyzed, a term containing the square of azimuth axis velocity is seen. However, since angular velocities are kept near zero in the course of stabilization, this condition holds as long as the azimuth axis controller can stabilize the azimuth axis with good performance, which holds under all but the most severe disturbances. Therefore, this squared angular velocity term becomes negligible and with this assumption elevation axis equation of motion becomes independent of azimuth axis motion.

$$\ddot{\epsilon} = \frac{T_{m_I} + T_{fr_I} + D_I - \dot{\eta}^2\sin(\epsilon)\cos(\epsilon)(J_{I_3} - J_{I_1})}{J_{I_2}} \tag{2.86}$$

As a result, it is concluded that azimuth and elevation axes can be considered as two independent plants to be controlled and separate controllers can be designed for each of them. Therefore, from now on stabilization problem is handled separately for both axes. Next two subsections explain the simplification of equations of motions for both azimuth and elevation axes and it is also the first place in which uncoupled axes assumption is used.

2.2.1.2 Simplification of the Azimuth Axis Equation of Motion

We start with rewriting Equation 2.58, the already given Euler equation for azimuth axis

$$\check{J}_O \cdot \vec{\alpha_O} + \vec{\omega}_O \times \check{J}_O \cdot \vec{\omega}_O = \vec{M}_{BO} + \vec{M}_{IO} + \vec{r}_{OC_O} \times (m_O \vec{g}) + \vec{D}_O$$

Sticking with the previous coordinate frame definitions, let the following assumptions be valid;

- $\theta(t) = 0$, $\phi(t) = 0$, and $\epsilon(t) = 0$, meaning that there exists only the yaw disturbance on the base and only the outer gimbal motion is allowed, inner gimbal is rigidly fixed to the outer gimbal, restricting all movement between these two.
- $\vec{r}_{OC_O}$ length is zero, meaning outer gimbal center of rotation and center of gravity are coincident, therefore no static or dynamic unbalance torque acts on the outer gimbal.
- $\hat{J}_O^{(O)} = \begin{bmatrix} J_{O_1} & 0 & 0 \\ 0 & J_{O_2} & 0 \\ 0 & 0 & J_{O_3} \end{bmatrix}$
- $\bar{M}_{BO}^{(O)} = \begin{bmatrix} M_{BO_1} \\ M_{BO_2} \\ T_{m_O} + T_{fr_O} \end{bmatrix}$
- $\bar{D}_O^{(O)} = \begin{bmatrix} 0 \\ 0 \\ D_O \end{bmatrix}$

As long as the above assumptions hold, angular velocity and angular acceleration terms simplify as follows

$$\begin{aligned}\bar{\omega}_{O/e}^{(O)} &= \dot{\eta}\bar{u}_3 + \underbrace{\dot{\phi}\hat{C}^{(O,B)}\bar{u}_1}_{0} + \underbrace{\dot{\theta}\hat{C}^{(O,B)}\hat{C}^{(B,n)}\bar{u}_2}_{0} + \dot{\psi}\hat{C}^{(O,B)}\underbrace{\hat{C}^{(B,n)}}_{\hat{I}}\underbrace{\hat{C}^{(n,m)}}_{\hat{I}}\bar{u}_3 \\ &= \dot{\eta}\bar{u}_3 + \dot{\psi}\hat{C}^{(O,B)}\hat{I}\hat{I}\bar{u}_3\end{aligned}$$

where

$$\hat{C}^{(O,B)} = \begin{bmatrix} \cos(\eta) & \sin(\eta) & 0 \\ -\sin(\eta) & \cos(\eta) & 0 \\ 0 & 0 & 1 \end{bmatrix}$$

Therefore, the angular velocity term becomes

$$\bar{\omega}_{O/e}^{(O)} = (\dot{\eta} + \dot{\psi})\bar{u}_3 \tag{2.87}$$

Furthermore

$$\begin{aligned}\bar{\alpha}_{O/e}^{(O)} &= \ddot{\eta}\bar{u}_3 + \underbrace{\ddot{\phi}\hat{C}^{O,B}\bar{u}_1}_{0} + \underbrace{\dot{\phi}\dot{\hat{C}}^{O,B}\bar{u}_1}_{0} + \underbrace{\ddot{\theta}\hat{C}^{(O,B)}\hat{C}^{(B,n)}\bar{u}_2}_{0} + \underbrace{\dot{\theta}\dot{\hat{C}}^{(O,B)}\hat{C}^{(B,n)}\bar{u}_2}_{0} \\ &\quad + \underbrace{\dot{\theta}\hat{C}^{(O,B)}\dot{\hat{C}}^{(B,n)}\bar{u}_2}_{0} + \ddot{\psi}\hat{C}^{(O,B)}\underbrace{\hat{C}^{(B,n)}}_{\hat{I}}\underbrace{\hat{C}^{(n,m)}}_{\hat{I}}\bar{u}_3 + \dot{\psi}\dot{\hat{C}}^{(O,B)}\underbrace{\hat{C}^{(B,n)}}_{\hat{I}}\underbrace{\hat{C}^{(n,m)}}_{\hat{I}}\bar{u}_3 \\ &\quad + \underbrace{\dot{\psi}\hat{C}^{(O,B)}\dot{\hat{C}}^{(B,n)}\hat{C}^{(n,m)}\bar{u}_3}_{0} + \underbrace{\dot{\psi}\hat{C}^{(O,B)}\hat{C}^{(B,n)}\dot{\hat{C}}^{(n,m)}\bar{u}_3}_{0} \\ &= \ddot{\eta}\bar{u}_3 + \ddot{\psi}\hat{C}^{(O,B)}\hat{I}\hat{I}\bar{u}_3 + \dot{\psi}\dot{\hat{C}}^{(O,B)}\hat{I}\hat{I}\bar{u}_3\end{aligned}$$

where;

$$\hat{C}^{(O,B)} = \begin{bmatrix} \cos(\eta) & \sin(\eta) & 0 \\ -\sin(\eta) & \cos(\eta) & 0 \\ 0 & 0 & 1 \end{bmatrix}$$

$$\dot{\hat{C}}^{(O,B)} = \begin{bmatrix} -\sin(\eta)\dot{\eta} & \cos(\eta)\dot{\eta} & 0 \\ -\cos(\eta)\dot{\eta} & -\sin(\eta)\dot{\eta} & 0 \\ 0 & 0 & 0 \end{bmatrix}$$

Therefore, the angular acceleration term becomes

$$\bar{\alpha}_{O/e}^{(O)} = (\ddot{\eta} + \ddot{\psi})\bar{u}_3 \tag{2.88}$$

Substituting all terms into the Euler equation for the outer gimbal gives

$$\begin{bmatrix} J_{O_1} & 0 & 0 \\ 0 & J_{O_2} & 0 \\ 0 & 0 & J_{O_3} \end{bmatrix} \begin{bmatrix} 0 \\ 0 \\ (\ddot{\eta} + \ddot{\psi}) \end{bmatrix} + \begin{bmatrix} 0 \\ 0 \\ (\dot{\eta} + \dot{\psi}) \end{bmatrix} \times \begin{bmatrix} J_{O_1} & 0 & 0 \\ 0 & J_{O_2} & 0 \\ 0 & 0 & J_{O_3} \end{bmatrix} \begin{bmatrix} 0 \\ 0 \\ (\dot{\eta} + \dot{\psi}) \end{bmatrix}$$

$$= \begin{bmatrix} M_{BO_1} \\ M_{BO_2} \\ T_{m_O} + T_{fr_O} \end{bmatrix} + \begin{bmatrix} M_{IO_1} \\ M_{IO_2} \\ M_{IO_3} \end{bmatrix} + \begin{bmatrix} 0 \\ 0 \\ D_O \end{bmatrix} \quad (2.89)$$

This matrix equation can be decomposed into three scalar equations

$$M_{BO_1} + M_{IO_1} = 0 \quad (2.90)$$

$$M_{BO_2} + M_{IO_2} = 0 \quad (2.91)$$

$$J_{O_3}(\ddot{\eta} + \ddot{\psi}) = T_{m_O} + T_{fr_O} + M_{IO_3} + D_O \quad (2.92)$$

The last equation gives the equation of motion for the gimbal outer axis. Note that the M_{IO_3} term appearing in the equation is the contribution of inner gimbal inertia to the total inertia of inner and outer gimbals combined. Therefore the two terms can be lumped into a total inertia term J_{T_3} In Figure 2.5 below, a simple block diagram of the plant is drawn and some observations about the plant are given following the figure.

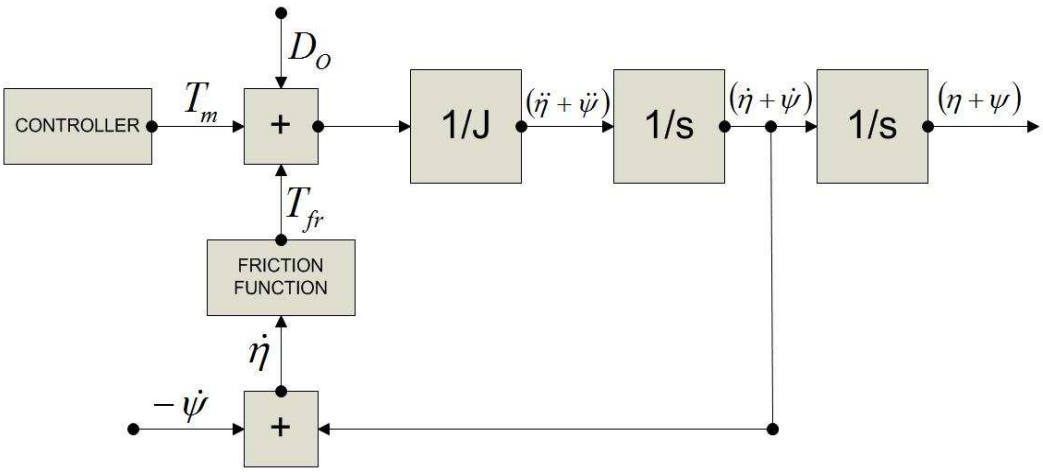

Figure 2.5: Plant Azimuth Axis Block Diagram

- Friction function can be selected as one of the many friction models presented in the literature. The model used in this thesis work is the Coulomb friction model, which is explained in Section 3.3.3.

- $(\dot{\eta} + \dot{\psi})$ is the angular velocity of elevation axis relative to inertial frame and it is directly measured by the gyroscopes.

- $(\ddot{\eta} + \ddot{\psi})$ is the angular acceleration of elevation axis relative to inertial frame and it is directly measured by accelerometers.

- The effect of base movement $\dot{\psi}$ on the gimbal is through the friction moment developing in the bearing as can be seen from the block diagram. This friction is a function of $\dot{\eta}$ which is the relative velocity in this bearing.

2.2.1.3 Simplification of the Elevation Axis Equation of Motion

We start with rewriting Equation 2.58, the already given Euler equation for elevation axis

$$\check{J}_I \cdot \vec{\alpha}_I + \vec{\omega}_I \times \check{J}_I \cdot \vec{\omega}_I = \vec{M}_{OI} + \vec{r}_{OC_I} \times (m_I \vec{g}) + \vec{D}_I$$

Sticking with the previous coordinate frame definitions, let the following assumptions be valid;

- $\psi(t) = 0$, $\phi(t) = 0$, and $\eta(t) = 0$, meaning that there exists only the pitch disturbance on the base and only the inner gimbal motion is allowed, outer gimbal is rigidly fixed, restricting all movement between the base and the outer gimbal.

- $\vec{r}_{OC_I}$ length is zero, meaning inner gimbal center of rotation and center of gravity are coincident, therefore no static or dynamic unbalance torque acts on the inner gimbal.

- $\hat{J}_I^{(I)} = \begin{bmatrix} J_{I_1} & 0 & 0 \\ 0 & J_{I_2} & 0 \\ 0 & 0 & J_{I_3} \end{bmatrix}$

- $\bar{M}_{OI}^{(I)} = \begin{bmatrix} M_{OI_1} \\ T_{m_I} + T_{fr_I} \\ M_{OI_3} \end{bmatrix}$

- $\bar{D}_{I}^{(I)} = \begin{bmatrix} 0 \\ D_I \\ 0 \end{bmatrix}$

As a result of the above assumptions, angular velocity and angular acceleration terms simplify as follows

$$\begin{aligned}
\bar{\omega}_{I/e}^{(I)} &= \dot{\epsilon}\bar{u}_2 + \underbrace{\dot{\eta}\hat{C}^{(I,O)}\bar{u}_3}_{0} + \underbrace{\dot{\phi}\hat{C}^{(I,O)}\hat{C}^{(O,B)}\bar{u}_1}_{0} + \dot{\theta}\hat{C}^{(I,O)}\underbrace{\hat{C}^{(O,B)}}_{\hat{I}}\underbrace{\hat{C}^{(B,n)}}_{\hat{I}}\bar{u}_2 \\
&\quad + \underbrace{\dot{\psi}\hat{C}^{(I,O)}\hat{C}^{(O,B)}\hat{C}^{(B,n)}\hat{C}^{(n,m)}\bar{u}_3}_{0} \\
&= \dot{\epsilon}\bar{u}_2 + \dot{\theta}\hat{C}^{(I,O)}\hat{I}\hat{I}\bar{u}_2
\end{aligned}$$

where;

$$\hat{C}^{(I,O)} = \begin{bmatrix} \cos(\epsilon) & 0 & -\sin(\epsilon) \\ 0 & 1 & 0 \\ \sin(\epsilon) & 0 & \cos(\epsilon) \end{bmatrix}$$

Therefore, the angular velocity term becomes

$$\bar{\omega}_{I/e}^{(I)} = (\dot{\epsilon} + \dot{\theta})\bar{u}_2 \tag{2.93}$$

Furthermore

$$\begin{aligned}
\bar{\alpha}_{I/e}^{(I)} &= \ddot{\epsilon}\bar{u}_2 + \underbrace{\ddot{\eta}\hat{C}^{I,O}\bar{u}_3}_{0} + \underbrace{\dot{\eta}\dot{\hat{C}}^{I,O}\bar{u}_3}_{0} + \underbrace{\ddot{\phi}\hat{C}^{(I,O)}\hat{C}^{(O,B)}\bar{u}_1}_{0} + \underbrace{\dot{\phi}\dot{\hat{C}}^{(I,O)}\hat{C}^{(O,B)}\bar{u}_1}_{0} \\
&\quad + \underbrace{\dot{\phi}\hat{C}^{(I,O)}\dot{\hat{C}}^{(O,B)}\bar{u}_1}_{0} + \ddot{\theta}\hat{C}^{(I,O)}\underbrace{\hat{C}^{(O,B)}}_{\hat{I}}\underbrace{\hat{C}^{(B,n)}}_{\hat{I}}\bar{u}_2 + \dot{\theta}\dot{\hat{C}}^{(I,O)}\underbrace{\hat{C}^{(O,B)}}_{\hat{I}}\underbrace{\hat{C}^{(B,n)}}_{\hat{I}}\bar{u}_2 \\
&\quad + \underbrace{\dot{\theta}\hat{C}^{(I,O)}\dot{\hat{C}}^{(O,B)}\hat{C}^{(B,n)}\bar{u}_2}_{0} + \underbrace{\dot{\theta}\hat{C}^{(I,O)}\hat{C}^{(O,B)}\dot{\hat{C}}^{(B,n)}\bar{u}_2}_{0} + \underbrace{\ddot{\psi}\hat{C}^{(I,O)}\hat{C}^{(O,B)}\hat{C}^{(B,n)}\hat{C}^{(n,m)}\bar{u}_3}_{0} \\
&\quad + \underbrace{\dot{\psi}\dot{\hat{C}}^{(I,O)}\hat{C}^{(O,B)}\hat{C}^{(B,n)}\hat{C}^{(n,m)}\bar{u}_3}_{0} + \underbrace{\dot{\psi}\hat{C}^{(I,O)}\dot{\hat{C}}^{(O,B)}\hat{C}^{(B,n)}\hat{C}^{(n,m)}\bar{u}_3}_{0} \\
&\quad + \underbrace{\dot{\psi}\hat{C}^{(I,O)}\hat{C}^{(O,B)}\dot{\hat{C}}^{(B,n)}\hat{C}^{(n,m)}\bar{u}_3}_{0} + \underbrace{\dot{\psi}\hat{C}^{(I,O)}\hat{C}^{(O,B)}\hat{C}^{(B,n)}\dot{\hat{C}}^{(n,m)}\bar{u}_3}_{0} \\
&= \ddot{\epsilon}\bar{u}_2 + \ddot{\theta}\hat{C}^{(I,O)}\hat{I}\hat{I}\bar{u}_2 + \dot{\theta}\dot{\hat{C}}^{(I,O)}\hat{I}\hat{I}\bar{u}_2
\end{aligned}$$

where;

$$\hat{C}^{(I,O)} = \begin{bmatrix} \cos(\epsilon) & 0 & -\sin(\epsilon) \\ 0 & 1 & 0 \\ \sin(\epsilon) & 0 & \cos(\epsilon) \end{bmatrix}$$

$$\dot{\hat{C}}^{(I,O)} = \begin{bmatrix} -\sin(\epsilon)\dot{\epsilon} & 0 & -\cos(\epsilon)\dot{\epsilon} \\ 0 & 0 & 0 \\ \cos(\epsilon)\dot{\epsilon} & 0 & -\sin(\epsilon)\dot{\epsilon} \end{bmatrix}$$

Therefore, the angular acceleration term becomes

$$\bar{\alpha}^{(I)}_{I/e} = (\ddot{\epsilon} + \ddot{\theta})\bar{u}_2 \tag{2.94}$$

Substituting all terms into the Euler equation for the inner gimbal gives

$$\begin{bmatrix} J_{I_1} & 0 & 0 \\ 0 & J_{I_2} & 0 \\ 0 & 0 & J_{I_3} \end{bmatrix} \begin{bmatrix} 0 \\ (\ddot{\epsilon} + \ddot{\theta}) \\ 0 \end{bmatrix} + \begin{bmatrix} 0 \\ (\dot{\epsilon} + \dot{\theta}) \\ 0 \end{bmatrix} \times \begin{bmatrix} J_{I_1} & 0 & 0 \\ 0 & J_{I_2} & 0 \\ 0 & 0 & J_{I_3} \end{bmatrix} \begin{bmatrix} 0 \\ (\dot{\epsilon} + \dot{\theta}) \\ 0 \end{bmatrix}$$
$$= \begin{bmatrix} M_{OI_1} \\ T_m + T_{fr} \\ M_{OI_3} \end{bmatrix} + \begin{bmatrix} 0 \\ D_I \\ 0 \end{bmatrix} \tag{2.95}$$

This matrix equation can be decomposed into three scalar equations

$$M_{OI_1} = 0 \tag{2.96}$$

$$M_{OI_3} = 0 \tag{2.97}$$

$$J_{I_2}(\ddot{\epsilon} + \ddot{\theta}) = T_{m_I} + T_{fr_I} + D_I \tag{2.98}$$

The last equation gives the equation of motion for the gimbal inner axis. In Figure 2.6, a simple block diagram of the plant is drawn and some observations about the plant are given.

- Friction function can be selected as one of the many friction models presented in the literature. The model used in this thesis work is the Coulomb friction model which is explained in Section 3.3.3.

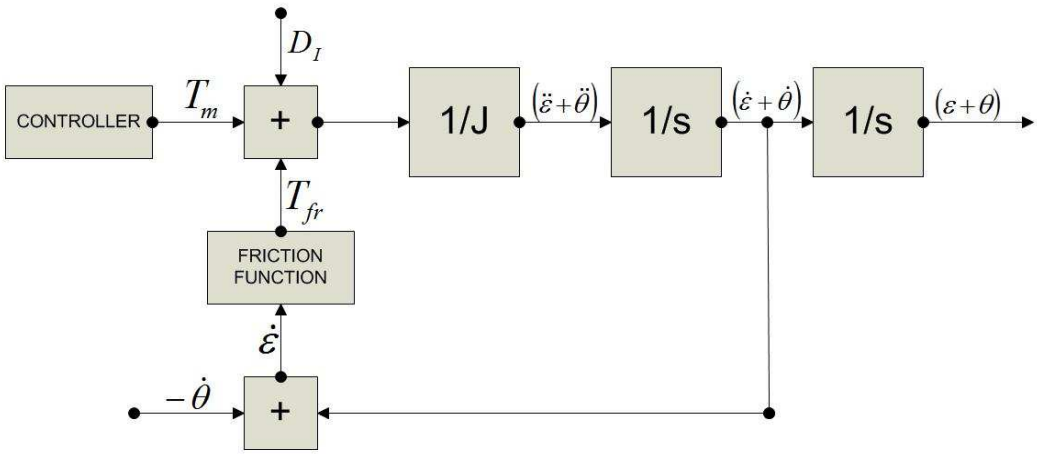

Figure 2.6: Plant Elevation Axis Block Diagram

- $(\dot{\epsilon} + \dot{\theta})$ is the angular velocity of elevation axis relative to inertial frame and it is directly measured by the gyroscopes.

- $(\ddot{\epsilon} + \ddot{\theta})$ is the angular acceleration of elevation axis relative to inertial frame and it is directly measured by accelerometers.

- The effect of base movement $\dot{\theta}$ on the gimbal is through the friction moment developing in the bearing as can be seen from the block diagram. This friction is a function of $\dot{\epsilon}$ which is the relative velocity in this bearing.

2.3 Preliminaries on Kalman Filtering

In this section a brief explanation about Kalman filtering is given since Kalman filters will be used for the fusion and filtering of the velocity and acceleration signals. Reference [21] can be consulted for a detailed derivation and further information.

2.3.1 The Discrete Time Kalman Filter

Kalman filter operates by propagating the mean and covariance of the state through time. Suppose we have a linear discrete-time system given as follows

$$x_k = F_{k-1}x_{k-1} + G_{k-1}u_{k-1} + \omega_{k-1} \tag{2.99}$$

$$y_k = H_k x_k + \upsilon_k \tag{2.100}$$

The noise processes $\{\omega_k\}$ and $\{v_k\}$ are white, zero-mean, uncorrelated and have known covariance matrices Q_k and R_k, respectively

$$\omega_k \approx (0, Q_k)$$

$$\upsilon_k \approx (0, R_k)$$

$$E[\omega_k {\omega_j}^T] = Q_k \delta_{k-j}$$

$$E[\upsilon_k {v_j}^T] = R_k \delta_{k-j}$$

$$E[\upsilon_k {\omega_j}^T] = 0$$

Our goal is to estimate the state x_k based on our knowledge of the system dynamics and the availability of the noisy measurements $\{y_k\}$. The Kalman filter works as follows; assume that we have the expected value and covariance of the state feedback before a certain time k. When time k arrives, before we process the measurement at time k we compute an estimate of x_k (denoted $\hat{x}_k^-$) and the covariance of that estimate (denoted ${P_k}^-$) by using the system model. Then we process the measurement at time k to refine our estimate of x_k. The resulting estimate of x_k is denoted $\hat{x}_k^+$ and its covariance is denoted ${P_k}^+$. The former update using system model is called the time update where the latter is called the measurement update. Figure 2.7 shows the time and measurement updates of the state and covariance estimates.

The so-called time update equations for $\hat{x}$ and P are given as follows. We do not have any additional measurements available to help us update our state estimate between time $(k-1)^+$ and k^-, so we should update the state estimate based on our knowledge of the system dynamics. From the rules for propagation of the mean and covariance of the states, we have

$$\hat{x}_k^- = F_{k-1}x_{k-1}^+ + G_{k-1}u_{k-1} \tag{2.101}$$

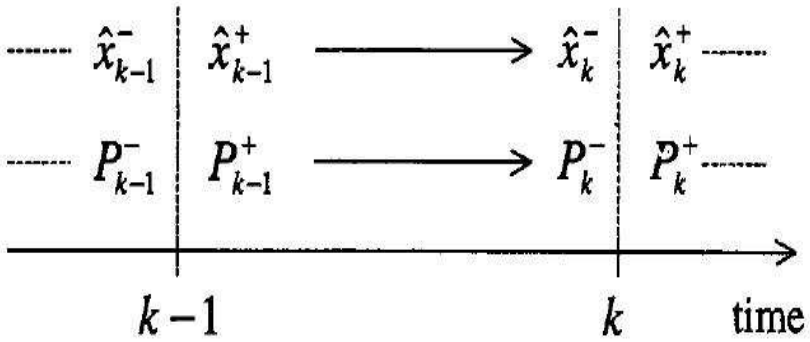

Figure 2.7: Timeline Showing *a priori* and *a posteriori* State Estimates and Estimation Error Covariances [14]

$$P_k{}^- = F_{k-1}P_{k-1}^+F_{k-1}{}^T + Q_{k-1} \tag{2.102}$$

Once the time update equations are given, we continue with the measurement update equations. The derivation of measurement update equations for $\hat{x}$ and P are given in various sources. Here we list the resulting equations as follows

$$\begin{aligned} K_k &= P_k{}^-H_k{}^T(H_kP_k{}^-H_k{}^T + R_k)^{-1}) \\ &= P_k{}^+H_k{}^TP_k{}^{-1} \end{aligned} \tag{2.103}$$

,

$$x_k{}^+ = x_k{}^- + K_k(y_k - H_k\hat{x}_k^-) \tag{2.104}$$

$$\begin{aligned} P_k{}^+ &= (I - K_kH_k)P_k{}^-(I - K_kH_k)^T + K_kR_kK_h{}^T \\ &= [(P_k{}^-)^{-1} + H_k{}^TR_k{}^{-1}H_k]^{-1} \\ &= (I - K_kH_k)P_k{}^- \end{aligned} \tag{2.105}$$

If model and measurement noises, $\{\omega_k\}$ and $\{\upsilon_k\}$ are zero-mean, uncorrelated, white and Gaussian, then the Kalman filter is the optimal solution that minimizes the estimation error. Even, if the noise is not Gaussian, the Kalman filter is still the optimal *linear* filter [14].

2.4 On the Use of Acceleration Information in Servo Control Applications

In this section, the theoretical background will be laid down for the acceleration feedback methods that are going to be utilized. The first subsection will be an introductory section, presenting the expectations and goals in using acceleration feedback together with the definition of a standard base controller without acceleration feedback for comparing the acceleration feedback methods to. Later on, three methods, namely the disturbance observer method, the inner acceleration loop method and the state derivative feedback LQR method, all of which utilize acceleration feedback in controlling the platform will be covered in their corresponding subsections. How control methodologies explained here are implemented in simulation and physical system will be covered in the following chapters.

2.4.1 Definition of the Standard Controller and Overview of Expectations from Using Acceleration Feedback

In stabilization control of a platform, the aim is to minimize the motion of the platform relative to the earth fixed inertial frame in the presence of external disturbance moments and base motion. In most of the stabilized platforms, stabilization is achieved with the help of rate gyros which gives the angular speed of the platform relative to inertial frame and this method can be considered as the state of the art for systems in use today. Feedback from gyros can be considered as the stabilization error in a stabilization task and this error is fed to the controller, which in turn, tries to minimize it. Therefore, one can say that stabilization task is a regulator problem, trying to keep the angular velocity and position states near zero. In Figure 2.8 below, block diagram of a standard controller which uses angular velocity feedback for stabilization is given.

In most of the electromechanical systems, because of the very high bandwidth of the current controller compared to the other loops, combined with the fast dynamics of the servomotor, motor and driver together have little effect in terms of dynamics and delays once they are properly installed and tuned. Therefore this makes it possible for us to model these two elements as a single block, whose transfer function can be identified on the experimental setup. The block representing driver and motor

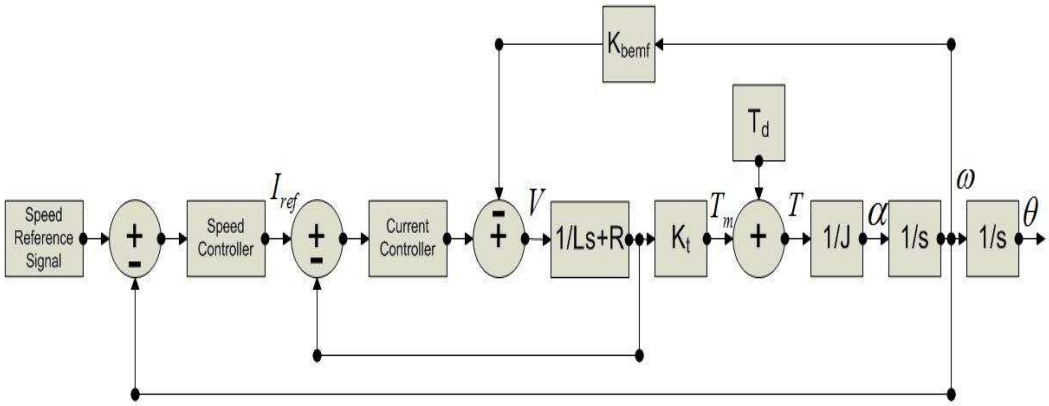

Figure 2.8: Overall System Block Diagram, Plant and Controller Combined.

dynamics will look like as shown in Figure 2.8, with a torque reference signal going into the block and actual torque, which is proportional with the developed current in the motor windings, coming out of the block. For the purpose of controller design, a first order approximation will be sufficient and the transfer function can most of the time be assumed as unity since motor and driver dynamics are very fast compared to the mechanical system dynamics.

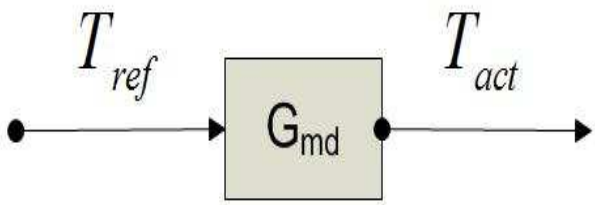

Figure 2.9: Driver and Motor Dynamics Combined in a Single Transfer Function

Therefore with the simplification of Figure 2.9 inserted into the overall system block diagram, we obtain the base system that we are going to work, which is given in Figure 2.10.

In the above figure T_d represents disturbance torques acting on the plant, which includes friction forces, cable restraint forces and external disturbances. Speed con-

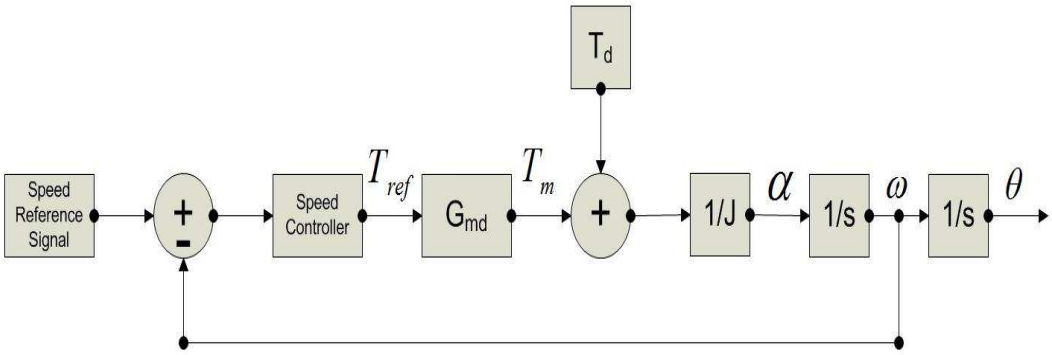

Figure 2.10: Block Diagram After the Motor-Controller Simplification

troller tries to track the reference signal while eliminating the effects of these disturbances. In case of stabilization, this speed reference signal is usually zero and the sole purpose pf the controller becomes rejecting disturbances.

A generic speed controller, which is also the base controller that is going to be a benchmark controller for comparing developed acceleration feedback controllers, is the PII^2 (proportional-integral-double integral) controller [22]. As the name suggests, the controller has proportional and derivative terms and in addition to that, a double integrator. The addition of the second integrator assures that controller can control its position without steady-state error in the presence of a constant disturbance torque. Such constant disturbance torques are commonly encountered in servo control applications, most important examples being the friction torque as a result of the relative motion in a joint or the static gravitational torque which may be caused by the unbalanced mass on the system.

Transfer function of this speed controller is

$$G_{spd} = \frac{K_p s^2 + K_i s + K_v}{s^2} \tag{2.106}$$

After a block diagram simplification is carried out, two important transfer functions can be identified as $\frac{\omega}{\omega_{ref}}$ which can be named as the velocity tracking transfer function and $\frac{T_d}{\theta}$ which can be named as the dynamic stiffness of the system. These transfer

functions are obtained as

$$\frac{\omega}{\omega_{ref}} = \frac{G_{md}(K_p s^2 + K_i s + K_v)}{Js^3 + G_{md}(K_p s^2 + K_i s + K_v)} \tag{2.107}$$

$$\frac{T_d}{\theta} = \frac{Js^3 + G_{md}(K_p s^2 + K_i s + K_v)}{s} \tag{2.108}$$

Our main goal in utilizing acceleration feedback will be to improve the system dynamic stiffness without effecting tracking performance. Therefore the definition of the dynamic stiffness becomes extremely important. In [35] dynamic stiffness is defined to be comprised of both passive and active stiffness. Passive stiffness in systems is based on the plant inertia and damping. Active stiffness is added by the damping and stiffness terms resulting from the feedback controller gains. Cumulatively, they define how big of a disturbance torque is required in order to develop a certain amount of position error; bigger the stiffness meaning better disturbance rejection and smaller position errors.

There is a remarkable number of papers in the literature that promotes the use of acceleration feedback to improve servo performance. It has been shown that acceleration feedback is especially useful in rejecting disturbances. In [23], it is mentioned that in an indirect approach, acceleration signal can be used in an observer to improve the estimates of position and speed i.e., reduce the contamination with noise by filtering the measurements, or raise the bandwidth of the measured signals. This method of improving feedback signal quality will be employed in all controllers designed including the standard controller since a Kalman filter will be used to combine the sensor measurements in all controllers. References [5, 24, 25, 26, 8] make use of a disturbance observer or in other words, a load torque observer in order to compute the load torque using the acceleration measurements and torque developed in the motor. This torque is added to the output of the controller to compensate for the disturbance torques. This method is covered in Section 2.4.2. Finally, in [7, 24, 25, 27, 28] one can find the use of acceleration feedback in a faster inner acceleration loop and this method is covered in Section 2.4.3.

2.4.2 Load Torque Estimator

The basic idea behind the use of a load torque estimator is simple; if we measure the current in the motor armature, we can calculate the torque developed by the motor. In the absence of any disturbance effects such as friction, static and dynamic unbalance or external forces applied on the physical system, the angular acceleration of the controlled inertia can be directly calculated by dividing the motor torque with the total inertia of the system. However, in the presence of these disturbances, there will be a discrepancy between the calculated acceleration and the measured one. Therefore, if the actual acceleration is measured, total disturbance torque can be calculated as

$$T_d = T_m - J\alpha \tag{2.109}$$

where;

T_d: total of disturbance torques

T_m: motor torque

J: total inertia of the system including motor shaft and gearbox inertias

α: angular acceleration of the system

Previous work in this subject [25] showed that a load torque estimator also takes into account the parameter variations in the system such as the variation of total inertia or the variation of motor torque constant. This can be shown by writing the equations of motion and parameter variations as

$$J\alpha = T_m - T_d \tag{2.110}$$

$$T_m = K_t I_a \tag{2.111}$$

$$J = J_n + \Delta J \tag{2.112}$$

$$K_t = K_{tn} + \Delta K_t \tag{2.113}$$

where, J_n and K_{tn} being the nominal inertia and nominal torque constant and ΔJ and ΔK_t being the variations of inertia and torque constant. Substituting Equations 2.111, 2.112, and 2.113 into Equation 2.110, we obtain

$$J_n\alpha = K_{tn} I_a + \tilde{T}_d \tag{2.114}$$

where;

$$\tilde{T}_d = \Delta K_{tn} I_a - \Delta J \alpha - T_d$$

As can be seen, when the nominal values of inertia and torque constant are used, the variation terms can be included in the newly defined disturbance term $\tilde{T}_d$. This aspect is especially useful in our application since inertia variations are commonly encountered in platform stabilization tasks due to the possibility of payload variation.In a double axis gimbal such as the one used, even the angular position change of the elevation axis changes azimuth effective inertia.

Having showed the ability of the load torque estimator to compensate for the variations in the plant, we proceed with below Figure 2.11, in which the addition of a load torque estimator to the base system of Figure 2.10 is shown.

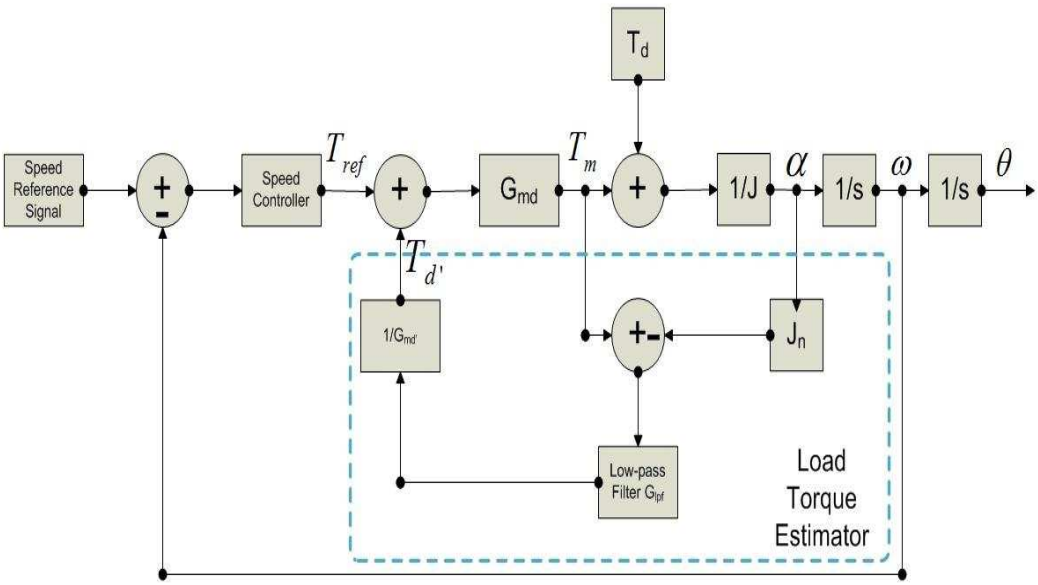

Figure 2.11: Control Structure With Speed Controller and Load Torque Estimator

The low-pass filter placed in the disturbance observer is to account for measurement lag and dynamics of filtering done to get rid of the measurement noise and it has a transfer function which changes with the low-pass filter characteristics such as bandwidth and order. The transfer function G_{md}' is the modeled transfer function of motor and driver dynamics, better modeling of which improves the performance. As one

can see, the performance of the load torque estimator depends on the bandwidth and noise level of the acceleration and actual motor torque signals and also on how good the model of driver-motor pair dynamics, namely G_{md} is. Following analysis shows the effect of the load torque estimator on the disturbance rejection capabilities of the controller better.

By looking at the above block diagram, one can write the estimated load torque $T_d{}'$ as

$$T_d{}' = \frac{1}{G_{md}{}'} G_{lpf} \left(T_m - \frac{\alpha}{J_n} \right) \tag{2.115}$$

Angular acceleration term α can be defined as follows

$$\alpha = \left(\frac{T_m + T_d}{J} \right) \tag{2.116}$$

Substituting Equation 2.116 into 2.115, we obtain

$$T_d{}' = \frac{1}{G_{md}{}'} G_{lpf} \left(\left(1 - \frac{J_n}{J} \right) T_m - \frac{J_n}{J} T_d \right) \tag{2.117}$$

Actual torque exerted on the inertia is the summation of disturbance torque and motor torque, which can be written as

$$\begin{aligned} T &= T_d + G_{md}(T_{ref} + T_d{}') \\ &= T_d + G_{md} T_{ref} + \frac{G_{md}}{G_{md}{}'} G_{lpf} \left(\left(1 - \frac{J_n}{J} \right) T_m - \frac{J_n}{J} T_d \right) \end{aligned} \tag{2.118}$$

Now if we assume that $J_n \cong J$ and $G_{md}{}' \cong G_{md}$, the above expression simplifies to

$$T = G_{md} T_{ref} + T_d (1 - G_{lpf}) \tag{2.119}$$

Equation 2.119 shows that as a result of the load torque compensation, the disturbance torque acts on the system as if through the transfer function $(1 - G_{lpf})$. This is also shown in Figure 2.12. Since G_{lpf} is a low pass filter, load torque compensator will reject disturbances with low frequency content almost completely while disturbances that are higher in frequency content may still pass. As a result, the bandwidth of the load torque estimator becomes an important consideration, justifying the importance of the work done on how to obtain fast and noiseless acceleration signal.

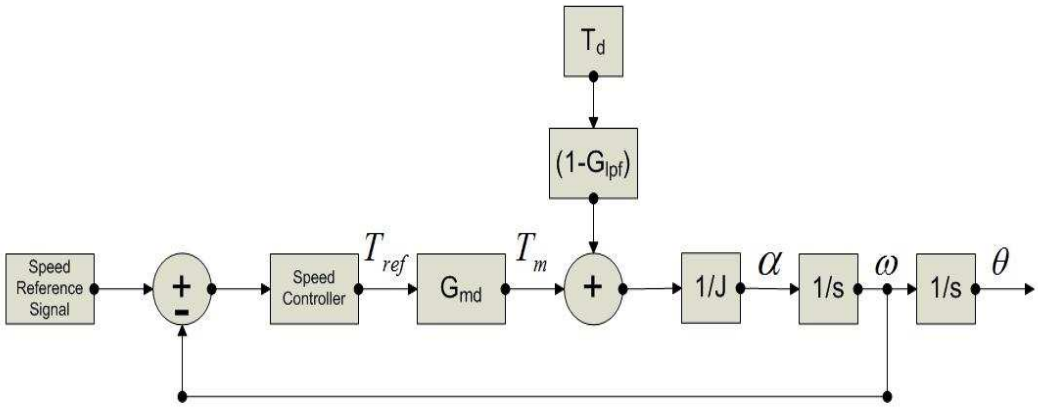

Figure 2.12: Block Diagram Showing the Effective Result of Using a Load Torque Estimator to Compensate Disturbance Torques

A final remark regarding the use of acceleration feedback as shown above is given in [23]. It is stated that an algebraic loop may be introduced due to the direct feed through of the input to the acceleration measurement. However, it is also stated that in practice this concern is of little significance due to the presence of filters and actuator and system dynamics which will surely introduce some time delay, breaking the algebraic loop mentioned.

2.4.3 Inner Acceleration Loop Method

Another approach that can be adopted is the use of acceleration signal as feedback to a fast inner acceleration loop. This approach is also investigated in several works in the literature [7, 24, 25, 27, 28]. The motivation comes from the intuitive idea that a fast inner acceleration loop should be effective in disturbance rejection since the effects of disturbance will be sensed first in acceleration signal before a significant velocity error can build up in the velocity loop. As expected, analysis shows that the effect of acceleration feedback usage in such a loop is a net improvement in the disturbance rejection characteristics. Acceleration feedback acts like an ”‘electronic inertia”’ in addition to the physical inertia of the system, therefore acting as a big flywheel in rejecting disturbances.

It is stated in [7] that, acceleration feedback which acts as an added electronic iner-

tia, allows using higher loop gains without actually increasing the bandwidth of the overall system. Therefore, disturbance rejection performance is increased without increasing the bandwidth of speed and position loops, avoiding undesired oscillatory system response.

Below Figure 2.13 shows the implementation of an inner acceleration loop into the base controller of 2.10. The speed controller shown here is still a PII^2 speed controller but it is different than the previous ones due to having modified gains. The acceleration controller on the other hand is a PI controller.

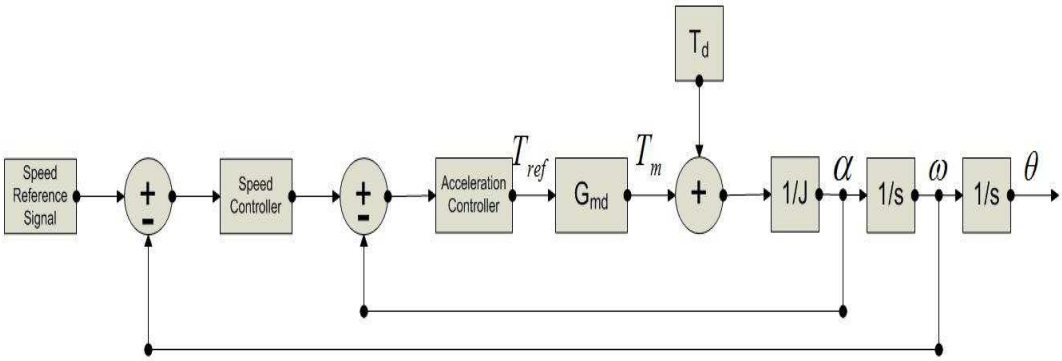

Figure 2.13: Control Structure With Cascaded Speed and Acceleration Loops

Similar to the case of standard controller, transfer functions between velocity reference and actual velocity and between angular displacement and applied disturbance torque as shown below can be obtained

$$\frac{\omega}{\omega_{ref}} = \frac{K_a G_{md}(K_p s^2 + K_i s + K_v)}{s^3(J + K_a G_{md}) + G_{md} K_a (K_p s^2 + K_i s + K_v)} \tag{2.120}$$

$$\frac{T_d}{\theta} = \frac{s^3(J + K_a G_{md}) + G_{md} K_a (K_p s^2 + K_i s + K_v)}{s} \tag{2.121}$$

In the previous sections, $\frac{T_d}{\theta}$ is defined as the dynamic stiffness of the system, which is a measure of disturbance rejection capabilities of the given controller and system. When we compare the newly found dynamic stiffness term Equation 2.121 with the one belonging to the base controller, the addition of $s^3 K_a G_{dm}$ term to the nominator is the most important difference. This result is in line with the previous statement

that acceleration feedback acts like an electronically added inertia. It is evident from Equation 2.121 that higher the acceleration loop gain K_a, the more added electronic inertia and better disturbance rejection. Once again to allow higher acceleration loop gains, the acceleration signal should contain as little noise contamination as possible and have as high a bandwidth as possible.

Note that even though all previous controller gains are multiplied with the factor K_a, the corresponding gains should be identical with the previous case since K_p, K_i, and K_v will no longer be the same as before, they are in fact implicitly divided by K_a.

To have a better understanding of the stiffness expression, let's assume that the transfer function G_{md} is equal to unity and rewrite the terms involved in the expression as follows

$$\frac{T_d}{\theta} = s^2(J + K_a) + sK_aK_p + K_aK_i + \frac{K_aK_v}{s} \tag{2.122}$$

It is evident from Equation 2.122 that four terms involved dominate different frequency ranges. $s^2(J + K_a)$ term is dominant at very high frequencies while $\frac{K_aK_v}{s}$ is dominant at very low frequencies and the remaining two dominate the frequencies in between. Figure 2.14 shows this dependence on frequency. As can be seen in this figure, by introducing the acceleration feedback, rejection against high frequency disturbances, which traditional control schemes struggle the most, is enhanced drastically.

2.4.4 State Derivative Feedback LQR Method

The last of the controllers that are going to be developed, implemented and tested is a controller which can be called as the state derivative feedback LQR. In fact, this control methodology is a modified version of the well-known optimal controller, linear quadratic regulator, modified so that it is applicable to the control problem at hand. Although the 2-DOF gimbal can be modeled as a linear-time invariant system, and a quadratic cost function can be selected as a performance index, making it suitable for the standard LQR solution, the use of acceleration information is not directly possible, making some modification necessary.

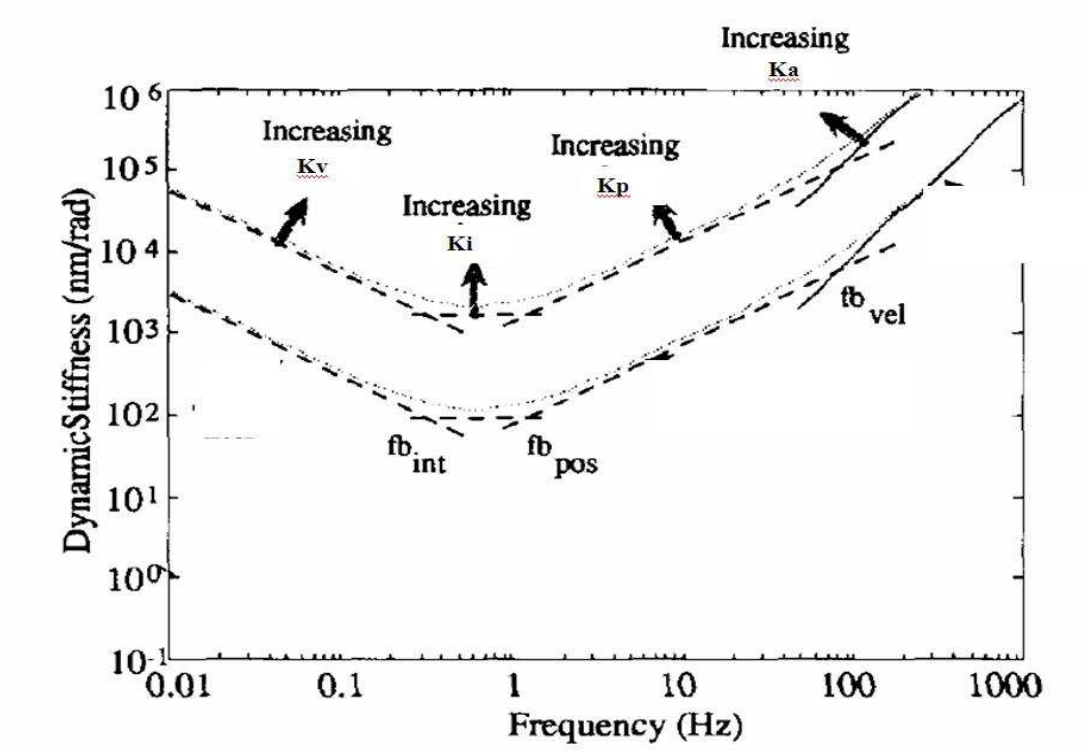

Figure 2.14: Terms Involved in the Dynamic Stiffness Expression and the Effects of Increasing Controller Gains on Dynamic Stiffness [7]

In order to see why standard LQR formulation is not usable for the problem at hand, let's remember the problem definition and solution for the standard LQR [29, 30, 31];

Given the system equation

$$\dot{x} = Ax + Bu \tag{2.123}$$

determine the matrix K of the optimal control vector

$$u(t) = -Kx(t) \tag{2.124}$$

so as to minimize the performance index

$$J = \int_0^\infty (x^T Qx + u^T Ru)dt \tag{2.125}$$

It has been shown that the gimbal axes can be considered as two uncoupled axes that are going to be controlled separately. When system equations are written as shown in Equation 2.123 for both axes, the state vector $\bar{x}$ is a two-dimensional vector containing the angular position and angular velocity terms. When state feedback LQR

method is utilized, angular acceleration cannot be fed back since it is not one of the states. Furthermore, in this formulation the performance index expression given in Equation 2.125 does not contain a cost term for the angular acceleration of the gimbal, whereas we would like to have a cost associated with the angular acceleration. Due to the reasons above, the following modified approach for representing the system equations, which is called the ”‘Reciprocal State Space”’ framework [32, 33] is adopted. A short definition of this framework is given next [34].

$$x = G\dot{x} + Hu \tag{2.126}$$

$$u = L\dot{x} \tag{2.127}$$

where;

$$G = A^{-1} \tag{2.128}$$

$$H = -A^{-1}B \tag{2.129}$$

It is important to note that the eigen values fo the system matrix G in the reciprocal state space are reciprocal of those in the standard state space. Thus, the stability condition for both the reciprocal state space and standard state space frameworks are the same. As shown in Equations 2.126 through 2.129, derivative of the state vector, which has acceleration information, can be directly fed back in the ”‘Reciprocal State Space”’.

The problem definition and solution for the reciprocal state space framework is given next [35].

Given the standard system equation

$$\dot{x} = Ax + Bu \tag{2.130}$$

determine the matrix K of the optimal control vector;

$$u(t) = -K\dot{x}(t) \tag{2.131}$$

so as to minimize the performance index;

$$J = \int_0^\infty (\dot{x}^T Q\dot{x} + u^T Qu)dt \tag{2.132}$$

The solution starts as follows; substituting Equation 2.131 into 2.132, the performance index is rewritten as

$$\begin{aligned} J &= \int_0^\infty (\dot{x}^T Q \dot{x} + \dot{x}^T K^T R K \dot{x}) dt \\ &= \int_0^\infty \dot{x}^T (Q + K^T R K) \dot{x} dt \end{aligned} \tag{2.133}$$

writing x in terms of $\dot{x}$ from Equations 2.130 and 2.131, we have

$$\dot{x} = Ax - BK\dot{x}$$

$$x = A^{-1}(I + BK)\dot{x} \tag{2.134}$$

Now, let there be a P matrix such that

$$\dot{x}^T (Q + K^T R K)\dot{x} = -\frac{d}{dt}(x^T P x) \tag{2.135}$$

where P is a positive definite Hermitian or real symmetric matrix. As a result, we obtain

$$\begin{aligned} \dot{x}^T (Q + K^T R K)\dot{x} &= -\dot{x}^T P x - x^T P \dot{x} \\ &= -\dot{x}^T (P {A_c}^{-1} + {A_c}^{-T} P)\dot{x} \end{aligned} \tag{2.136}$$

where

$$A_c = (I + BK)^{-1} A \tag{2.137}$$

noting that Equation 2.136 must hold true for any x, we require that

$${A_c}^{-T} P + P {A_c}^{-1} = -(Q + K^T R K) \tag{2.138}$$

It can be proven that [31] if A_c is a stable matrix, there exists a positive definite matrix P that satisfies Equation 2.138.

Proceeding with writing the expressions for ${A_c}^{-1}$ and ${A_c}^{-T}$ as follows

$${A_c}^{-1} = A^{-1} + A^{-1} B K$$

$${A_c}^{-T} = A^{-T} + K^T B^T A^{-T}$$

we can rewrite Equation 2.138 as

$$PA^{-1} + A^{-T}P + PA^{-1}BK + K^TB^TA^{-T}P + K^TRK + Q = 0 \tag{2.139}$$

Since R is a positive-definite matrix, one can write $R = T^TT$, where T is nonsingular. Substituting this into the above Equation 2.139, we have

$$PA^{-1} + A^{-T}P + PA^{-1}BK + K^TB^TA^{-T}P + K^TT^TTK + Q = 0 \tag{2.140}$$

which can also be written as

$$PA^{-1} + A^{-T}P + (TK + T^{-T}B^TA^{-T}P)^T(TK + T^{-T}B^TA^{-T}P) - PA^{-1}BR^{-1}B^TA^{-T}P + Q = 0 \tag{2.141}$$

As shown in [31], the minimization of J requires the minimization of

$$\dot{x}^T(TK + T^{-T}B^TA^{-T}P)^T(TK + T^{-T}B^TA^{-T}P)\dot{x} \tag{2.142}$$

with respect to K. Since the last expression is nonnegative, the minimum occurs when it is zero

$$TK = -T^{-T}B^TA^{-T}P \tag{2.143}$$

Finally, the optimal gain matrix K can be found as

$$\begin{aligned} K &= -T^{-1}T^{-T}B^TA^{-T}P \\ &= -R^{-1}B^TA^{-T}P \end{aligned} \tag{2.144}$$

and the optimal control law in this case becomes

$$\begin{aligned} u(t) &= -K\dot{x}(t) \\ &= R^{-1}B^TA^{-T}P\dot{x}(t) \end{aligned} \tag{2.145}$$

The matrix P must satisfy Equation 2.139 or the very well-known algebraic Ricatti equation (ARE)

$$PA^{-1} + A^{-T}P - PA^{-1}BR^{-1}B^TA^{-T}P + Q = 0 \tag{2.146}$$

which can be represented in reciprocal state space framework as

$$PG + G^TP - PHR^{-1}H^TP + Q = 0 \tag{2.147}$$

The above concludes the state derivative feedback solution. However, it does not fully make it possible to use LQR approach in the problem at hand. The last item that needs to be tackled is that full state derivative feedback results in the feedback of angular acceleration and angular velocity and also, the cost function contains terms only containing angular acceleration and angular velocity. However, angular position needs to be included among both the feedbacks and quantities that need to be penalized. In order to satisfy this, the integral of position is also considered as a state and added to the state vector, increasing its size to three, including the integral of angular position, angular position and angular velocity. As a result, state derivative vector also becomes a three dimensional vector containing angular position, angular velocity and angular acceleration, which satisfies our objectives.

CHAPTER 3

MODELING, SIMULATION AND CONTROL USING ACCELERATION FEEDBACK

In order to fully utilize the advantages of additional acceleration measurement in control and stabilization of the 2-DOF gimbal platform, all controller architectures developed in Chapter 2 are implemented and tuned in both simulation and on the experimental setup. This chapter mainly focuses on the implementation and tuning of these controllers. Resulting controllers together with the simulation test results obtained with these controllers are presented in this chapter.

A simulation model of the actual system is built in order to be able to rapidly develop and tune the controllers and also test them without actually running the test setup, therefore avoiding the overhead associated with setting up and calibrating the system and the test equipment each time. Matlab/Simulink is used for both the simulation model and the controller since it is also the environment that is going to be used in real time control of the actual system. SimMechanics blockset, which is a blockset of Simulink especially designed for simulating mechanical systems, is used in the modeling of the 2-DOF gimbal and the 6-DOF motion simulator used in the tests. Controllers are implemented in Simulink and the whole model is run together.

This chapter starts with the identification of dynamic parameters of the actual test setup. In order to simulate the real system as realistically as possible and for controller design purposes, an accurate identification of the system parameters is required. Later, the simulation model built in Simulink and SimMechanics using these parameters is explained in detail. After explanation of the simulation model, controller design efforts are discussed. Firstly, justification of using a Kalman filter in the

controller for fusion and filtering of accelerometer and gyroscope readings is given and tuning of the Kalman filter is done. Following this, implementation and tuning of the different controllers are explained and some properties of the designed controllers are given. This chapter concludes with the explanation and results of the simulation testing of the developed controllers.

3.1 Identification of the Parameters of the 2-DOF Gimbal Platform

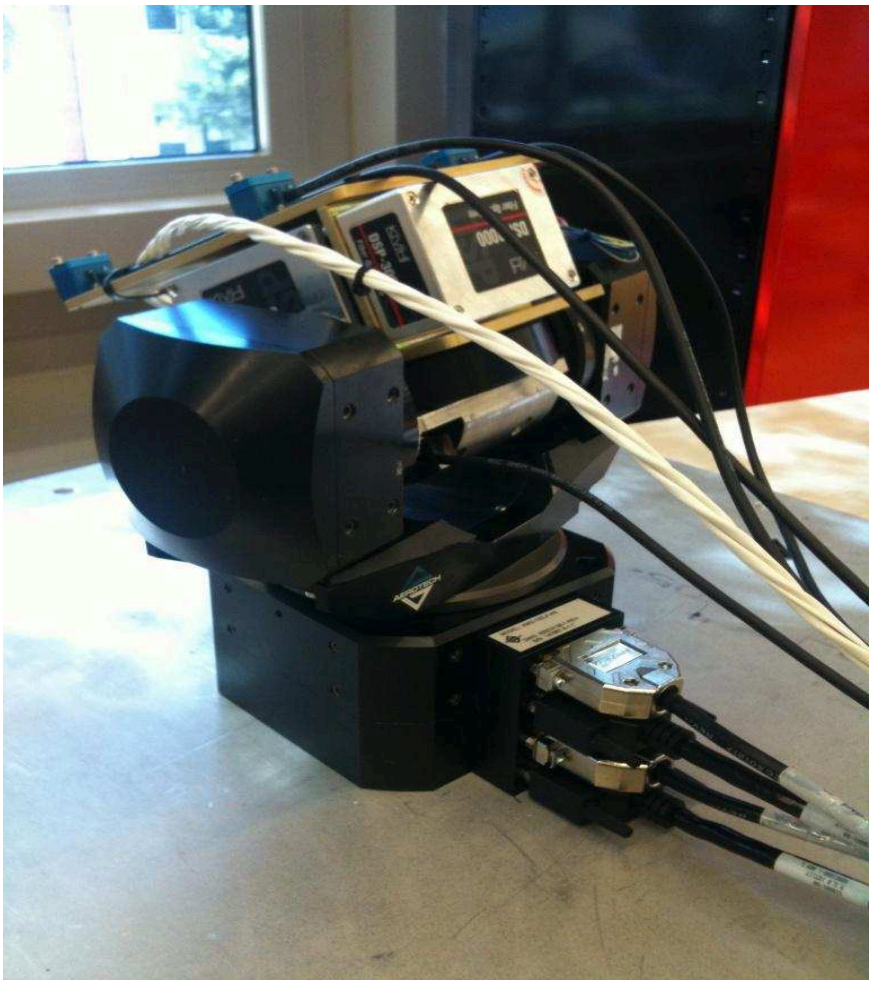

Figure 3.1: Picture of the Gimbal Platform to be Stabilized

In 3.1, a picture of the gimbal platform that is going to be stabilized is given. In order to create a successful simulation model of the system, some important parameters of this gimbal should be accurately identified. These parameters can be listed as the

inertial parameters such as weights, inertias and centers of gravity of azimuth and elevation axes, amount of friction originating from the bearings on the system and most importantly the effect of compliance and accompanying damping effects occurring in the mechanical structure, which effectively constitutes the transfer function of the plant to be controlled. We start with the transfer functions for both azimuth and elevation axes.

3.1.1 Identification of the Azimuth and Elevation Axis Plant Transfer Functions

As discussed in Section 3.3, SimMechanics blockset is used for simulating the mechanical plant which is going to be controlled. Use of SimMechanics blockset makes it necessary to adopt a different identification procedure than the usual one. In this new approach, rather than a transfer function fitting to the system response, a Bode plot of this transfer function is obtained from a frequency response test since transfer functions can not be implemented directly into a SimMechanics model. Later on, the frequency response of the simulation model is made such that it fits to this Bode plot. At the end, a simulation model that simulates the actual plant is obtained. In Section 3.3, use of SimMechanics and the simulation model which is built for system is explained in detail.

Identification of these Bode plots is done with seperate frequency response tests for azimuth and elevation axes. A frequency sweep torque command is given to the mechanical system and the resulting angular acceleration signals are read from the accelerometer array. From these two signals, Bode plot of the transfer function between the torque command given from the real time computer and the angular acceleration signal read from the accelerometers is formed. This transfer function therefore includes the transfer functions of motor drivers and torque loops inside the motor drivers, the motors, the mechanical structure and associated compliance effects and finally any delays in reading the sensor data or dynamics of sensors themselves.

A frequency sweep signal spanning the range from 5Hz to 200Hz is applied as the torque command from the control computer. For low frequencies, the overall transfer function acts as a pure gain therefore there is no need to include frequencies lower

than 5Hz. Frequencies higher than 200Hz on the other hand, are of little importance since control design is done for frequencies well before 200Hz, making frequencies above this upper limit unimportant.

3.1.1.1 Azimuth Axis Plant Bode Plot

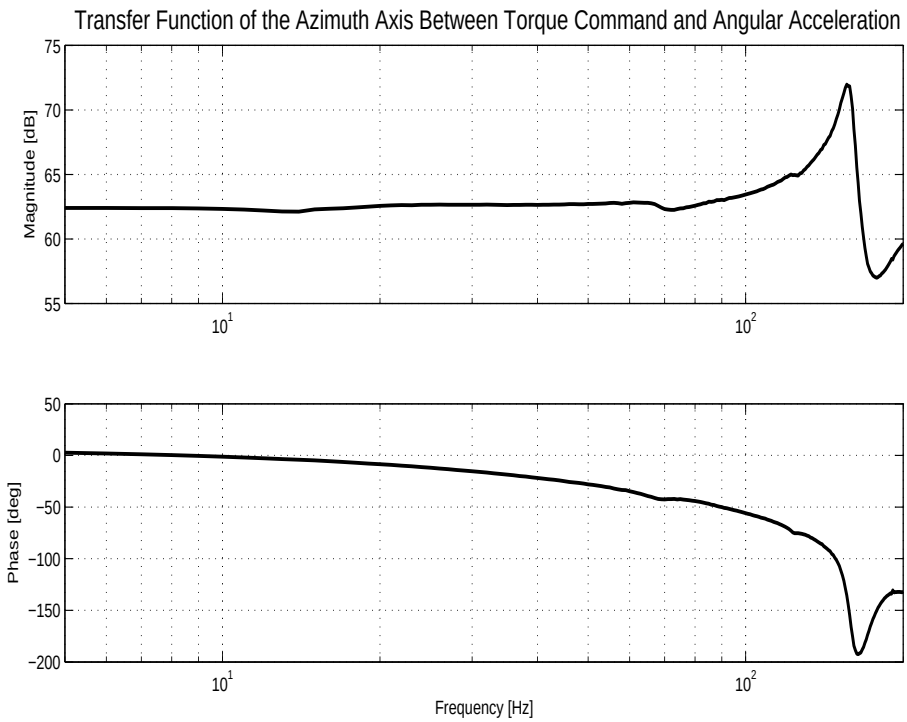

Figure 3.2: Azimuth Axis Plant Bode Plot Between Torque Command and Angular Acceleration

In Figure 3.2 above, Bode plot of the gimbal azimuth axis obtained as a result of the frequency sweep test is given. It is evident from the plot that the mechanical structure remains rigid until very high frequency excitations and the first structural dynamic observed is the resonance at frequencies near 160Hz. Monotonically increasing phase loss with increasing frequencies is easily spotted in the phase plot, which is considered to be mainly due to delays occurring in sensor measurement.

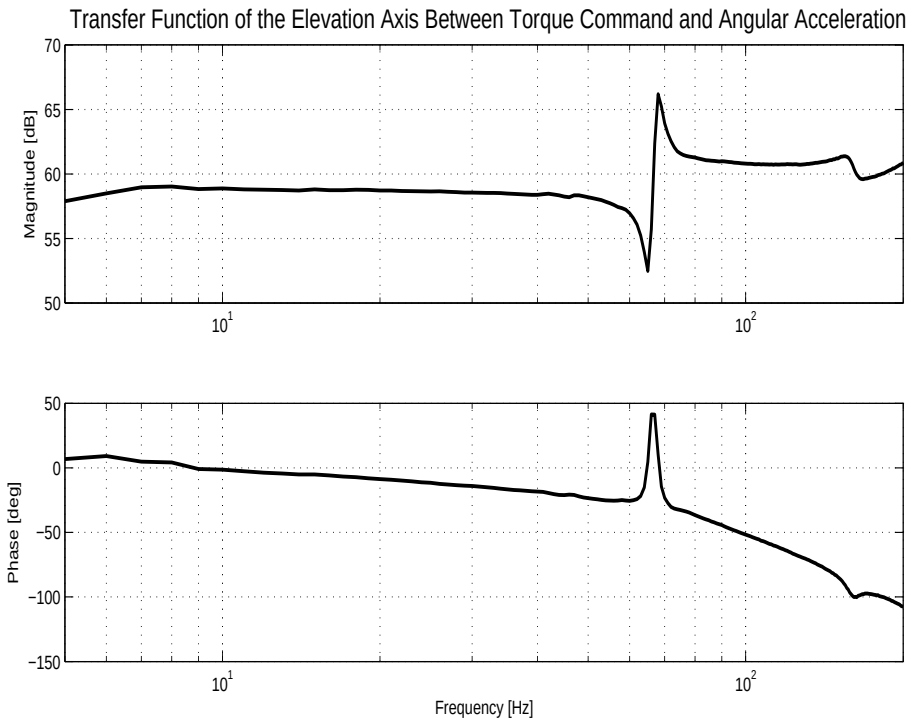

Figure 3.3: Elevation Axis Plant Bode Plot Between Torque Command and Angular Acceleration

3.1.1.2 Elevation Axis Plant Bode Plot

In Figure 3.3 above, Bode plot of the gimbal elevation axis obtained as a result of the frequency response test is given. It is seen that the mechanical structure remains rigid until considerably high frequencies, only a small-magnitude perturbation is seen near 65Hz. Monotonically increasing phase loss with increasing frequencies is easily spotted in the phase plot, which is considered to be mainly due to delays occurring in sensor measurement.

3.1.2 Identification of the Azimuth and Elevation Axis Inertial Parameters

Inertial parameters that are going to be identified include masses, inertias and centers of gravity of both axes. CAD models of the parts, catalog properties and Bode plots given in Figures 3.2 and 3.3 are used in order to identify these parameters.

3.1.2.1 Azimuth Axis Inertial Parameters

First of these parameters is the mass of azimuth axis. In calculating the mass, we take into account all the parts that azimuth axis motor can move but elevation motor cannot move. This approach is dictated by the way inertial properties of mechanical elements are defined in SimMechanics. When masses of the used components and materials of designed parts are entered into the computer aided drawing model of the system, total mass is calculated to be around 4 kilograms. Using the same method, inertia tensor of the azimuth axis around its COG is calculated to be equal to $[33166\ 94\ 22; 94\ 10463\ 106; 22\ 106\ 29582]10^{-6}\ kgm^2$. Finally, the location of the center of gravity is calculated to be 59 mm above the center of azimuth bearing, coincident with the center of rotation in the remaining two directions.

3.1.2.2 Elevation Axis Inertial Parameters

First of these parameters is the mass of elevation axis. In calculating the mass, we take into account all the parts that elevation axis motor can move. This approach is dictated by the way inertial properties of mechanical elements are defined in SimMechanics. When masses of the used components and materials of designed parts are entered into the computer aided drawing model of the system, this value is calculated to be around 3.4 kilograms. Using the same method, inertia tensor of the azimuth axis around its COG is calculated to be equal to $[8708\ 19\ -246; 19\ 7122\ 727; 246\ 727\ 8195]10^{-6}$ kgm^2. Finally, the location of the center of gravity is calculated to be 4 mm above the intersection of centers of rotations of the two gimbal axes.

3.1.2.3 Correction of Inertia Values Using Information Obtained from Bode Plots

Even though CAD models give quite accurate inertia values for both axes, there exists some discrepancy between the real values and the ones obtained from the CAD model due to modeling errors and insufficient information about some components' masses and inertias. These discrepancies however, can be corrected using the information one can get from the Bode diagrams of the axes. Note that the low frequency parts

of the Bode plots for both axes can be characterized as a pure gain, with constant magnitude and zero phase. This gain is the overall gain of the system from the torque command to the resulting angular acceleration. Once we know the amount of torque developed by the electric motors for an input torque command, we can calculate the inertia of that axis using Newton's law.

It is important to note that, the torque command signals which is used in drawing the Bode diagrams of both axes are both normalized to 10, which means that 10 corresponds to the maximum torque in one direction, and -10 corresponds to the maximum torque in the other direction while 0 means no torque output. For the azimuth axis, peak torque output of the motor is 9.3 Nm while this value is 1.82 Nm for the elevation axis.

Looking at low frequency part of the azimuth axis Bode plot, a gain of 62.5 dB, which is equal to 1334, is read from torque command to the measured angular acceleration. Taking into account the known driver-motor combined gain of 0.93 and radian to degree conversion gain of 57.296, one can find the inertia of the azimuth axis as $0.93 * 57.296/1334 = 0.04\ kgm^2$. However, note that this value is the combined value of both azimuth and elevation axes. When the corresponding J_{zz} elements of the above two inertia tensors are summed, a value of 0.0378 kgm^2 is obtained, resulting in a difference of 0.0022 kgm^2, which is added to the simulation model as a correction.

Repeating the same for elevation axis Bode plot, a gain of 59 dB, which is equal to 891, is read from torque command to the measured angular acceleration. Taking into account the known driver-motor combined gain of 0.182 and radian to degree conversion gain of 57.296, one can find the inertia of the azimuth axis as $0.182 * 57.296/891 = 0.0117\ kgm^2$. When the corresponding J_{yy} element of the elevation inertia tensor is checked, a value of 0.0071 kgm^2 is obtained, resulting in a difference of 0.0046 kgm^2, which is added to the simulation model as a correction.

3.1.3 Identification of Azimuth and Elevation Axis Friction Torques

One of the most important parameters for a stabilized platform is the amount of friction force developing in bearings, gears and gearboxes for the reason that this torque

acts as a disturbance torque in the presence of base platform movements. Since direct-drive motors together with low-friction bearings are used in the 2-DOF platform, no gear and gearbox friction and a very low amount of bearing friction is present in the system. As explained in Section 3.3.3, the friction existing in the bearings is assumed to be fitting to the Coulomb friction model. Therefore, the measurement of this friction torque can be done as follows; the axis whose friction is measured is rotated with a constant angular velocity of 2 deg/s in both directions, covering the full operational range of the axis. While this is done, the amount of torque developed by the motors is logged. In the absence of acceleration and deceleration torques, the measured torque is assumed to be mainly due to the friction in the associated bearings. Later, friction torque values as a function of gimbal position is plotted. In the following subsections, friction torques for azimuth and elevation axes obtained using this method are given.

3.1.3.1 Azimuth Axis Friction Torque

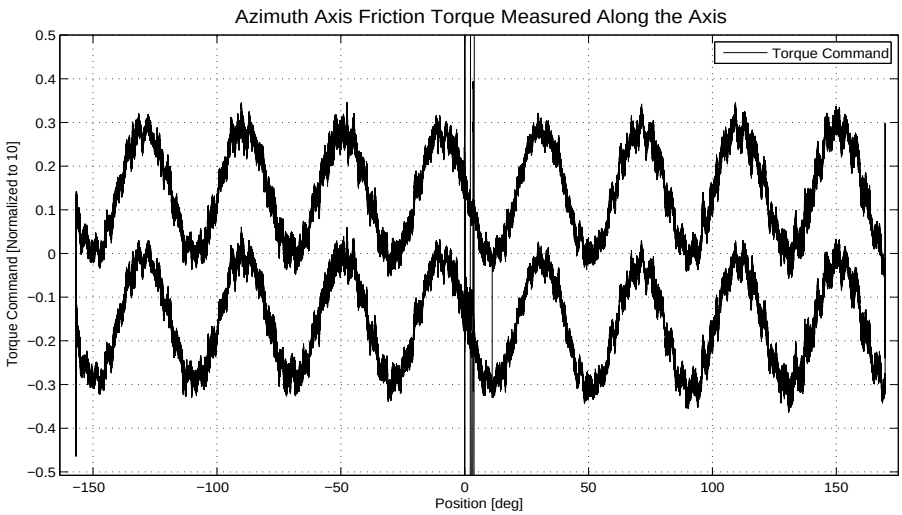

Figure 3.4: Azimuth Axis Friction Torque Plot

In Figure 3.4, friction torque values measured for the azimuth axis is given. While two constant torque lines are expected, the result is not in agreement with the expectations. Two fluctuating lines are present in the figure. The fluctuation on the torque signal is considered to be due to the cogging torque developed in the motor itself. From the

offset between these two lines, the amount of friction can be calculated. Taking into account that this offset corresponds to two times the friction torque in one direction and assuming the same amount of friction acts in both directions it is seen that the offset is 3% of the maximum motor torque, and the friction torque is found to be equal to $9.3 \times \frac{3}{2\times100} = 0.140\ Nm$. Note that, although variations exist between different friction models, it will be assumed that this friction is both the break-away friction and the kinetic friction.

3.1.3.2 Elevation Axis Friction Torque

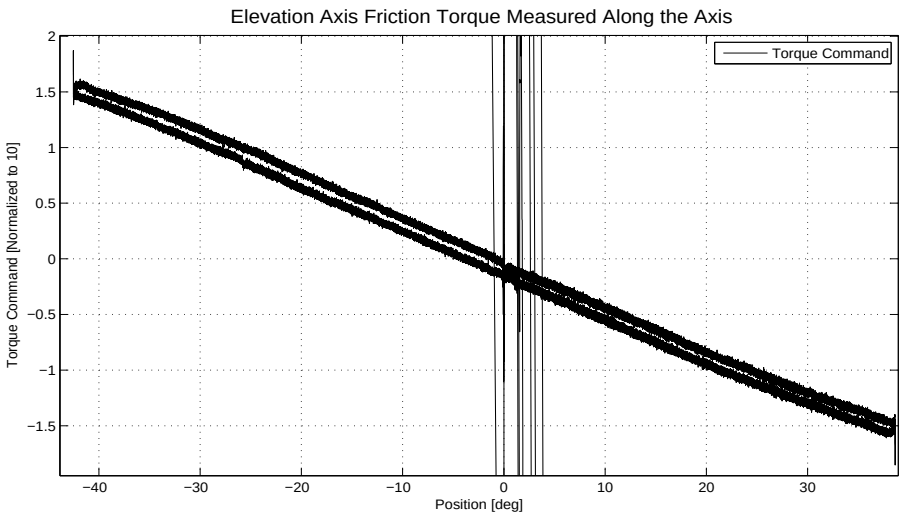

Figure 3.5: Elevation Axis Friction Torque Plot

In Figure 3.5, torque values measured as described in the previous section for the elevation axis is given. Two almost linearly changing torque lines are present in the figure. This almost-linear trend superposed onto the torque signal is due to the unbalance torque resulting from the distance between center of rotation and COG of the elevation axis. From the offset between these two lines, the amount of friction can be calculated. Taking into account that this offset corresponds to two times the friction torque in one direction and assuming the same amount of friction acts in both directions it is seen that the offset is 1.2% of the maximum motor torque, therefore obtaining the friction torque to be equal to $1.82 \times \frac{1.2}{2\times100} = 0.011\ Nm$. Note that,

although variations exist between different friction models, it will be assumed that this friction is both the break-away friction and the kinetic friction.

3.1.4 Identification of ”‘Friction to System Inertia Ratio”’ as an Important Parameter for Stabilized Platforms

As mentioned previously, friction proves to be one of the most important sources of disturbance in stabilized systems. Other disturbances such as the one due to unbalanced mass or forces acting on the stabilized platform may not be present in a given system as a result of good mechanical design or working scenario of the gimbal, respectively. However, no matter what size the platform is, or how good it is designed or manufactured, there always is some friction torque acting as disturbance on the platform. Furthermore, disturbance due to friction torque is unpredictable since it is caused by the relative motion of the gimbal axes, which in turn is caused by the unpredictable disturbances of the gimbal base.

As stated earlier, stabilization performance is measured in terms of the amount of positional perturbation of the platform from its intended position. Due to Newton’s law, the amount of perturbation the plant undergoes as a result of certain disturbance is inversely proportional with the total inertia of the plant. This is logical since bigger and heavier systems will be effected less from the same disturbance torque while smaller systems will be effected more. Therefore, the ratio of disturbance and system inertia can be recognized as a good sign of how well the system can be stabilized.

Discussion of the last two paragraphs leads to the definition of a commonly used design performance index for stabilized platforms, namely the ”‘Friction to System Inertia Ratio.”’ For achieving a high performance platform with low stabilization accuracy, this ratio must be kept as low as possible. As a rule of thumb, it is stated that a ratio of two or less should be aimed for good performance.

For the 2-DOF gimbal we use, this ratio can be calculated for the azimuth and elevation axes separately. Azimuth axis friction torque is calculated to be 0.14 Nm in the previous chapter while total inertia of azimuth axis is 0.04 kgm^2. This results in a ratio of 3.5, which is a little high. On the other hand, elevation axis friction torque

is calculated to be 0.011 Nm while the total inertia is 0.0117 kgm^2. Friction torque to inertia ratio is just under one for the elevation axis, which is much better than azimuth axis ratio.

Looking at the obtained ratios for azimuth and elevation axes, it can be predicted that stabilization performance of elevation axis should be better due to its lower friction torque to inertia ratio, assuming all other factors are taken to be similar and only friction disturbance is acting on the system. Indeed, this result will be achieved as a result of the simulation model runs later in this chapter.

3.2 Sensor Fusion and Filtering

The addition of angular acceleration measurement to the already measured angular velocity signal and its effects on improving the stabilization performance is the main topic analyzed throughout this thesis work. Even though an improvement is expected as the result, one may also consider this additional measurement as a redundant one since acceleration information can be obtained by taking the derivative of velocity. Therefore, this section will focus on showing that measurement of acceleration in fact improves the quality of velocity and acceleration signals to a degree that the techniques utilizing acceleration feedback are realizable. In this section properties of sample signals collected from the sensors are analyzed and optimality conditions for a Kalman filter are checked. Finally, the quality of velocity and acceleration signals obtainable with and without the additional acceleration measurement are assessed, showing the improvement possible with additional acceleration measurement.

3.2.1 Identification of the Amount of Sensor Noise for Sensors Used

Presented in Figure 3.6 is the sample data collected from sensors mounted on the system while the system is not moving. A 20-second acceleration measurement is given on the top graph, while velocity measurement belonging to the same time period is given in the bottom graph. While peak-to-peak noise levels can be read from the graphs, covariances of these noise signals are calculated to be 58.25 for angular acceleration signal and 0.0054 for angular velocity signal.

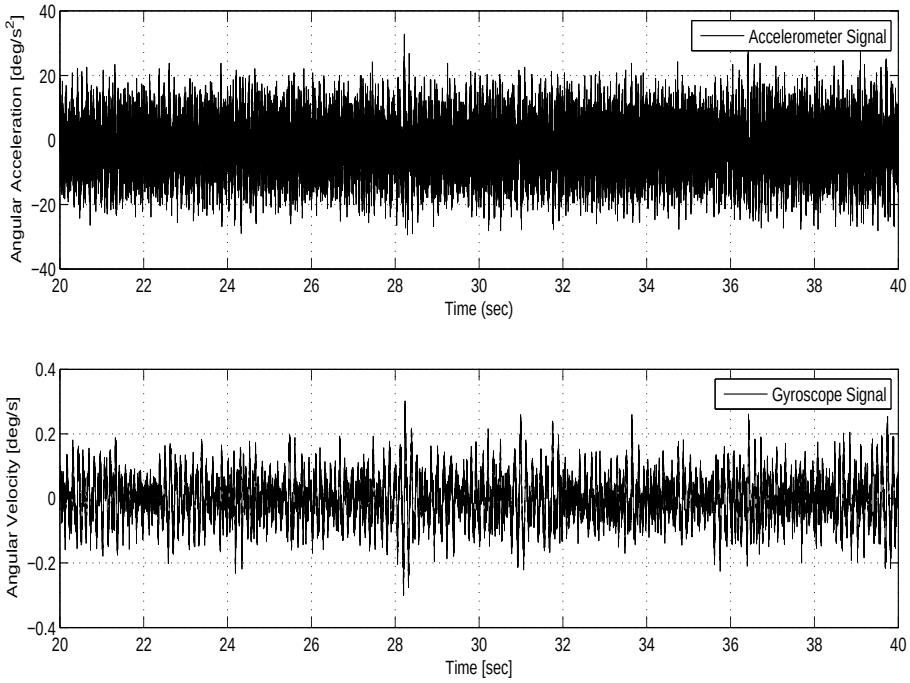

Figure 3.6: Sample Accelerometer Array and Gyroscope Noises Collected from the System in the Absence of any Motion

Using these covariance values, actual sensor noises are simulated in the simulation model by adding white noise with same covariances to the corresponding measurement signals. White noise assumption made here is discussed in more detail in later chapters and found to be valid. Figure 3.7 shows the artificial noise added. Note that peak-to-peak noise amplitudes of both acceleration and velocity signal noises are very similar to the collected signal. Some differences in the characteristics are inevitable but this similarity shows the validity of the white noise assumption.

3.2.2 Analysis of Validity Conditions for Kalman Filter Optimality

The noise in sensor measurements must be attenuated to some permissible degree so that they can be used as feedback signals; otherwise noise amplification in the controller may cause high frequency vibrations. Several approaches can be used in order to filter out the undesired noise present in the measurements, the most popular of these being the use of FIR or IIR low-pass filters to reduce the high frequency noise

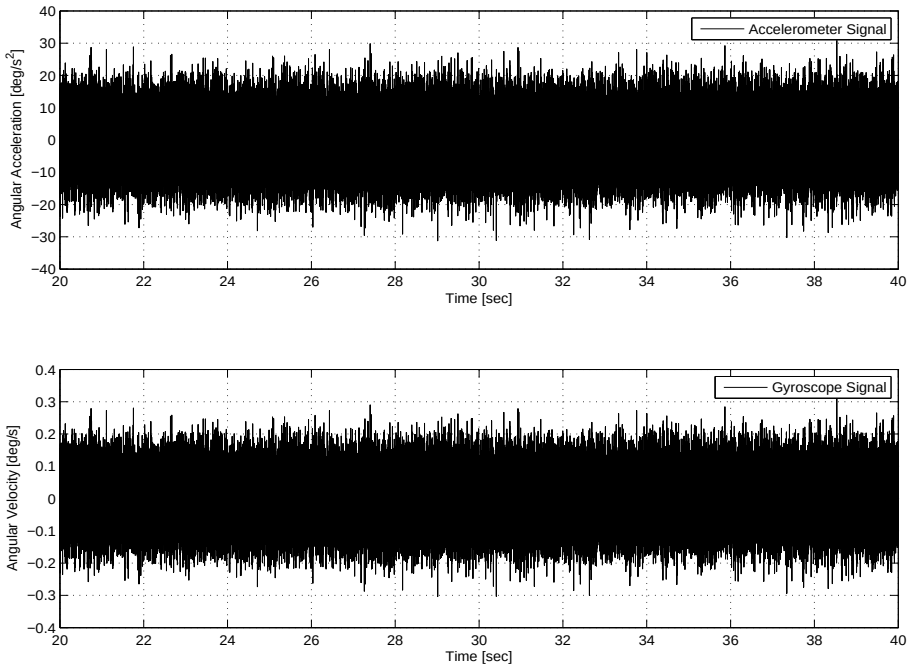

Figure 3.7: Artificially Created Accelerometer Array and Gyroscope Noises to be Used in the Simulation Model

while keeping the low frequency sensor information unaltered. Note that separate filters must be used for both velocity and acceleration signals. Orders and cutoff frequencies of the filters are highly important parameters since filters will introduce delays into the feedback signals even in the pass-band frequencies and these delays will effect the loop performances directly.

A second and yet better approach will be the use of a Kalman filter, one for each axis, combining both angular velocity and angular acceleration signals in a single Kalman filter and calculating both filtered velocity and acceleration signals together. As a widely known fact, the Kalman filter is the optimal filter once certain conditions are satisfied. Therefore it will be shown that these conditions are satisfied, making the use of a Kalman filter the optimal method. Once this is done, tuning and performance assessment of the used Kalman filters is given in the next section.

According to [21], for the Kalman filter to be the optimal filter certain conditions must hold. These conditions can be listed as follows;

- The modeling noise ω_k and the measurement noise v_k must be uncorrelated stochastic processes.
- The modeling noise ω_k and the measurement noise v_k must be zero mean.
- The modeling noise ω_k and the measurement noise v_k must be white.
- The modeling noise ω_k and the measurement noise v_k must be Gaussian.

Now we will check the validity of these conditions one-by-one.

On modeling noise $\omega_\mathbf{k}$ and measurement noise $\mathbf{v_k}$ being uncorrelated: Being uncorrelated implies that the occurrence of one event has no effect on the probability of the occurrence of the other event. We know that both noise processes defined in the system model, ω_k and v_k are stochastic processes. From the two, v_k models the noise present in the sensor measurements whereas ω_k is an artificially included noise term which tries to model the errors present in the system dynamic model. Therefore it is evident that there can be no correlation in between these two stochastic processes and it is concluded that this condition holds.

On modeling noise $\omega_\mathbf{k}$ and measurement noise $\mathbf{v_k}$ being zero-mean: As stated in the previous item, since ω_k is an artificially defined noise term, we can easily define it to be zero-mean. v_k on the other hand is a real signal which may have offsets and other non-zero mean noise components originating from sensors. However, these non-zero mean noise components are cancelled out at the start of every operation of the system in a drift-compensation process by calculating the average of these offsets over an adequate amount of time and subtracting it from the signals. Therefore, it is concluded that both noise terms are zero-mean.

On modeling noise $\omega_\mathbf{k}$ and measurement noise $\mathbf{v_k}$ being white: The definition of discrete time white noise implies that it does not have any correlation with itself except at the present time. This shows that the power of a discrete-time white noise process is equal at all frequencies. Therefore we will analyze the power density spectrum of both angular velocity and angular acceleration signals to see if the signals are white or colored. Once again note that since ω_k is an artificially defined noise term, we can easily define it to be white. For v_k, we will check the power spectral density of

noise components in both gyroscope and acceleration sensor readings from respective periodograms.

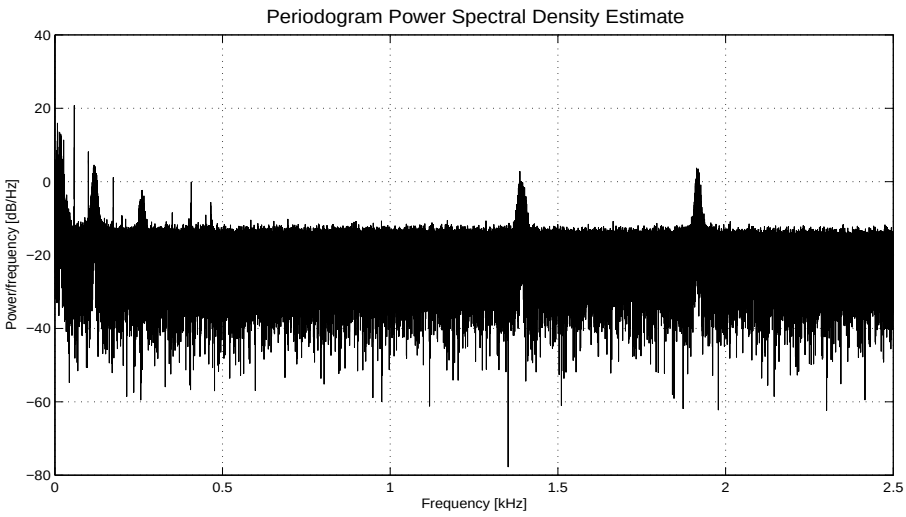

Figure 3.8: Power Density Spectrum Computed for Angular Acceleration Signal Collected for y-axis of the Gimbal

In Figure 3.8, periodogram of a sample angular acceleration signal belonging to gimbal y-axis is given. The sensor readings are recorded while the gimbal is not moving and disturbances acting on the gimbal platform from outside sources are tried to be minimized. One can see that excluding a couple of frequencies in which the power density rises over the average value, the power spectrum density remains flat. These few high energy frequencies are most likely results of external disturbances and noise from sources in the close environment. Hence, it is concluded that noise read from accelerometers are white.

In Figure 3.9, periodogram of the gyroscope y-axis reading is given for the same time period. While the plot is not perfectly flat, one can say that power densities among different frequencies does not change drastically hence it is concluded that white noise assumption for the noise read from the gyroscopes is also valid.

On modeling noise ω_k and measurement noise v_k being Gaussian: In the previous items it is shown that both ω_k and v_k are zero-mean noises and here it will be shown that these two stochastic processes have Gaussian distribution around the mean point. Once again note that since ω_k is an artificially defined noise term, we can easily

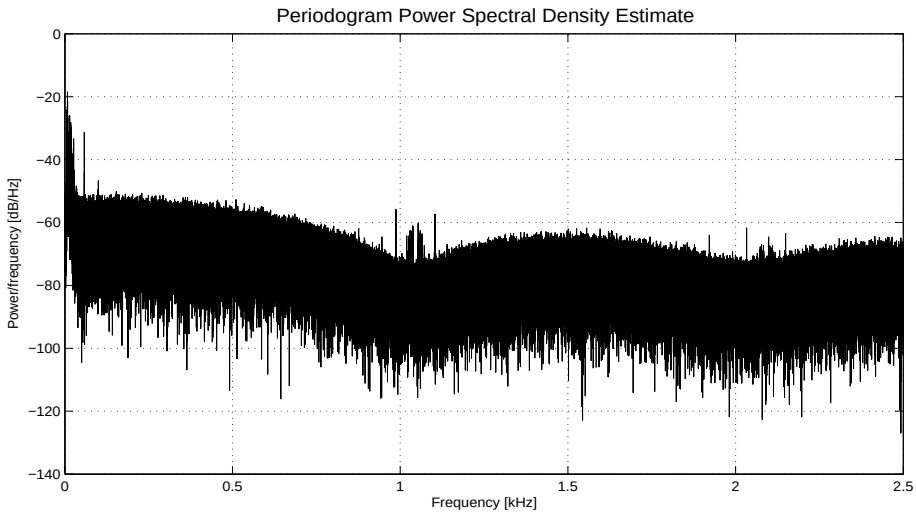

Figure 3.9: Power Density Spectrum Computed for Angular Velocity Signal Collected for y-axis of the Gimbal

define it to have Gaussian distribution. The distribution of v_k on the other hand will be obtained by looking at the histograms of accelerometer array and gyroscope readings.

In Figures 3.10 and 3.11 that follows, histograms of the signals collected from gyroscope and accelerometer array in y-direction is given respectively for the same experiment of previous item. The distribution functions of both noises clearly resemble a Gaussian distribution. Hence it is concluded that both modeling noise and measurement noise terms are Gaussian.

3.2.3 Implementation and Tuning of the Kalman Filter Used

The Kalman filter which is going to be implemented into the controller uses the following kinematic system model;

$$x_k = \begin{bmatrix} \theta_k \\ \omega_k \\ \alpha_k \\ \gamma_k \end{bmatrix} = \begin{bmatrix} 1 & t_s & \frac{{t_s}^2}{2} & \frac{{t_s}^3}{6} \\ 0 & 1 & t_s & \frac{{t_s}^2}{2} \\ 0 & 0 & 1 & t_s \\ 0 & 0 & 0 & 1 \end{bmatrix} \begin{bmatrix} \theta_{k-1} \\ \omega_{k-1} \\ \alpha_{k-1} \\ \gamma_{k-1} \end{bmatrix} + \omega_{k-1} \tag{3.1}$$

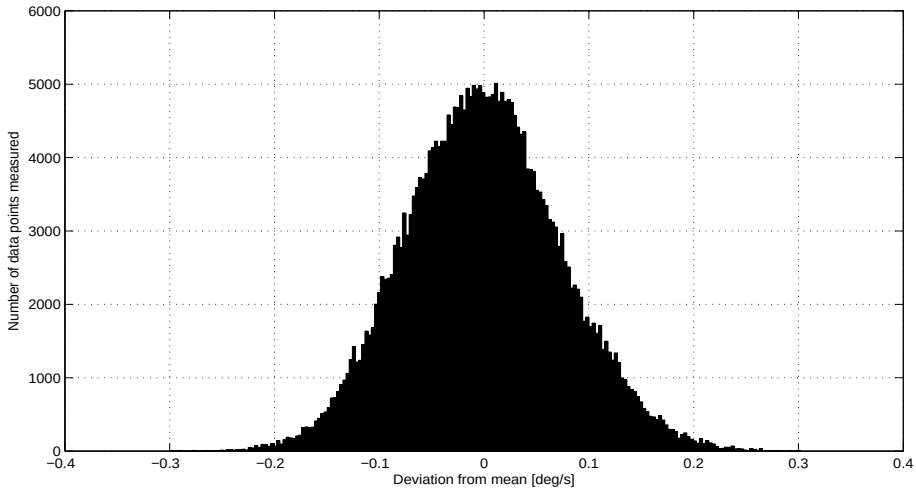

Figure 3.10: Histogram of the Sample Angular Velocity Measurement for y-axis

$$y_k = \begin{bmatrix} \omega_k \\ \alpha_k \end{bmatrix} = \begin{bmatrix} 0 & 1 & 0 & 0 \\ 0 & 0 & 1 & 0 \end{bmatrix} \begin{bmatrix} \theta_k \\ \omega_k \\ \alpha_k \\ \gamma_k \end{bmatrix} + v_k \tag{3.2}$$

As can be seen from Equation 3.1, a constant jerk kinematic model is used for Kalman filter time update equations. The reason for this is the fact that inputs of the system cannot be modeled adequately enough for the use of the real dynamic model of the system. More precisely, although we can know the generated motor torque, disturbances are still unpredictable and therefore cannot be included in the model. This results in a degradation in filter performance rather than an improvement. As an example of this behaviour take the case in which a constant external disturbance torque is being applied to the system. The controller, if working properly, is going to apply an opposite torque trying to reject this disturbance and keep the platform stabilized. After letting enough time for the transients to die, the net torque acting on the plant, which is the sum of disturbance and controller output torques should be around zero and no acceleration of the system should be observed if stabilization is successful. However, since it is possible only to measure motor torque, the only available input to a dynamic system model will be the misleading motor torque and if fed into the

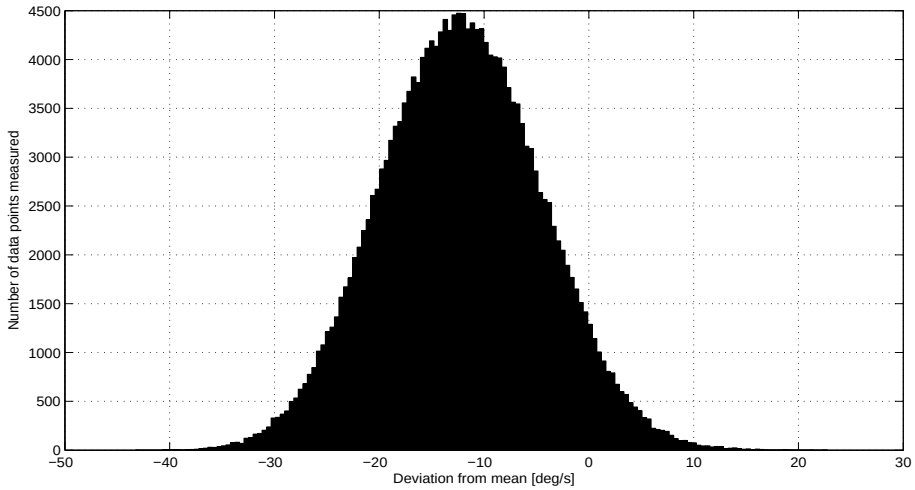

Figure 3.11: Histogram of the Sample Angular Acceleration Measurement for y-axis

model, this input will try to accelerate the modeled system while we know that the real system is not accelerating. As a result, the state estimations and filter outputs will be degraded.

The modeling noise matrix and the measurement noise vector are left to be determined once the Kalman filter model is determined as above. These parameters can be considered as the tuning parameters of the filter. Measurement noise vector is a two-element vector consisting of the velocity measurement covariance and the acceleration measurement covariance. Modeling noise matrix on the other hand is a four-by four matrix, designed to have all zero elements except the last diagonal one and the last diagonal element equal to the modeling noise covariance. This approach takes into account the modeling error done with the constant jerk assumption by adding an error term to the new constant jerk estimate at each step.

As a result three parameters are there for tuning the Kalman filter, which can be listed as follows;

- **Modeling noise covariance:** which defines the amount of error present in the system model,
- **Velocity measurement noise covariance:** which defines the amount of noise

in the velocity measurement done with the gyroscopes,

- **Acceleration measurement noise covariance:** which defines the amount of noise in the acceleration measurement done with the accelerometer array.

Of the above three parameters, velocity measurement noise covariance and the acceleration measurement noise covariance are already known values, obtained in the previous subsection from sample gyroscope and accelerometer noise readings as 0.0054 and 58.25, respectively. Therefore, this gives us the true relative covariance ratio of the two noise signals. In addition, knowing these two covariance terms makes it possible to fix two of the three filter parameters and tune the remaining one as a more straightforward and easier process.

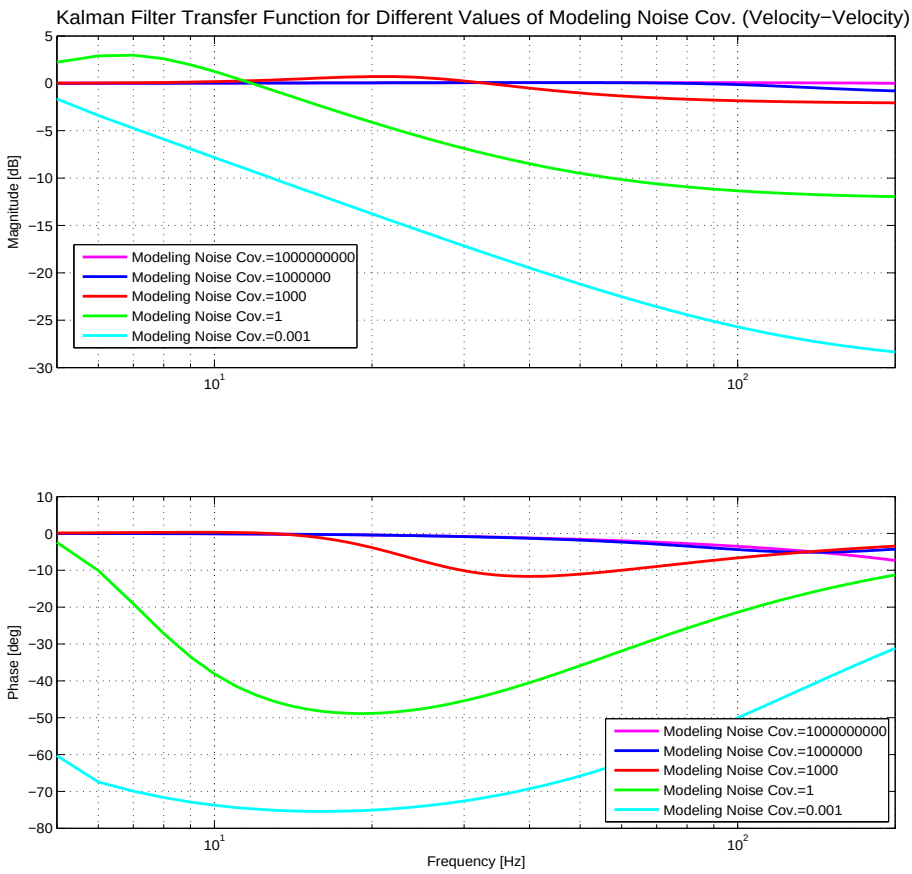

Figure 3.12: Variation of the Kalman Filter Transfer Function Between Input Velocity and Output Velocity for Different Values of the Modeling Noise Covariance

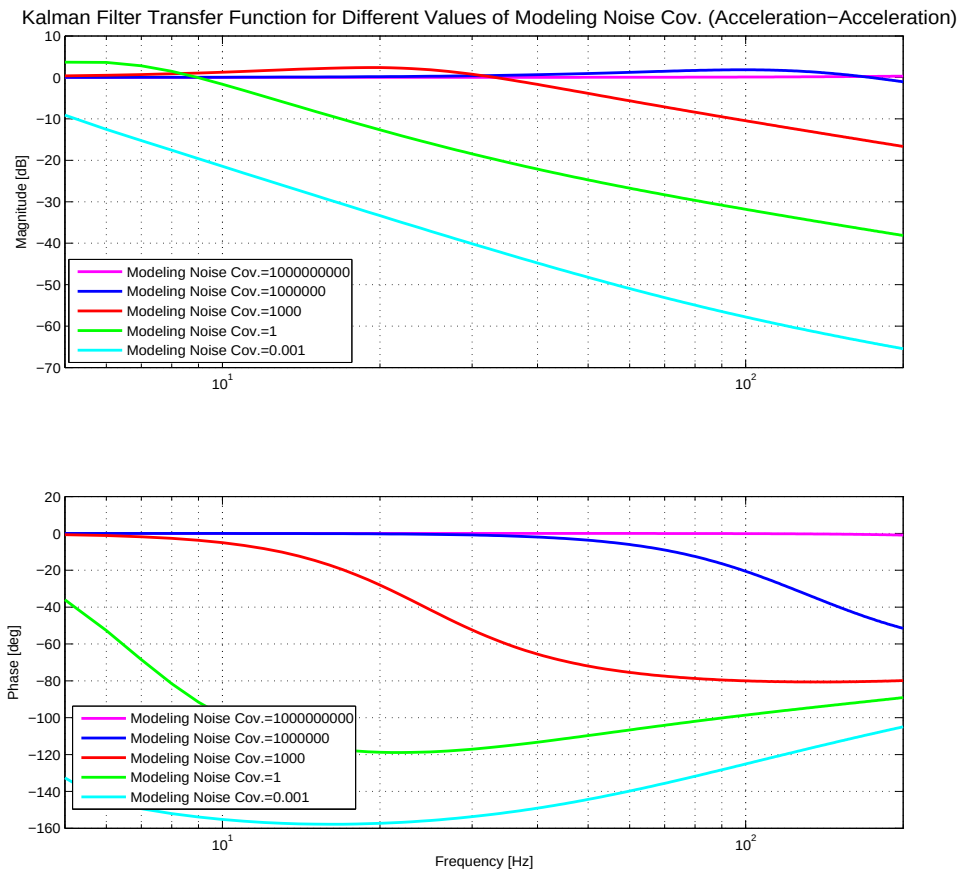

Figure 3.13: Variation of the Kalman Filter Transfer Function Between Input Acceleration and Output Acceleration for Different Values of the Modeling Noise Covariance

Figure 3.12 gives the transfer function of the Kalman filter from velocity input to filtered velocity output for various modeling noise covariance parameters. Figure 3.13 on the other hand gives the transfer function from acceleration input to the filtered acceleration output for the same set of modeling noise covariance parameters. As can be seen from both graphs, increasing modeling noise covariance means modeling errors are higher and measured signals should be trusted more. As a result, input measurement signals are filtered less and better frequency response characteristics in terms of attenuation and phase delay can be obtained. However, noise attenuation characteristics of the filter gets worse for higher modeling noise covariances, which may lead to noise and vibration related problems.

In order to have the best frequency response characteristics possible while having enough noise attenuation, tuning of the filters are done as follows; modeling noise covariance parameter is raised as much as possible to the point where noise amplification and vibrations due to this noise can be observed in the system in close loop control. This point is further tested with different controllers to see the behavior under different control schemes. Finally, the parameter is reduced from this limit value in order to have some margin for variations in system parameters. This method ensures that the best possible frequency response is obtained while high frequency noise contents are filtered out adequately.

Modeling noise covariance value obtained as a result of this method is one billion. Bode plots belonging to the resulting transfer functions are drawn with magenta color in Figures 3.12 and 3.13. One can see the higher phase lag and attenuation plots resulting from smaller values than one billion. It is important to note increasing modeling noise covariance parameter higher than one billion does not result in significant changes in both magnitude and phase plots for the given frequency range of 5 to 200 Hz since this value already results in near ”‘unity”’ transfer function in this range. Although higher frequency ranges can benefit from further increases, these higher frequencies are not of any interest since they lie outside of the intended control range.

3.2.4 Assessment of Feedback Quality Improvement Achieved with the Additional Measurement of Angular Acceleration

In this section, a quick assessment is done on of how measurement of angular acceleration signal in addition to the already measured angular velocity signal improves both angular velocity and angular acceleration feedback quality. However, before any serious comparison can be done, definition of the quality of a signal must be defined.

As the discussion of previous sections suggest, two characteristics of a given feedback signal prove to be important in control applications; one of them being the amount of noise in the signal and the other being any phase delay or magnitude attenuation due to filtering done. As a result, these two characteristics can be used to define the quality of a given feedback signal. Therefore quality of two signals can be compared by equating the covariance of noise present on both signals and comparing the Bode

plots for frequency response.

Covariances of noises present on sample measurements of angular velocity and acceleration signals are previously defined to be 0.0054 and 58.25. If white noises with same covariance values are fed into the Kalman filter tuned in the previous section, the output velocity and acceleration signal noise covariances become 0.00022 and 38.64, respectively. Our goal will be to tune another Kalman filter which runs a similar kinematic model as in the previous case but does not receive acceleration measurement at the input and tune this filter to achieve output velocity and acceleration signals with similar covariances. Once noise covariances are identical, a comparison can be made between the frequency responses.

We start with a comparison of the output acceleration signals. In order to come up with an acceleration output covariance around 38.6, modeling noise covariance parameter of this second Kalman filter needs to be tuned down to 125000. In Figure 3.14, acceleration input-acceleration output frequency response of this new filter is given together with the acceleration input-acceleration output frequency response of the original filter giving the same output acceleration noise covariance. When two Bode plots are compared, the improvement in the frequency response characteristics is clearly visible.

One can see the near unity gain" characteristic of the velocity-acceleration input Kalman filter from the given figure while velocity-only Kalman filter with the same output acceleration noise covariance starts to have lagging phase as early as 20 Hz and has a phase lag of 90°even before 60 Hz. Magnitude response also has a non-desirable shape with a peak around 40 Hz. While the velocity-only Kalman filter performs poorly, the reason for this is obvious; since only the velocity measurement is available to the filter, obtaining the acceleration signal requires the differentiation of the input, which brings the problem of noise amplification with it. As a result, in order to obtain the same output noise covariance with the original filter, heavy filtering of the signal is required which in turn adds phase lag and modifies the magnitude plot of the filter.

For comparing the quality of velocity signals, we equate the output velocity noise covariance of the velocity-only Kalman filter to 0.00022 by lowering the modeling

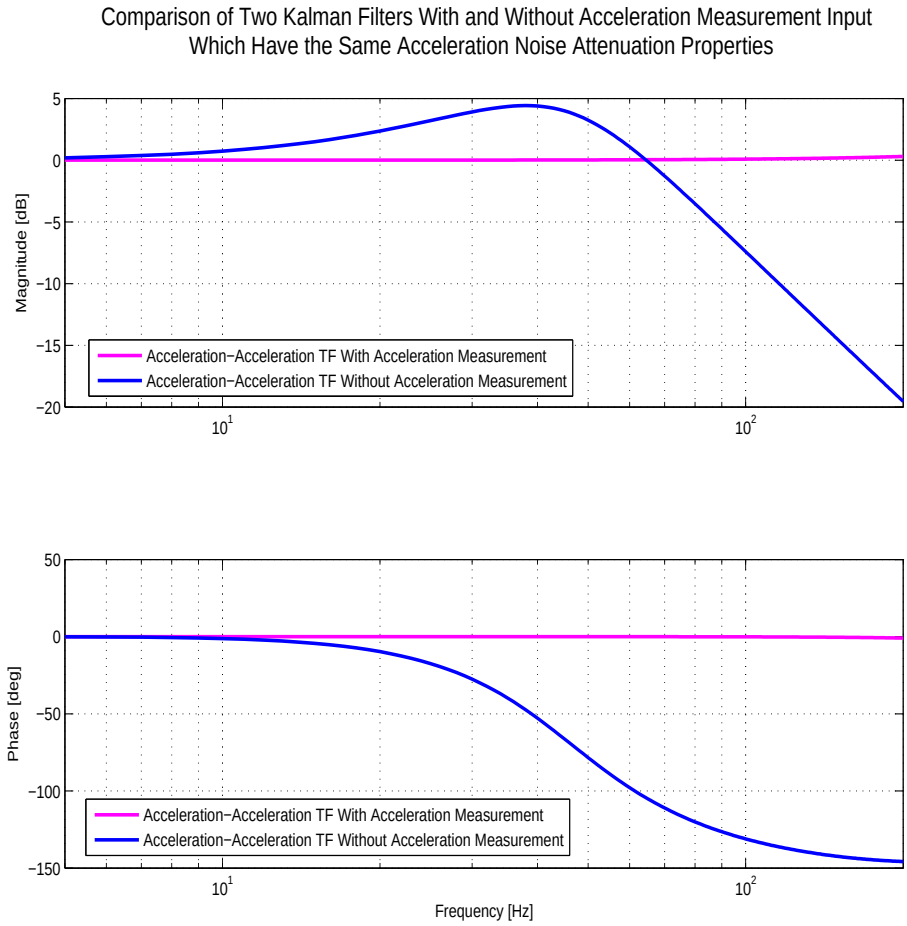

Figure 3.14: Input Acceleration-Output Acceleration Transfer Functions of the Two Kalman Filters Compared; The One With Acceleration and Velocity Input and the One With Only Velocity Input

noise covariance parameter to 750. In Figure 3.15 input velocity-output velocity transfer functions of the two Kalman filters are given. Acceleration-velocity combined Kalman filter once again clearly outperforms the velocity-only Kalman filter.

Acceleration-velocity combined Kalman filter once again exhibits “unity gain” characteristics through all frequencies of interest while phase lag and magnitude distortion starts as early as 20 Hz when the velocity-only Kalman is used. Different from the acceleration case, there exists no differentiation process in the velocity-only Kalman filter therefore no similar reason for excessive phase lag exists and better frequency response characteristics should be observed, however it is not the case.

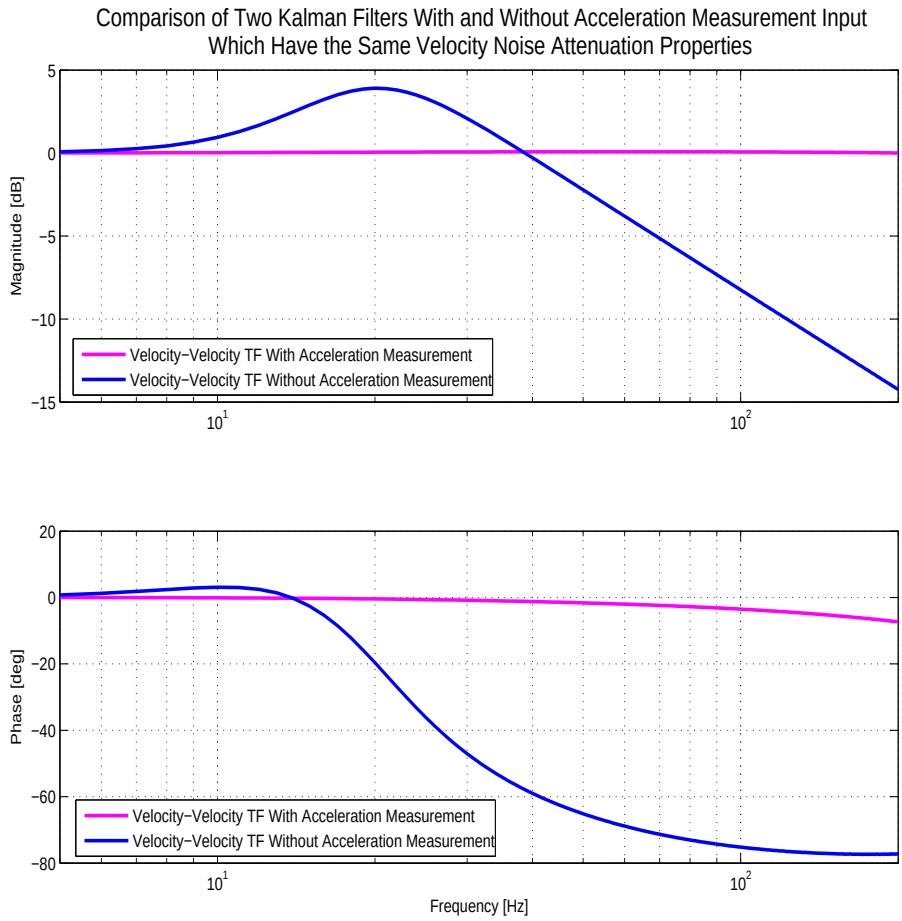

Figure 3.15: Input Velocity-Output Velocity Transfer Functions of the Two Kalman Filters Compared; The One With Acceleration and Velocity Input and the One With Only Velocity Input

Discussion of the last paragraph points towards an important result of using the additional measurement of acceleration in the Kalman filter. When input and output velocity noise covariances for the acceleration-velocity combined Kalman filter are compared, a high amount of attenuation in the velocity signal noise can be seen. This shows the improvement achieved by the addition of another signal to the list of measured signals. For the velocity-only Kalman filter to achieve the same degree of noise attenuation, heavy filtering of the signal is required. This in turn results in phase lag and amplitude distortion in the signal.

Phase lag and amplitude attenuation characteristics together constitute the bandwidth of a filter. Bandwidth can be defined as the frequency where magnitude plot passes

-3 dB or phase plot passes -90°. Filtering of high frequency noise also effects the lower frequency range and reduces filter bandwidth as can be seen in Figures 3.12 through 3.15. Since filter bandwidth directly effects the overall controller bandwidth, a high performance, high bandwidth controller is only possible with high bandwidth filters and feedback signals. Therefore the possibility of improvement in controller performance with the use of acceleration measurement as an additional feedback is evident even from the improvement in filter output signal shown above.

3.3 Construction of the Simulation Model

As stated earlier, for designing and testing different controllers rapidly and easily, a simulation model of the 2-DOF gimbal and the 6-DOF motion simulator is built in Matlab/Simulink. Mechanical parts of the system are modeled using blocks from the SimMechanics blockset which is a specially designed blockset for simulating mechanical systems. Since SimMechanics blocks can be connected to other Simulink blocks through sensor and actuator blocks, it has been possible to implement and test various controllers using this model and since the controller of the experimental setup is also implemented in Simulink, controller designed in simulation model can be directly copied to the real-time control computer with very little modification and used there.

Success of a simulation model directly depends on how detailed the real system dynamics are observed and modeled in the simulation model. For a close approximation of the experimental setup, a careful identification of the plant is carried out which is explained in Section 3.1. Building on to the information given in Section 3.1, details on how this information is used in Simulink environment in order to create a simulation model of the system is given here. In Figure 3.16, the whole model built in Simulink is given.

In order to explain the model better, this section is divided into six parts, each of which gives details about another part of the model which is worth an explanation. These parts are;

- mechanical bodies,

- friction,
- sensor noise and delay,
- motor and driver dynamics,
- compliance in mechanical structure,
- 6-DOF motion simulator.

Explanation of the simulation model starts with a quick review of SimMechanics blockset and continues with the listed items above.

3.3.1 A Review of SimMechanics Blockset

According to [36], SimMechanics blockset can be defined as a blockset of Matlab/Simulink that can simulate the dynamics of multi-body systems by computing the dynamics of the system numerically on the basis of a block diagram representation. This block diagram representation carried out in Simulink environment and is called *Physical Modeling* since unlike normal Simulink blocks, which represent mathematical operations, or operate on signals, these blocks represent physical components and geometric and kinematic relationships directly. The blockset consists of block libraries for bodies, joints, sensors, actuators, constraints and drivers, and force elements. Using these blocks and more advanced ones such as "Joint Stiction Actuator" block which models stiction and friction, modeling of complex mechanical systems which can become very tedious and difficult using traditional modeling techniques, can be done easily and accurately.

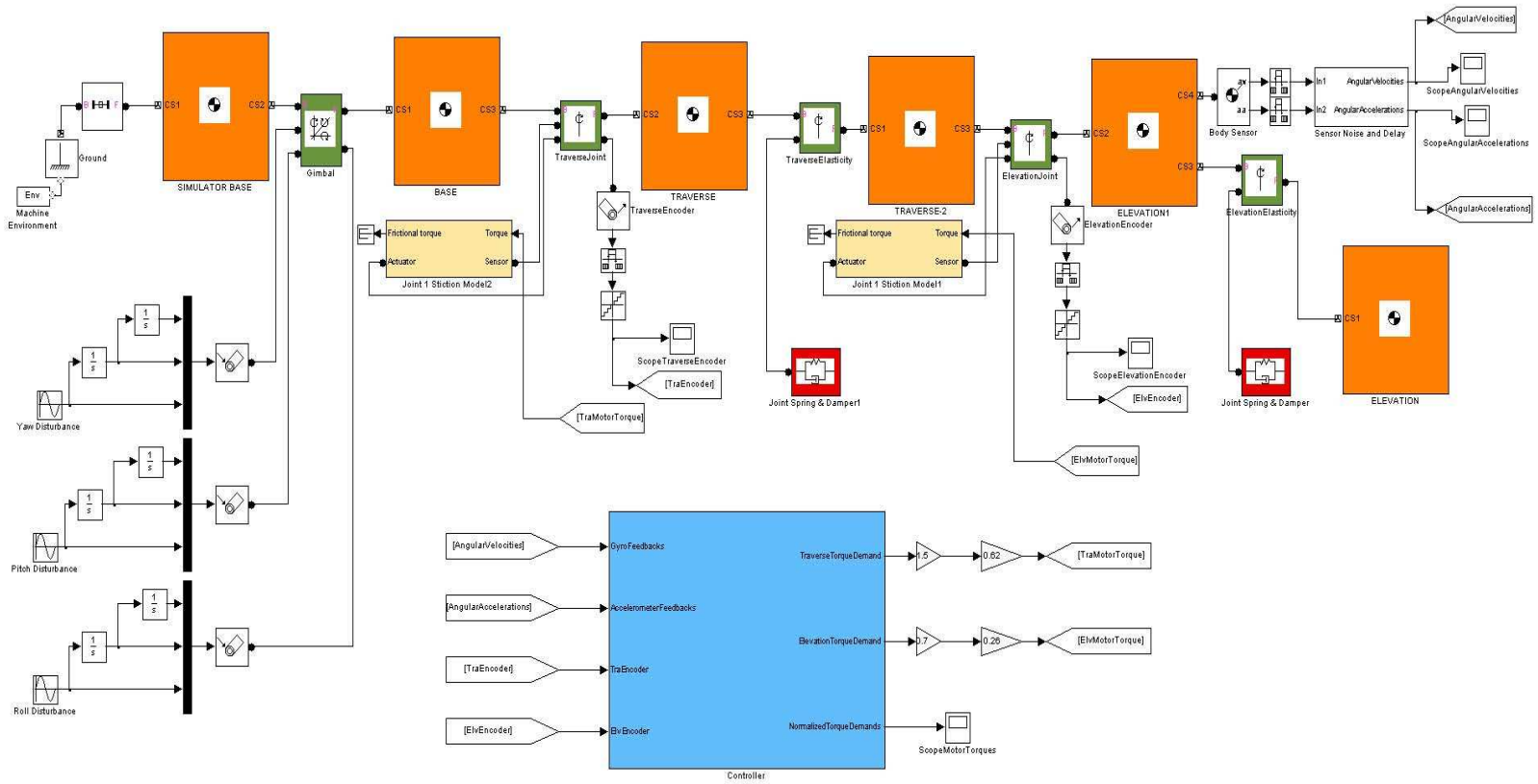

Figure 3.16: Simulation Model of the System Built in Simulink

In our model, the use of SimMechanics blockset makes it possible to model the friction phenomenon very realistically with the help of “Joint Stiction Actuator” block. Modeling of friction is especially important in the simulation model since it is the main source of disturbance that is given to the stabilized platform. Furthermore, with the use of SimMechanics blockset, better visualization tools become available and changing system parameters such as inertias, masses and geometric constraints become very easy, that in turn gives insight about the effects of variation of these parameters on the system performance.

SimMechanics block can be interfaced with other Simulink blocks through the special set of blocks called the sensors and actuators. This makes it possible to implement the controller into the same model in which the system model exists. Once both the plant and the controller are in the same model, implementation and testing of different algorithms can be carried out rapidly and effectively.

3.3.2 Mechanical Bodies

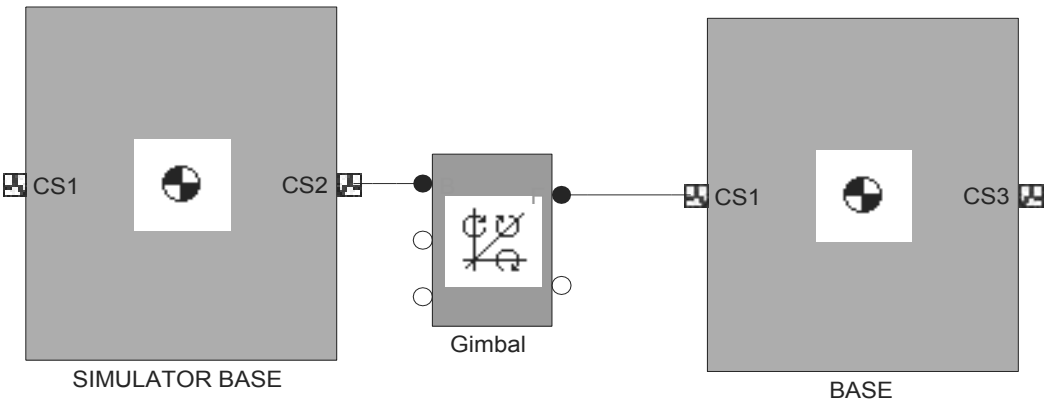

Figure 3.17: SimMechanics Body Blocks and Joints Used for Modeling the Physical Bodies in the System

Figure 3.17 shows two body blocks used in the model, namely the simulator base and gimbal base, connected to each other with a gimbal joint. In SimMechanics, separate bodies which can move relative to one another are modeled with body blocks and are connected to each other with joint blocks. Body blocks represent the inertial properties of the body such as mass and inertia, geometric properties of the body

such as the position of COG of the body and positions of joints connecting the body to other bodies and other properties of the body such as the position and orientation of the body itself. Joint blocks on the other hand represent the degree and type of freedom between these bodies. While the simulation model is being constructed kinematic relations of the bodies in experimental setup are used to define the properties of the joint blocks and above mentioned inertial and geometric properties of the bodies themselves obtained from the CAD models are used to define the properties of the body blocks.

Mainly speaking, four separate bodies are defined in the simulation model built. First one of them is the simulator base which is connected to ground and does not move. Connected to it through a 3 rotational DOF joint representing the motion simulator is the gimbal base. Third body is the gimbal azimuth axis connected to the gimbal base through a revolute joint and finally the fourth one is the gimbal elevation axis connected to the gimbal azimuth axis through another revolute joint. Note that gimbal azimuth and elevation axes are represented with two bodies each, the reason of which will be explained in a later section.

3.3.3 Friction

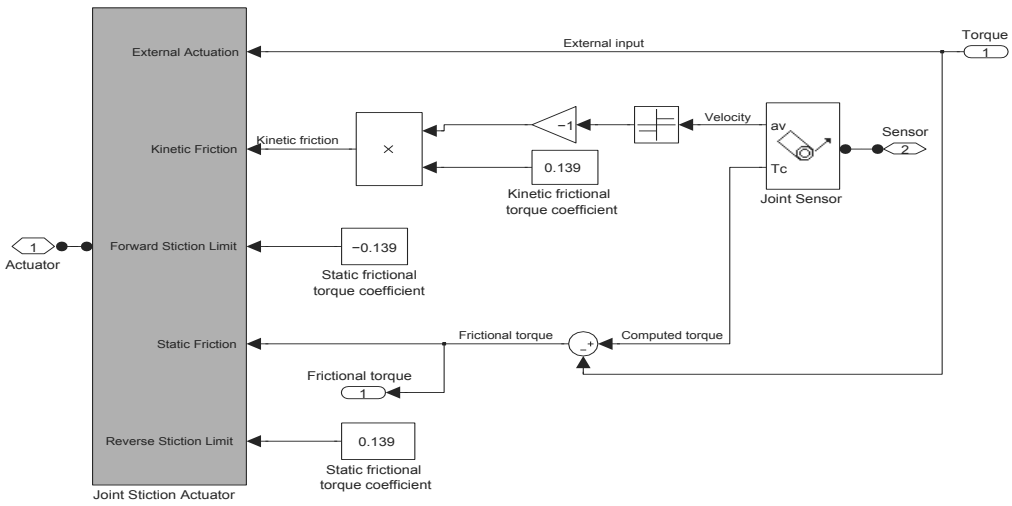

Figure 3.18: Joint Stiction Actuator Block of SimMechanics Which is Used to Simulate the Friction Torques in Mechanical System

Friction exists in the setup in two points, namely the azimuth and elevation bearings. One should note that since direct drive motors are employed in the gimbal, sources of friction such as gearboxes and additional bearings are not present. However, a small amount of friction still exists originating from the motor bearings and it should be included in the simulation model in order to simulate the plant as closely as possible.

In modeling the friction present in both axes "Joint Stiction Actuator" block of Sim-Mechanics blockset is used. Two of these blocks are used in the simulation model, one connected to the joint between gimbal base and gimbal azimuth axis and the other connected to the joint between gimbal azimuth axis and gimbal elevation axis. In Figure 3.18 the use of the block is given in more detail.

A state machine exists inside the joint stiction actuator block which decides if the joint sticks or moves. Its operation can be simplified as follows; once the relative velocity drops below a threshold value, the joint sticks meaning it does not move. Once the stiction occurs, the joint starts its relative motion only when the external torques applied on the joint reaches the static friction value defined. When the joint is moving, a friction equal to the kinetic friction value is applied in the direction opposing the motion.

Note that many different friction models exists in the literature ranging from very simple ones to very complex models. However, since the approach used in this work for friction and disturbance compensation is not a model based one and this friction model will only be used in the simulation model, Coulomb friction model is used. Coulomb friction model is one of the simplest models in which the friction torque is considered to be constant and only changes with the direction of the relative motion.

3.3.4 Sensor Noise and Delay

In a SimMechanics model, sensors can be placed on both bodies and joints in order to measure positions, velocities and accelerations. In an effort to duplicate the sensors on the real system, a body sensor measuring angular velocity and angular acceleration relative to inertial frame is connected to the gimbal elevation axis body for simulating the gyroscopes and accelerometers. Furthermore, two joint sensors measuring relative

angular positions of joints are connected to gimbal joints for simulating the encoders.

It shouldn't be forgotten that sensors placed in the model measure the related quantities without any noise or quantization errors, which is not the case in the real experimental setup since all sensors employ some amount of noise or discretization error in real life. Hence, these errors are introduced into the model artificially. First, encoder discretization is simulated with quantizer blocks, with an azimuth axis resolution of $360/(2048 * 10000) = 0.000018\ deg$ and elevation axis resolution of $360/(2048 * 3600) = 0.000049\ deg$. Second, white noise with covariance equal to the previously measured gyroscope and accelerometer array noise covariances are added to the angular velocity and angular acceleration measurements to simulate noises in these measurements. As a result, all sources of noise are included in the model.

Another factor that degrades sensor measurements is the amount of delay in the signal. There may be multiple sources of this delay such as the sensor itself or the delay originating from transfer and sampling of the signals. From the plant Bode plots given in Figure 3.2 and 3.3 for azimuth and elevation axes, these delays for both velocity and acceleration measurements can be identified as around 1.5 milliseconds, the effect of which is included in the simulation model via "integer delay" blocks.

3.3.5 Motor and Driver Dynamics

Needless to say, motors and drivers used in the system inherit some dynamics of their own. However, when these fast dynamics are compared with the dynamics of the mechanical system, their contribution becomes negligible. Furthermore, when the plant transfer function identification method discussed in Section 3.1.1 is considered, it is seen that the input is the torque command from the controller and the output is the sensor measurements read by the controller, hence the obtained transfer function takes into account not only the dynamics of the mechanical body but driver and motor dynamics are also included. As a result, when this transfer function is implemented into the simulation model in the next section, driver and motor dynamics will also be taken care of and no need exists for modeling these dynamics separately.

3.3.6 Compliances in Mechanical Structure

When under the effects of torques and forces mechanical structures experience all kinds of deformations. No matter how strongly designed the parts are, these deformations always exist. The implication of this to the servo control problem of the structure shows itself when high bandwidth and high performance control of the platform is aimed. When Bode plots of azimuth and elevation axes given in Figures 3.2 and 3.3 are examined, the effects of these deformations can be seen at higher frequencies. Under the rigid body assumption, thinking of the Newton's equation, inertia of the system should act as a pure gain when the transfer function between input torque and output acceleration is drawn. This is in fact the behavior for the lower frequency parts of both plots exhibiting a constant magnitude gain and zero phase lag. However, as higher frequency excitations are given to the system, rigid body assumption starts to fail and deflections start in the mechanical structure. Also called as the modes of the mechanical structure, some of these deflections directly effect the transfer function of the mechanical plant to be controlled, changing it from a constant gain transfer function to one having resonance and anti-resonance characteristics at different frequencies.

When Bode plot of the azimuth axis is studied, a resonance peak around 160 Hz is seen. Experience shows that such a behavior results from a compliance in the mechanical structure between the point of application of the actuating force/torque and the point where measurements are taken. For example, if a compliant shaft with known stiffness and damping is driven by a motor from one end and angular acceleration is measured at the other hand, such a resonance will be observed between the input torque and output acceleration, the frequency of which is decided by the system parameters such as stiffness of the shaft and the amount of total inertia driven.

When Bode plot of the elevation axis is studied on the other hand, a small anti-resonance followed by a resonance can be seen around the frequency of 65 Hz. Experience shows that this is a different case from the previous one and it results from a compliance in the mechanical structure between the point where measurements are taken and an extension of the structure. For example, if previous example is considered once again, if the measurement is done at the motor side of the shaft and the

compliant shaft still exists in the system, such a behavior will be observed between the input torque and output acceleration, the frequency of which is decided by the system parameters such as stiffness of the shaft and the amount of total inertia driven.

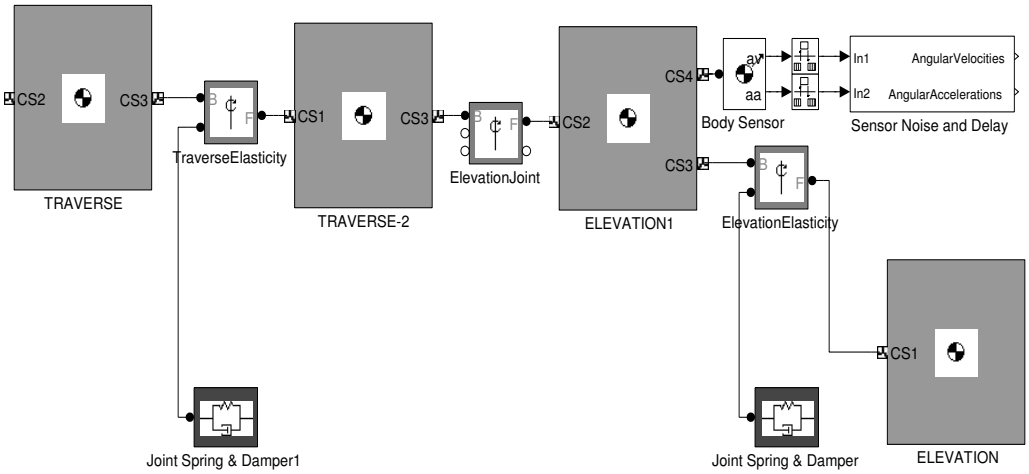

Figure 3.19: Inclusion of Mechanical Structure Compliance Effects in the Simulation Model

Using the discussion of the previous two paragraphs, simulation model of the system is modified as follows to mimic the effects of these compliances in bodies and as a result the resonance and anti-resonance dynamics in high frequency ranges of the transfer functions. Both azimuth and elevation axis masses are divided into two separate bodies and a “revolute joint” together with a “joint spring and damper” actuator is inserted in between as shown in Figure 3.19. This relieves the rigid body assumption and enables the modeling of stiffness and damping inside the mechanical structure. With more bodies defined this way, closer and closer approximations can be achieved. However when the gimbal is being modeled two bodies are used for each axis and the most dominant compliance characteristics are tried to be simulated.

For fitting Bode plots of the simulation model to the actual Bode plots of the system given in Figures 3.2 and 3.3, three parameters; mass ratio of the two divided bodies, spring constant in between the masses and the damping ratio in between the masses are optimized by trial-and-error. Resulting approximations for azimuth and elevation axes are given in Figures 3.20 and 3.21, respectively. Note that low frequency

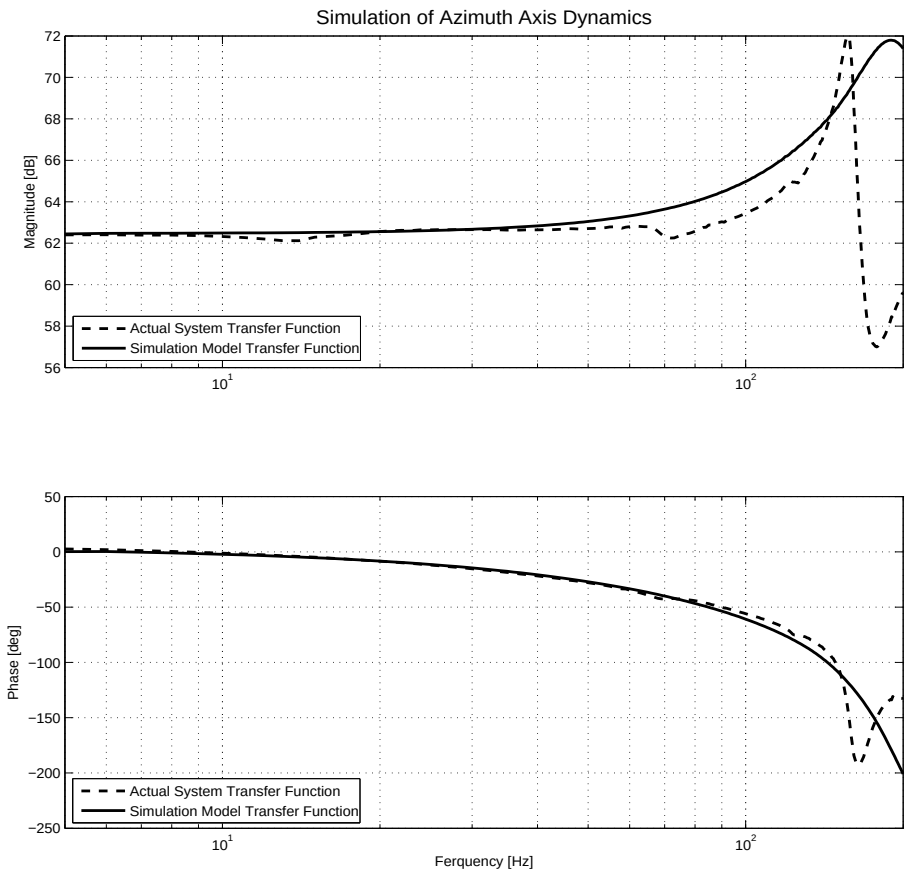

Figure 3.20: Bode Plot Showing the Simulation of Structural Compliances in Azimuth Axis

ranges of both azimuth and elevation plots are nearly identical for the real system and the simulation. In high frequency range however, some differences persist but main characteristics are properly simulated.

3.3.7 6-DOF Motion Simulator

As mentioned before, a 6-DOF motion simulator is used in order to give disturbances to the base of the gimbal platform while the stabilization tests are carried out. As shown in Figure 3.22, for simulating this 6-DOF motion simulator a “gimbal” joint is placed in between two bodies; the simulator base and the gimbal base. This joint permits three rotational degrees of freedom between the connected bodies. Using a

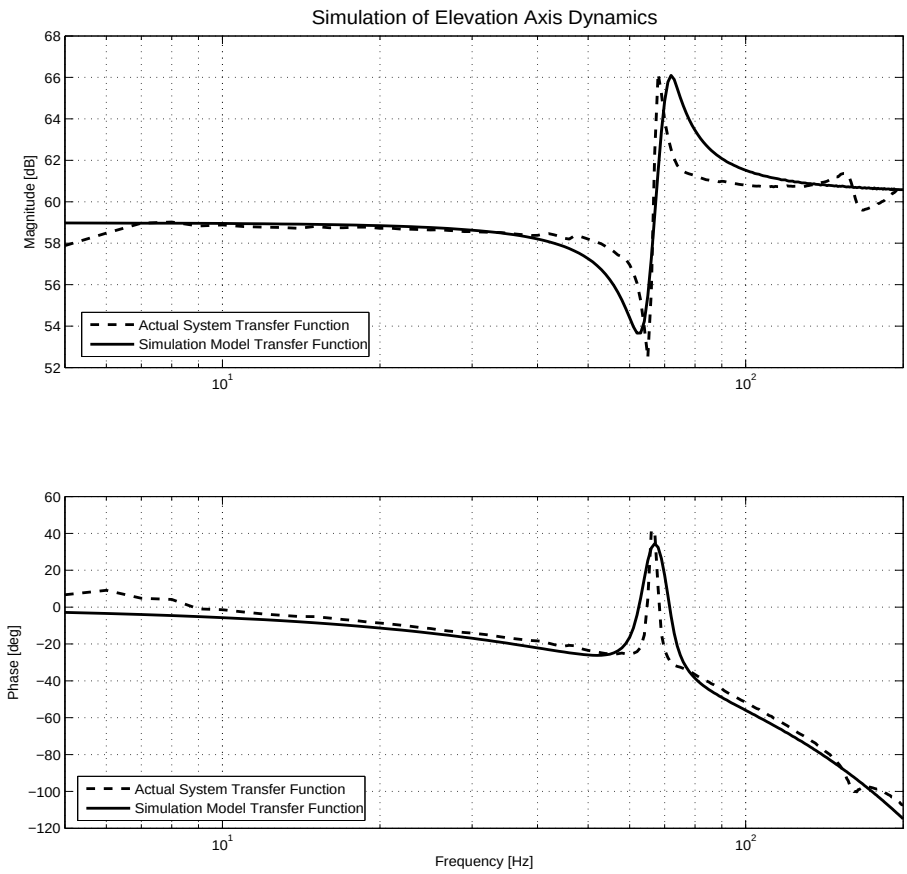

Figure 3.21: Bode Plot Showing the Simulation of Structural Compliances in Elevation Axis

joint actuator, the motion of this joint is defined kinematically in terms of accelerations, velocities and positions of the joint. This scenario is the same as the scenario in real experimental procedure since the 6-DOF motion simulator computer accepts kinematic commands and actuates the platform accordingly.

Note that while the real motion simulator has three rotational and three translational degrees of freedom, the gimbal joint used in the simulation model has only three rotational degrees of freedom. Since only yaw and pitch disturbances will be applied in the tests, translational motion of this joint is irrelevant and is not modeled in the simulation model.

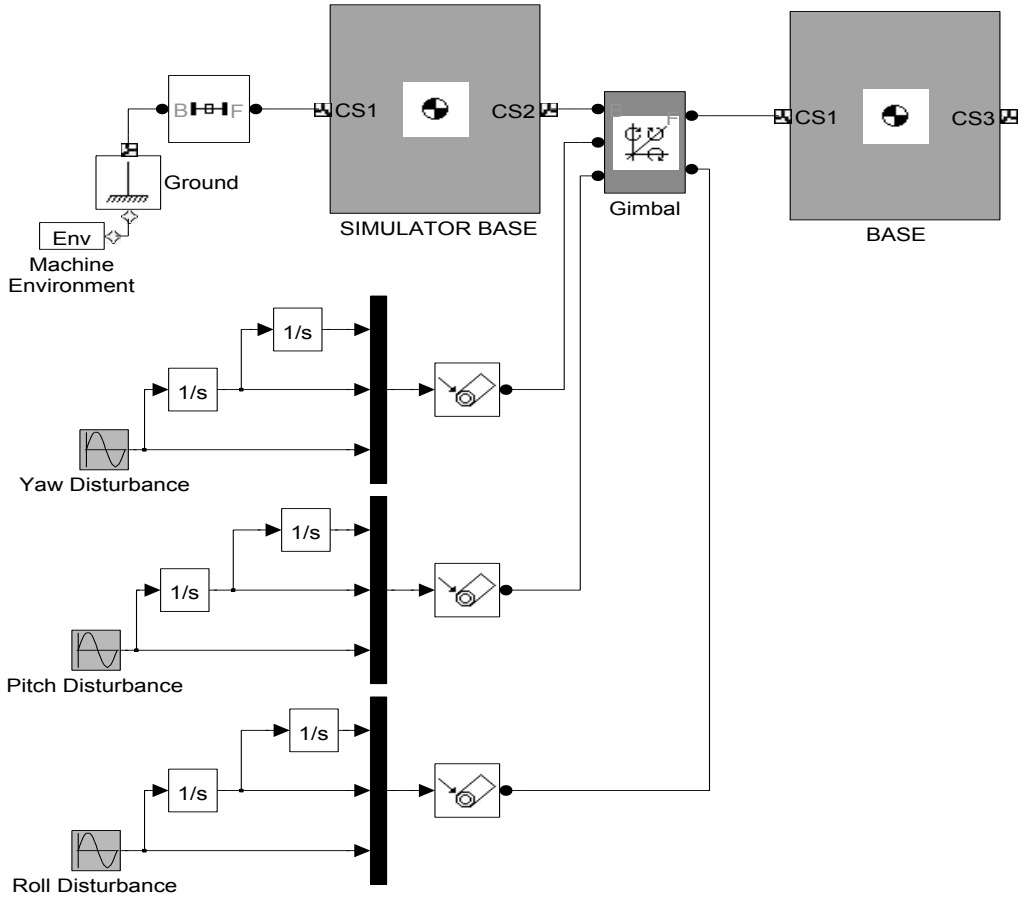

Figure 3.22: Gimbal Joint Which Simulates the Rotational Degrees of Freedom of the 6-DOF Motion Simulator Used

3.4 Controller Implementation and Tuning

Last section dealt with the construction of a proper simulation model in order to be able to implement, tune and test different controllers without the need for setting up the experimental setup and running it. Here in this section, the four controllers, theoretical background of which are given in Chapter 2 will be implemented and tuned on the simulation model. It is aimed to have a 30 degrees phase margin and 6 dB gain margin in all designs as a rule of thumb, however the actual margins obtained may change from controller to controller. Properties of the resulting controllers will be given in terms of their open-loop transfer functions. We start with the standard controller.

3.4.1 Standard Controller

As mentioned in Chapter 2, a standard controller which does not use acceleration feedback techniques is used in order to compare newly designed controllers with. This standard controller is a PII^2 (proportional-integral-double integral) speed controller, which is widely used for stabilization applications that use a rate gyro as feedback [22]. It is important to note that acceleration signal is used in the Kalman filter to improve velocity signal quality even in this controller. Therefore while acceleration feedback signal is not used explicitly, some improvement in velocity signal due to its use in the Kalman filter still exist.

3.4.1.1 Azimuth Axis

A PII^2 speed controller is used together with the Kalman filter developed in the previous sections. Controller gains are tuned to obtain the following open-loop transfer function whose Bode plot is given in Figure 3.23. Resulting open loop transfer function has a phase margin of 32°, and a gain margin of 4.5 dB.

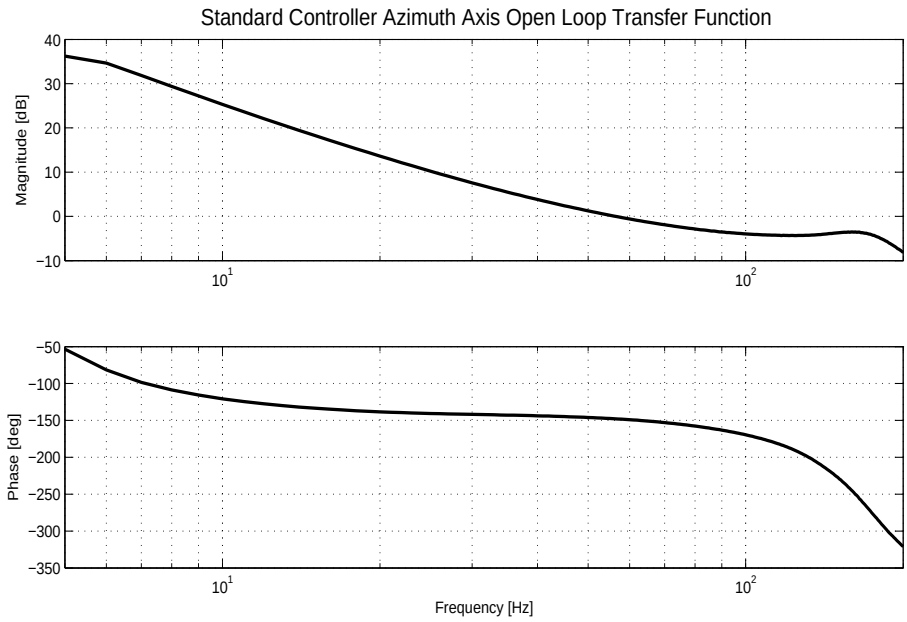

Figure 3.23: Standard Controller Azimuth Axis Open Loop Transfer Function

3.4.1.2 Elevation Axis

A PII^2 speed controller is used together with the Kalman filter developed in the previous sections. Controller gains are tuned to obtain the following open-loop transfer function whose Bode plot is given in Figure 3.24. Resulting open loop transfer function has a phase margin of 37°, and a gain margin of 6.5 dB.

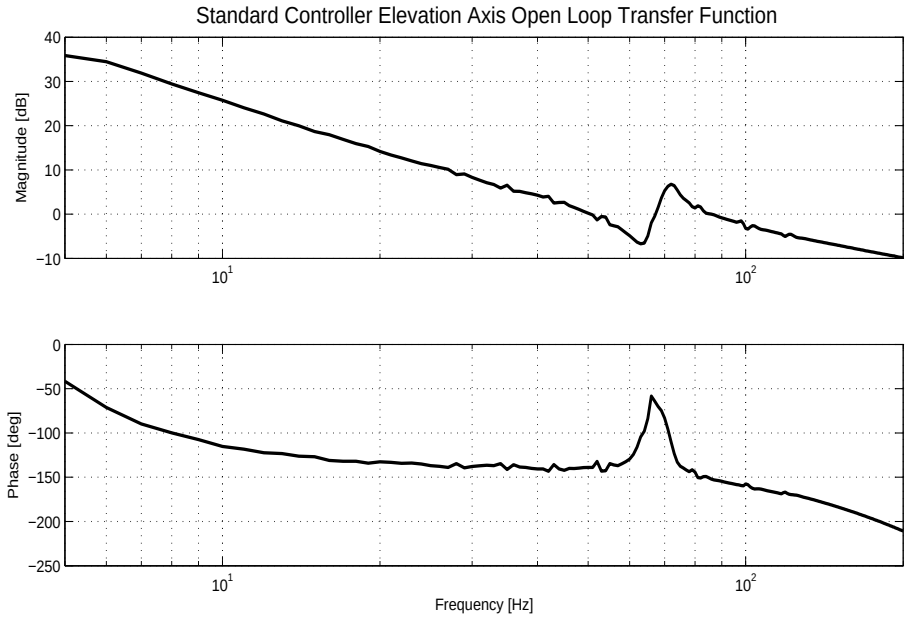

Figure 3.24: Standard Controller Elevation Axis Open Loop Transfer Function

3.4.2 Controller With Load Torque Estimator

This controller uses the standard PII^2 speed controller of the last section. In addition to that a load torque estimator as described in Chapter 2 is implemented in order to reject disturbance torques better. Load torque estimator low-pass filter is selected as a Butterworth low-pass filter with a pass-band frequency of 60 Hz, stop-band starting at 120 Hz and a stop-band attenuation of 40 dB. Resulting azimuth and elevation controllers are as follows.

3.4.2.1 Azimuth Axis

A PII^2 speed controller together with the load torque estimator of Chapter 2 is used together with the Kalman filter developed in the previous sections. Controller gains are kept the same as the standard controller in order to see the improvement obtained with the load torque estimator more clearly. Open loop Bode plot of the controlled system is given in Figure 3.25. Resulting open loop transfer function has a phase margin of 30°, and a gain margin of 4.5 dB.

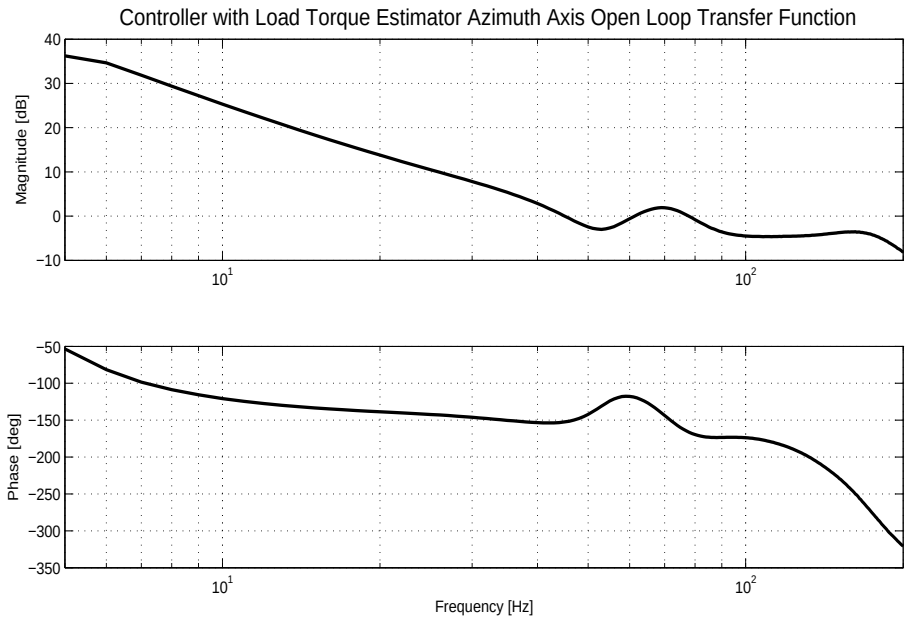

Figure 3.25: Controller with Load Torque Estimator Azimuth Axis Open Loop Transfer Function

3.4.2.2 Elevation Axis

A PII^2 speed controller together with the load torque estimator of Chapter 2 is used together with the Kalman filter developed in the previous sections. Controller gains are kept the same as the standard controller in order to see the improvement obtained with the load torque estimator more clearly. Open loop Bode plot of the controlled system is given in Figure 3.26. Resulting open loop transfer function has a phase margin of 40°, and a gain margin of 7 dB.

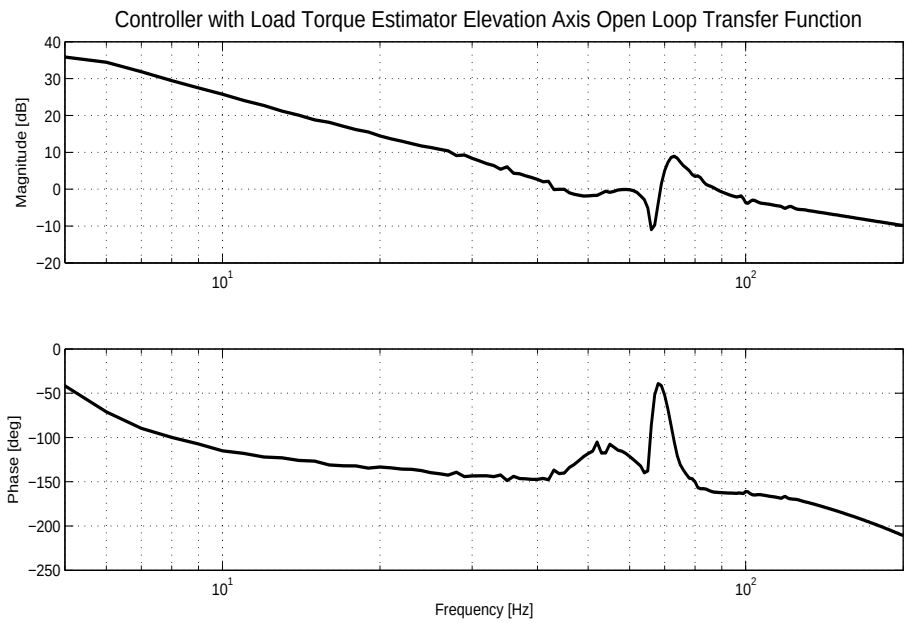

Figure 3.26: Controller with Load Torque Estimator Elevation Axis Open Loop Transfer Function

3.4.3 Controller with Inner Acceleration Loop

As described in Chapter 2, acceleration feedback can be used for closing a fast acceleration loop inside the present velocity loop in order to sense and reject disturbances much faster. Therefore, keeping the PII^2 speed controller structure, a PI inner acceleration loop which uses the angular acceleration signal as its feedback is added. The resulting azimuth and elevation controllers are as follows.

3.4.3.1 Azimuth Axis

A PII^2 speed controller together with an inner acceleration loop as described in Chapter 2 is used together with the Kalman filter developed in the previous sections. Controller gains of the velocity and acceleration loops are tuned to obtain the following open loop Bode plot of the controlled system given in Figure 3.27. Resulting open loop transfer function has a phase margin of 45°, and a gain margin of 4.5 dB.

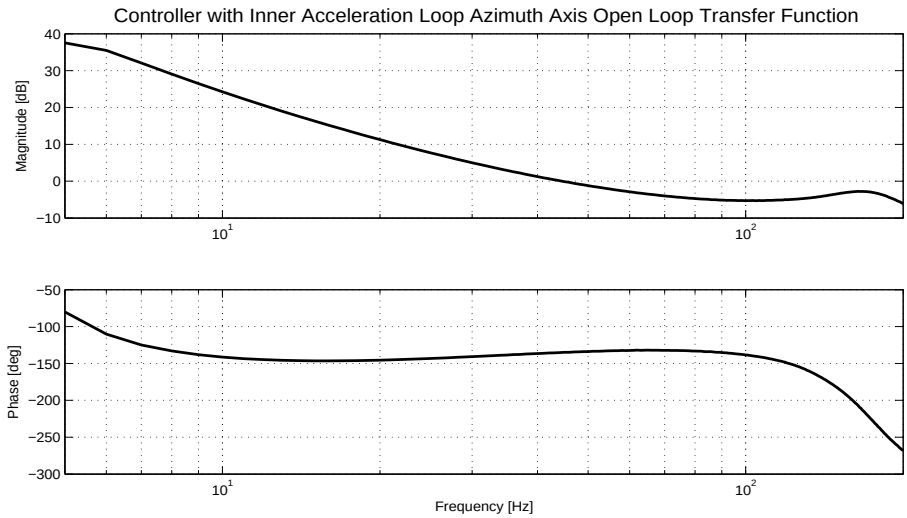

Figure 3.27: Controller with Inner Acceleration Loop Azimuth Axis Open Loop Transfer Function

3.4.3.2 Elevation Axis

An PII^2 speed controller together with an inner acceleration loop as described in Chapter 2 is used together with the Kalman filter developed in the previous sections. Controller gains of the velocity and acceleration loops are tuned to obtain the following open loop Bode plot of the controlled system given in Figure 3.28. Resulting open loop transfer function has a phase margin of 50°, and a gain margin of around 5 dB.

3.4.4 State Derivative Feedback LQR

State Derivative Feedback LQR method has been developed in Chapter 2 for calculating the optimal gain coefficients for the given quadratic cost function. The cost function includes weighted sums of costs associated with the position error, velocity error, acceleration error and magnitude of the input signal. A recursive process is carried out in order to obtain the optimal controllers for both azimuth and elevation axes. The resulting azimuth and elevation controllers are as follows.

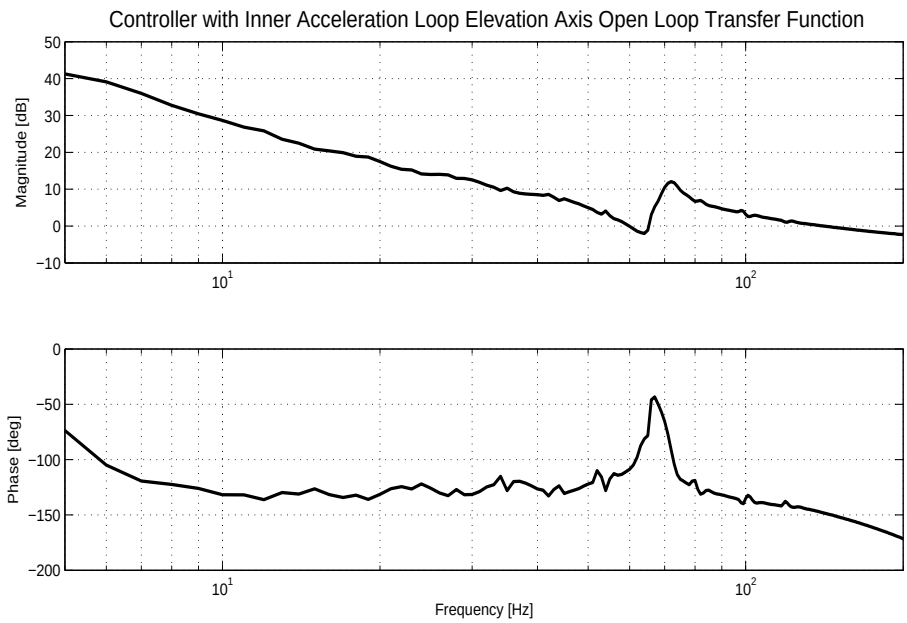

Figure 3.28: Controller with Inner Acceleration Loop Elevation Axis Open Loop Transfer Function

3.4.4.1 Azimuth Axis

State derivative feedback LQR described in Chapter 2 is used together with the Kalman filter developed in the previous sections. Controller gains are obtained by the solution to the state derivative LQR problem given in Chapter 2. Open loop transfer function of the controlled system is given in Figure 3.29. Resulting open loop transfer function has a phase margin of 24°, and a gain margin of 3 dB.

3.4.4.2 Elevation Axis

State derivative feedback LQR described in Chapter 2 is used together with the Kalman filter developed in the previous sections. Controller gains are obtained by the solution to the state derivative LQR problem given in Chapter 2. Open loop transfer function of the controlled system is given in Figure 3.30. Resulting open loop transfer function has a phase margin of 25°, and a gain margin of 3 dB.

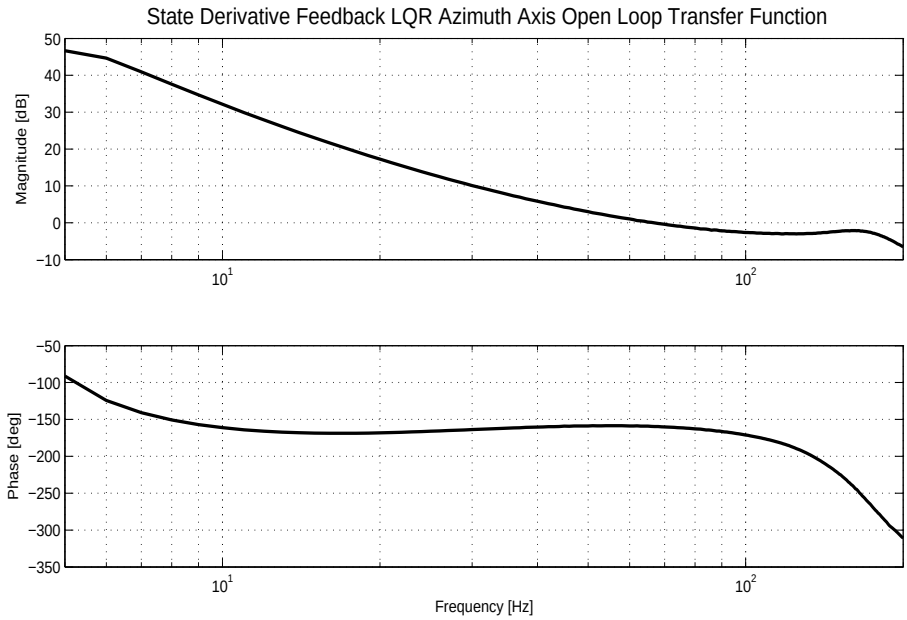

Figure 3.29: State Derivative Feedback LQR Azimuth Axis Open Loop Transfer Function

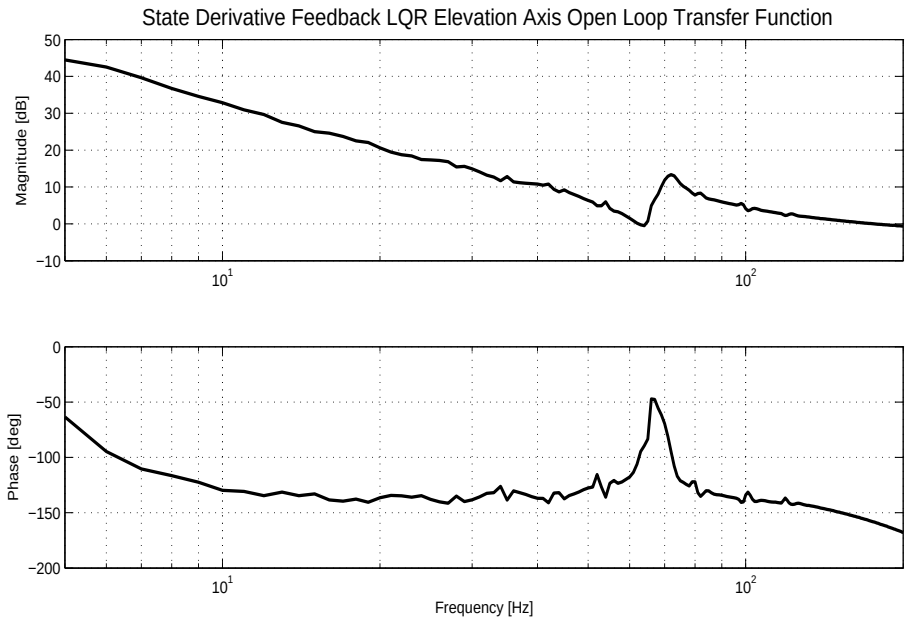

Figure 3.30: State Derivative Feedback LQR Elevation Axis Open Loop Transfer Function

3.5 Simulation Test Results

As presented in the previous section, simulation model is used in order to implement and tune the four controllers that are designed before these controllers are implemented in the real-time controller and tested in the experimental setup. However before work is carried on to the experimental setup, testing of stabilization performances of the four different controllers under different disturbances is done on the simulation model.

Since a very detailed modeling of the physical system is done, realistic results that are close to the actual performance of the real system are expected from these stabilization tests. Therefore, these results will give an insight to the performance of the stabilized platform even before any experiments are carried out. Another benefit of these test will be that comparing the results of simulation tests and experimental tests will provide the means to check the validity and accuracy of the simulation model built.

As mentioned before, the 6-DOF motion simulator is also modeled in the simulation model but with only three rotational DOF. Using this three DOF model of the simulator, kinematic yaw and pitch disturbances will be given to the base of the gimbal platform and stabilization performance will be measured from the inertial body sensors placed onto the gimbal elevation body. Table 3.1 gives the set of sinusoidal disturbances that are going to be applied to the base of the 2-DOF gimbal platform. The amplitudes of these sine waves at each frequency are directly determined from the maximum displacement the motion simulator can supply at that frequency.

It is important to note that these rotational disturbances will act around the center of rotation of corresponding rotation axis; to be more precise, yaw disturbances will act around the center of rotation of azimuth axis while pitch disturbances will act around the center of rotation of elevation axis. Therefore no translational motion is created that can bring together the effects of unbalanced mass centers of the gimbal axes.

A total of forty simulation runs are done in order to test all four controllers with the set of five different disturbances in both elevation and azimuth axes. Although results

Table 3.1: Table showing the disturbances that are going to applied to the base of the gimbal in yaw and pitch directions in stabilization tests

Frequency	Amplitude (peak-to-peak)	
	Yaw Direction	Pitch Direction
0.5 Hz	20°	17°
1 Hz	9.5°	8°
2 Hz	4°	3.5°
5 Hz	0.65°	0.6°
10 Hz	0.08°	0.1°

of these forty tests are given in Table 3.2 at the end of this section, only the graphs belonging to 1 Hz and 5 Hz disturbance profiles are given in order to avoid presenting an excessive number of graphs that repeat themselves since simulation runs prove to be very stable and repetitive. Only the graphs and necessary explanations are given here since comments on the test results are saved for Chapter 4 where the explanation of same tests done on the experimental setup are given and very similar results are obtained.

3.5.1 Azimuth Axis Tests

All four controllers are tested in azimuth axis tests and the results are given for all four of them next.

3.5.1.1 The Standard Controller

Detailed results for 1 Hz and 5 Hz disturbance profiles are given next. Results for all five disturbance profiles are summarized in Table 3.2 at the end of this section.

Frequency 1 Hz, Amplitude 9.5°; Standard deviation of a 20-second stabilization error data obtained by integrating the angular velocity signal is 0.031 mrad. In Figure 3.31, a 5-second stabilization error plot is given as a function of time.

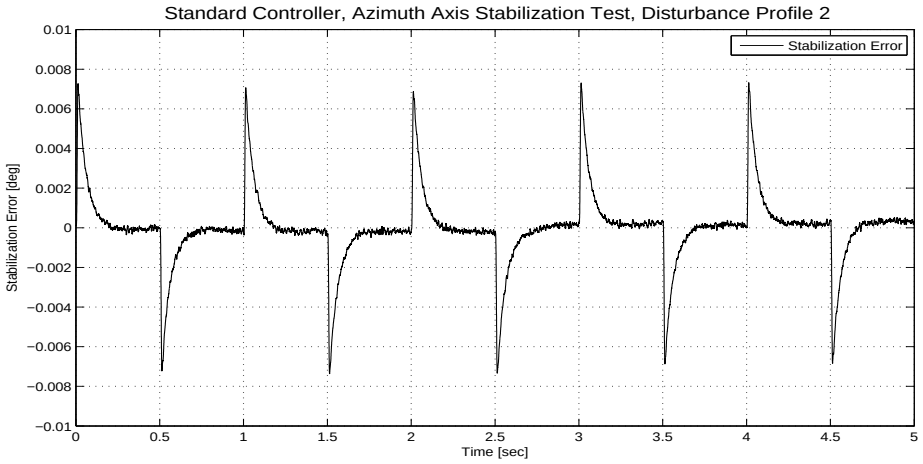

Figure 3.31: Azimuth Axis, Standard Controller, freq. 1Hz, amp. 9.5°

Frequency 5 Hz, Amplitude 0.65°; Standard deviation of a 20-second stabilization error data obtained by integrating the angular velocity signal is 0.060 mrad. In Figure 3.32, a 5-second stabilization error plot is given.

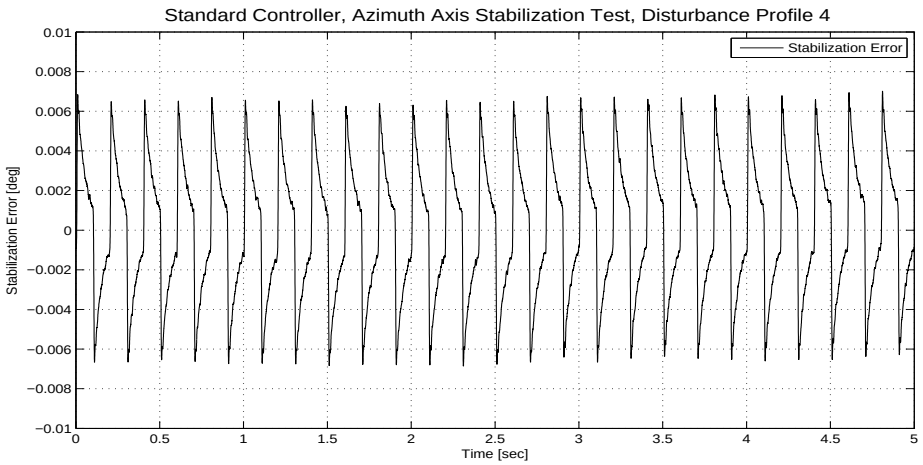

Figure 3.32: Azimuth Axis, Standard Controller, freq. 5Hz, amp. 0.65°

3.5.1.2 Controller with Load Torque Estimator

Detailed results for 1 Hz and 5 Hz disturbance profiles are given next. Results for all five disturbance profiles are summarized in Table 3.2 at the end of this section.

Frequency 1 Hz, Amplitude 9.5°; Standard deviation of a 20-second stabilization error data obtained by integrating the angular velocity signal is 0.022 mrad. In Figure 3.33, a 5-second stabilization error plot is given.

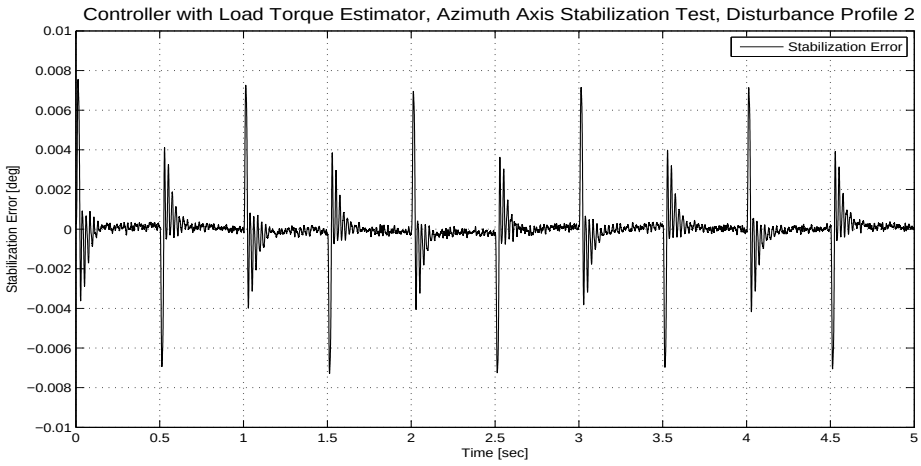

Figure 3.33: Azimuth Axis, Controller with Load Torque Estimator, freq. 1Hz, amp. 9.5°

Frequency 5 Hz, Amplitude 0.65°; Standard deviation of a 20-second stabilization error data obtained by integrating the angular velocity signal is 0.050 mrad. In Figure 3.34, a 5-second stabilization error plot is given.

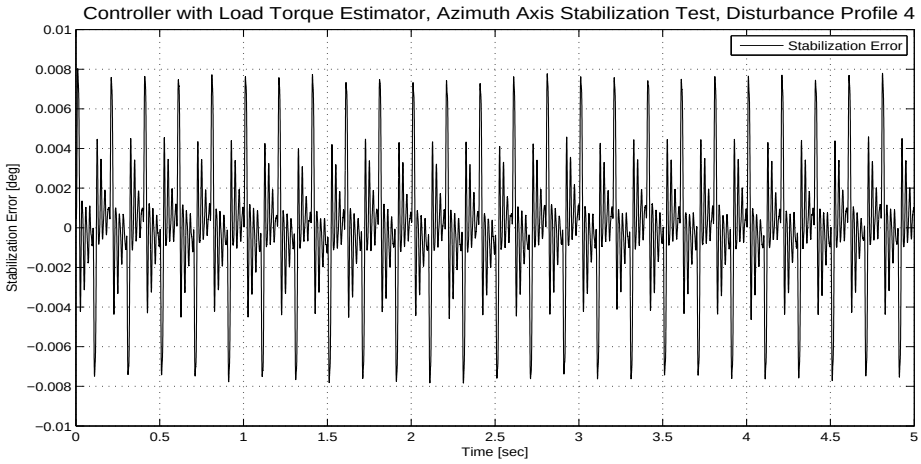

Figure 3.34: Azimuth Axis, Controller with Load Torque Estimator, freq. 5Hz, amp. 0.65°

3.5.1.3 Controller with Inner Acceleration Loop

Detailed results for 1 Hz and 5 Hz disturbance profiles are given next. Results for all five disturbance profiles are summarized in Table 3.2 at the end of this section.

Frequency 1 Hz, Amplitude 9.5°; Standard deviation of a 20-second stabilization error data obtained by integrating the angular velocity signal is 0.016 mrad. In Figure 3.35, a 5-second stabilization error plot is given.

Frequency 5 Hz, Amplitude 0.65°; Standard deviation of a 20-second stabilization error data obtained by integrating the angular velocity signal is 0.034 mrad. In Figure 3.36, a 5-second stabilization error plot is given.

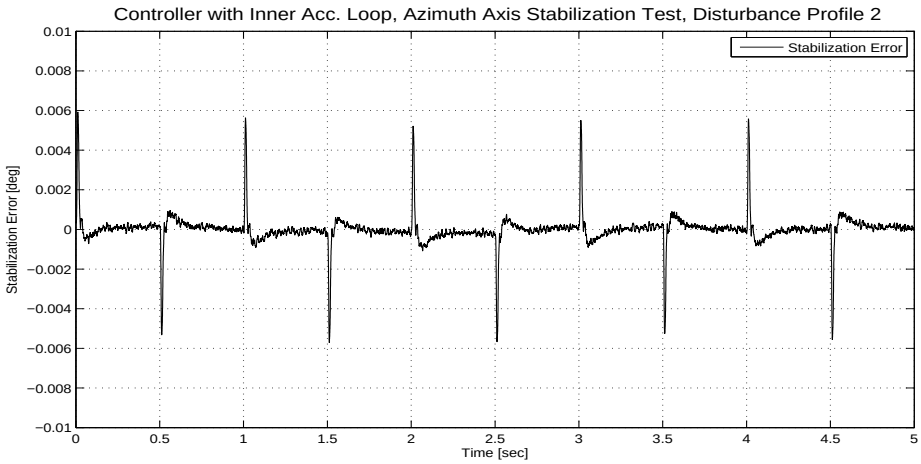

Figure 3.35: Azimuth Axis, Controller with Inner Acceleration Loop, freq. 1Hz, amp. 9.5°

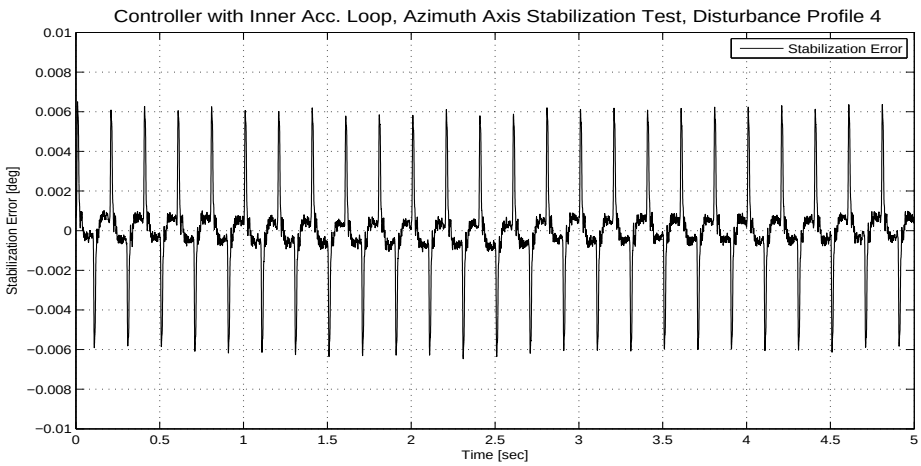

Figure 3.36: Azimuth Axis, Controller with Inner Acceleration Loop, freq. 5Hz, amp. 0.65°

3.5.1.4 State Derivative Feedback LQR

Detailed results for 1 Hz and 5 Hz disturbance profiles are given next. Results for all five disturbance profiles are summarized in Table 3.2 at the end of this section.

Frequency 1 Hz, Amplitude 9.5°; Standard deviation of a 20-second stabilization error data obtained by integrating the angular velocity signal is 0.014 mrad. In Figure 3.37, a 5-second stabilization error plot is given.

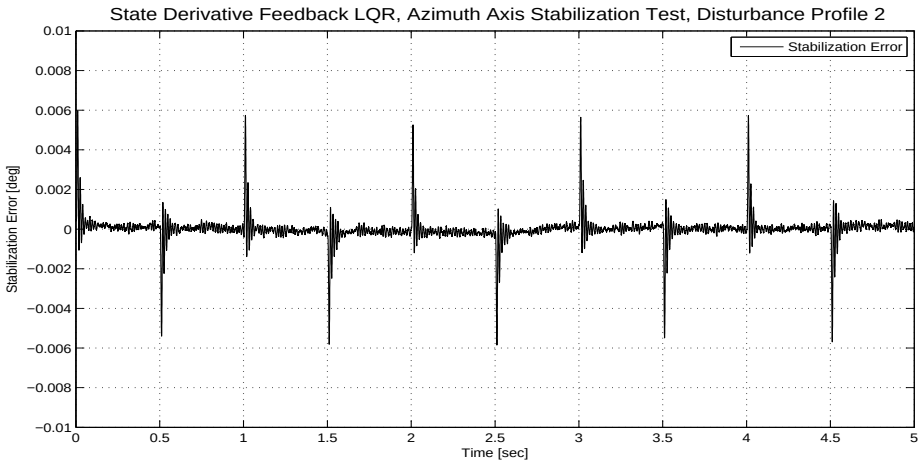

Figure 3.37: Azimuth Axis, State Derivative Feedback LQR, freq. 1Hz, amp. 9.5°

Frequency 5 Hz, Amplitude 0.65°; Standard deviation of a 20-second stabilization error data obtained by integrating the angular velocity signal is 0.029 mrad. In Figure 3.38, a 5-second stabilization error plot is given.

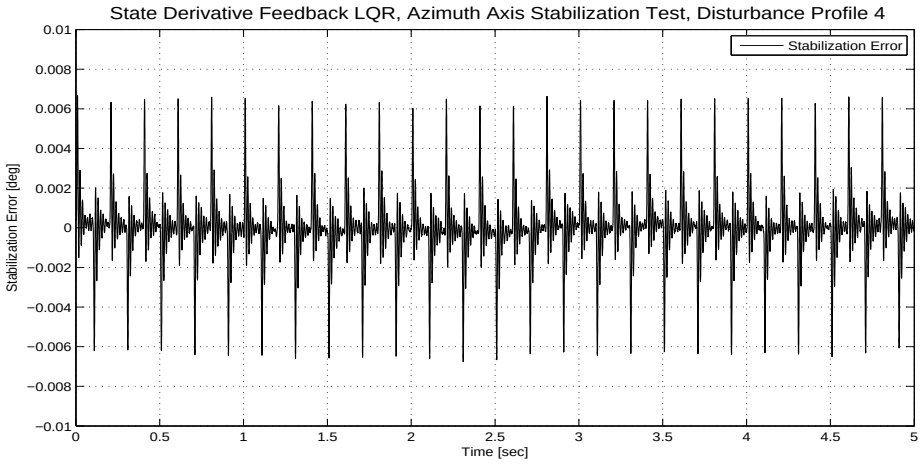

Figure 3.38: Azimuth Axis, State Derivative Feedback LQR, freq. 5Hz, amp. 0.65°

3.5.2 Elevation Axis Tests

All four controllers are tested in elevation axis tests and the results are given for all four of them next.

3.5.2.1 The Standard Controller

Detailed results for 1 Hz and 5 Hz disturbance profiles are given next. Results for all five disturbance profiles are summarized in Table 3.2 at the end of this section.

Frequency 1 Hz, Amplitude 8°; Standard deviation of a 20-second stabilization error data obtained by integrating the angular velocity signal is 0.013 mrad. In Figure 3.39, a 5-second stabilization error plot is given.

Frequency 5 Hz, Amplitude 0.6°; Standard deviation of a 20-second stabilization error data obtained by integrating the angular velocity signal is 0.019 mrad. In Figure 3.40, a 5-second stabilization error plot is given.

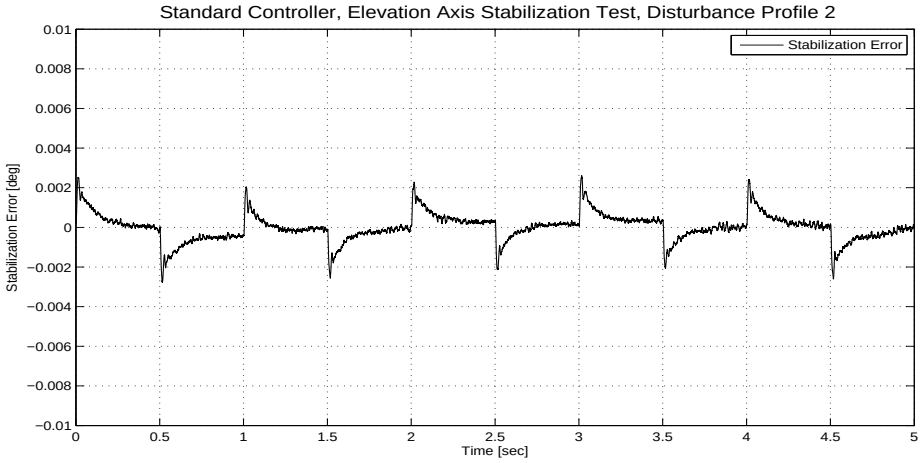

Figure 3.39: Elevation Axis, Standard Controller, freq. 1Hz, amp. 8°

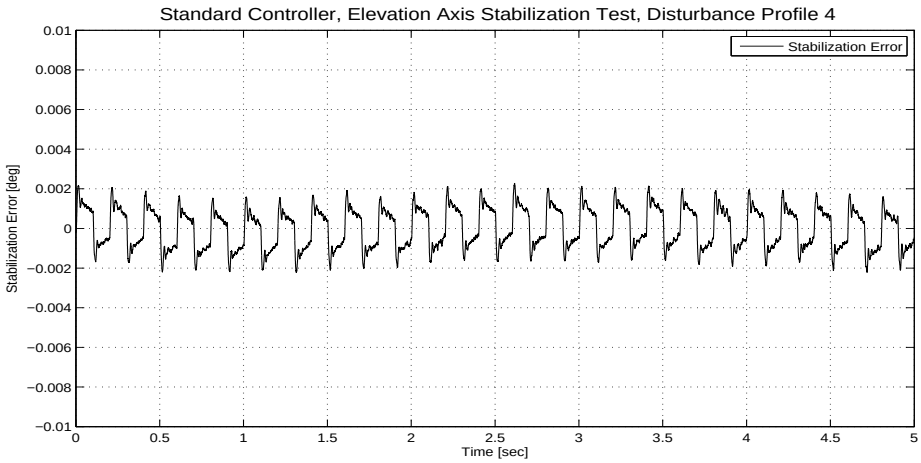

Figure 3.40: Elevation Axis, Standard Controller, freq. 5Hz, amp. 0.6°

3.5.2.2 Controller with Load Torque Estimator

Detailed results for 1 Hz and 5 Hz disturbance profiles are given next. Results for all five disturbance profiles are summarized in Table 3.2 at the end of this section.

Frequency 1 Hz, Amplitude 8°; Standard deviation of a 20-second stabilization error data obtained by integrating the angular velocity signal is 0.009 mrad. In Figure 3.41, a 5-second stabilization error plot is given.

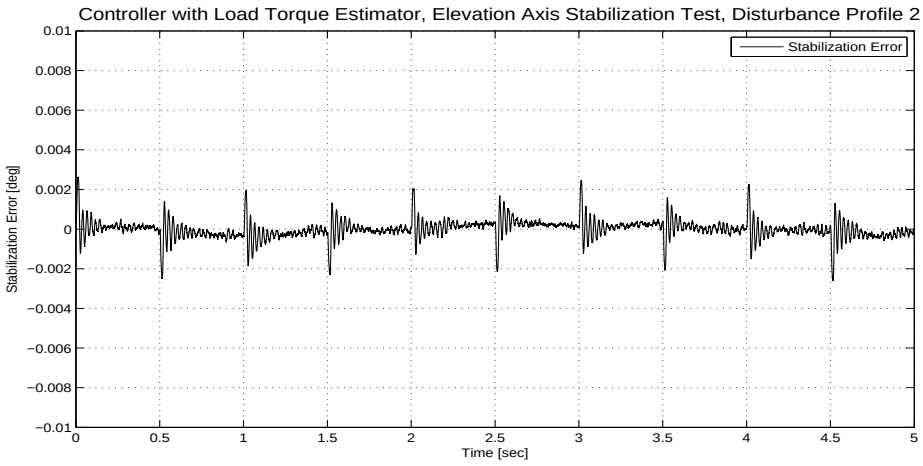

Figure 3.41: Elevation Axis, Controller with Load Torque Estimator, freq. 1Hz, amp. 8°

Frequency 5 Hz, Amplitude 0.6°; Standard deviation of a 20-second stabilization error data obtained by integrating the angular velocity signal is 0.016 mrad. In Figure 3.42, a 5-second stabilization error plot is given.

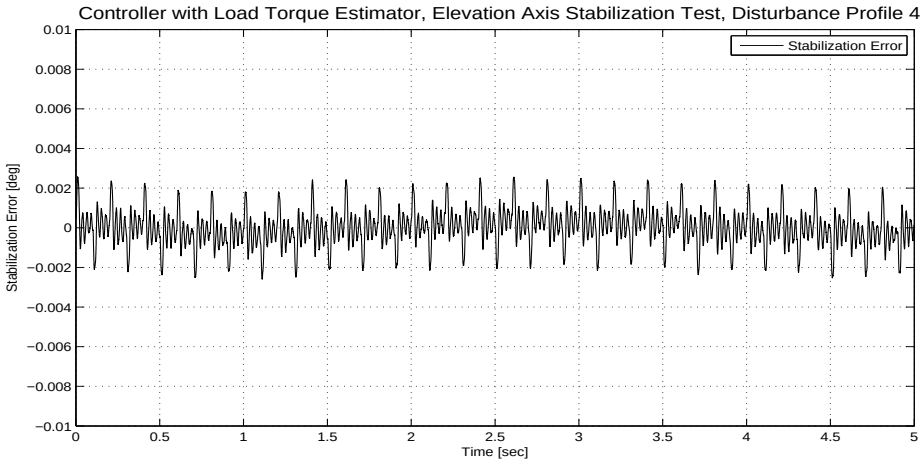

Figure 3.42: Elevation Axis, Controller with Load Torque Estimator, freq. 5Hz, amp. 0.6°

3.5.2.3 Controller with Inner Acceleration Loop

Detailed results for 1 Hz and 5 Hz disturbance profiles are given next. Results for all five disturbance profiles are summarized in Table 3.2 at the end of this section.

Frequency 1 Hz, Amplitude 8°; Standard deviation of a 20-second stabilization error data obtained by integrating the angular velocity signal is 0.005 mrad. In Figure 3.43, a 5-second stabilization error plot is given.

Frequency 5 Hz, Amplitude 0.6°; Standard deviation of a 20-second stabilization error data obtained by integrating the angular velocity signal is 0.009 mrad. In Figure 3.44, a 5-second stabilization error plot is given.

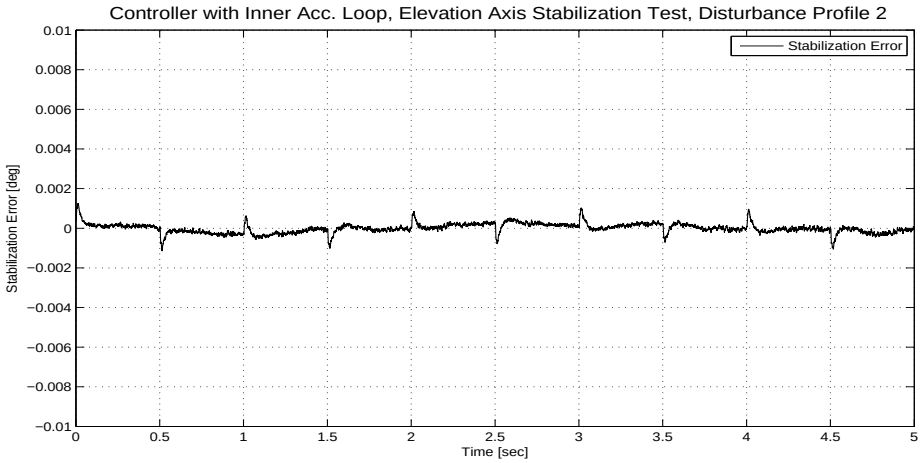

Figure 3.43: Elevation Axis, Controller with Inner Acceleration Loop, freq. 1Hz, amp. 8°

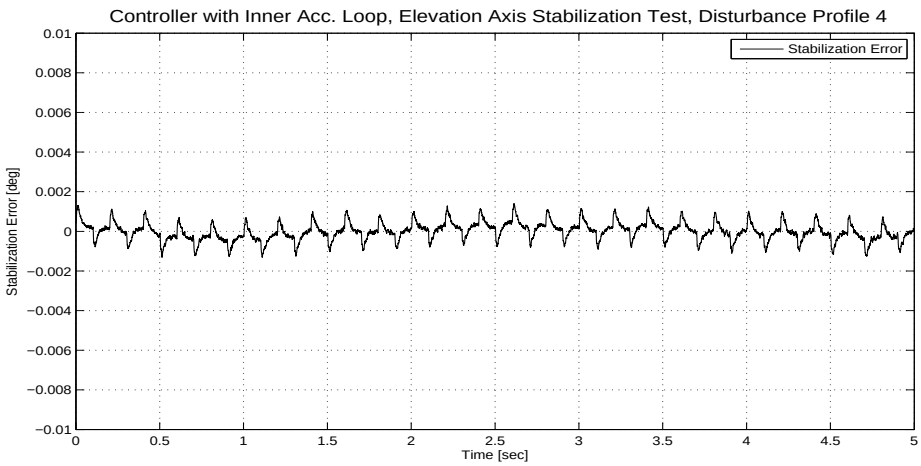

Figure 3.44: Elevation Axis, Controller with Inner Acceleration Loop, freq. 5Hz, amp. 0.6°

3.5.2.4 State Derivative Feedback LQR

Detailed results for 1 Hz and 5 Hz disturbance profiles are given next. Results for all five disturbance profiles are summarized in Table 3.2 at the end of this section.

Frequency 1 Hz, Amplitude 8°; Standard deviation of a 20-second stabilization error data obtained by integrating the angular velocity signal is 0.005 mrad. In Figure 3.45, a 5-second stabilization error plot is given.

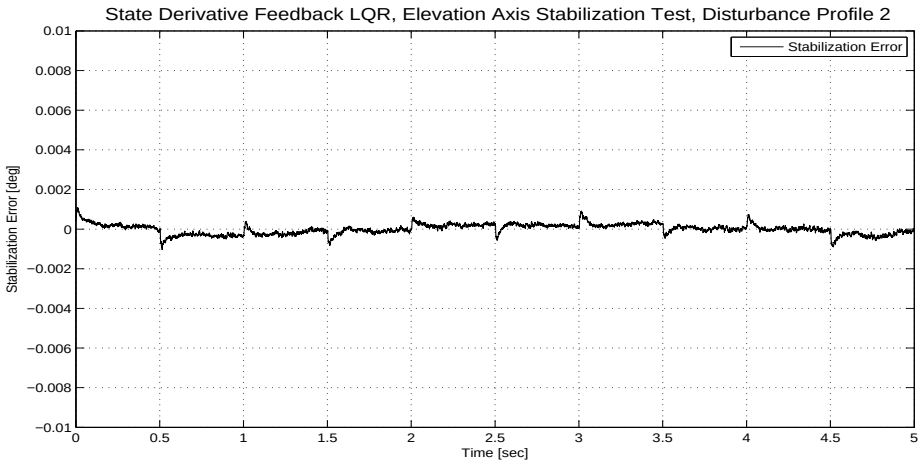

Figure 3.45: Elevation Axis, State Derivative Feedback LQR, freq. 1Hz, amp. 8°

Frequency 5 Hz, Amplitude 0.6°; Standard deviation of a 20-second stabilization error data obtained by integrating the angular velocity signal is 0.008 mrad. In Figure 3.46, a 5-second stabilization error plot is given.

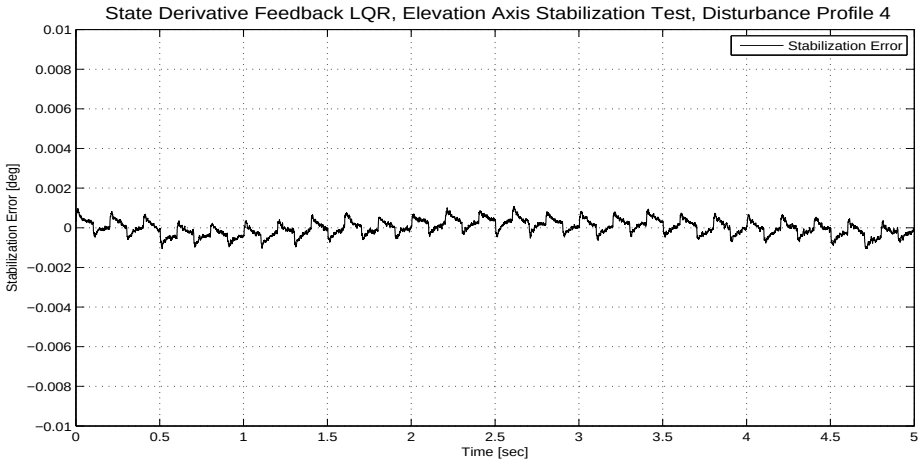

Figure 3.46: Elevation Axis, State Derivative Feedback LQR, freq. 5Hz, amp. 0.6°

3.5.3 Summary of the Simulation Test Results

Table 3.2 summarizes the results obtained in simulation tests.

Looking at the results, the following observations can be made;

- As expected standard controller performs the worst among the controllers tested. However, even the stabilization accuracies obtained with this controller are in par with high accuracy platforms used in military applications. High quality angular velocity feedback obtained as a result of acceleration signal fusion and the rigid mechanical structure which enables high bandwidth controller design can be listed as the main reasons of this satisfactory numbers.
- The overall stabilization accuracy of the elevation axis is much better compared to the azimuth axis. The reason for this is the much lower friction-to-inertia ratio elevation axis has.
- Another general trend which can be seen from the table is that stabilization errors increase with increasing disturbance frequency. This is an expected behavior since regardless of the amplitude of motion given by the motion simulator, the net friction torque acting on the stabilized platform remains the same since a Coulomb friction like friction is present in the system. The frequency

Table 3.2: Table showing the standard deviation stabilization errors achieved with all four controllers for both axes under different disturbances

AZIMUTH AXIS	0.5 Hz	1 Hz	2 Hz	5 Hz	10 Hz
Controller 1	23 μrad	31 μrad	44 μrad	60 μrad	63 μrad
Controller 2	16 μrad	22 μrad	32 μrad	50 μrad	56 μrad
Controller 3	13 μrad	16 μrad	22 μrad	34 μrad	45 μrad
Controller 4	11 μrad	14 μrad	19 μrad	29 μrad	33 μrad
ELEVATION AXIS	0.5 Hz	1 Hz	2 Hz	5 Hz	10 Hz
Controller 1	10 μrad	13 μrad	16 μrad	19 μrad	19 μrad
Controller 2	7 μrad	9 μrad	12 μrad	16 μrad	17 μrad
Controller 3	5 μrad	5 μrad	7 μrad	9 μrad	10 μrad
Controller 4	4 μrad	5 μrad	6 μrad	8 μrad	8 μrad

of the disturbance on the other hand changes frequency of direction changes of friction torque, which is the main source of stabilization error.

- The method of inner acceleration loop and state derivative feedback LQR results in best accuracies while load torque estimator method follows them. The effect of acceleration feedback can be seen clearly through all frequencies; stabilization errors are reduced by nearly fifty percent as a result of the acceleration feedback.

CHAPTER 4

EXPERIMENTAL WORK

Experimental work has been considered as being the most important part of this thesis work and therefore obtaining the results predicted in the former chapters on the experimental setup is the most important outcome of this work. This not only ensures that theoretical and simulation work is realizable, it also is the perfect way of comparing the different controllers designed.

This chapter starts with a brief explanation of the mechanical assembly, sensors and actuators used in the test setup and the electronics and computers involved in the control and data acquisition. Properties of the 6-DOF motion simulator used in the tests to simulate the disturbance profiles is also given. Key points in the selection and integration of the parts are discussed. Later, the usage of the motion simulator in the experimental work is explained together with the test procedure. Next section continues with the results of each experiment run with each controller and different disturbance profiles are given with a brief discussion of the obtained results. Finally, an overall discussion of the experimental results and concluding remarks are presented.

4.1 Design of the Test Setup

In order to test the stabilization performance of our 2-DOF gimbal with the different controllers presented in this theses work, an experimental setup is prepared. This setup is constructed around the Aerotech gimbal, and consists of the designed mechanical interface for mounting the sensors and electronics onto the gimbal, motor drivers, sensors, data acquisition electronics, control and monitoring computer and

the cabling between this elements in addition to the motors and rotary sensors already located in the gimbal itself. Needless to say, the motion simulator Stewart platform is a fundamental part of the test setup, applying the disturbance profiles to the base of the gimbal platform, therefore making it possible to test the actual performance of the stabilized platform under various disturbances. These mentioned parts of the experimental setup will be explained in more detail in the following subsections.

4.1.1 Gimbal Mechanic

Figure 4.1: Aerotech Gimbal Platform Used in the Experimental Setup [37]

2-DOF gimbal which is the product of Aerotech company is shown in Figure 4.1. This gimbal platform has two rotational degrees of freedom which are driven with

direct drive brushless motors. Two hall sensors and two interpolated analog encoders are also integrated into the axes of the platform to supply the required position information for the commutation of the brushless motors. The encoders, being very high resolution can also be used as the feedback for position and speed control loops in applications where relative positions of the axes to the gimbal base is desired to be controlled.

Being designed for precise mirror positioning applications, this mechanical platform has very low friction due its direct drive motors and low friction bearings and sealings and very high drive stiffness again owing to being a direct drive system and having no gearbox or other compliant elements. These two properties together make this platform extremely suitable for servo control applications and makes very high levels of servo performance achievable even without using the techniques developed in this thesis work. In a sense, this makes the objectives of this thesis work harder to reach, trying to improve the performance of an already high performance platform.

4.1.2 Motors

High performance brushless-frameless direct drive DC torque motors are used in both azimuth and elevation axes. These motors come mounted in the gimbal itself and belongs to the S-Series frameless motors product line of the same company, Aerotech. Usage of such direct drive torque motors removes the need for gearboxes and therefore concerns such as backlash and mechanical compliance are eliminated. Due to the quite different inertia values of azimuth and elevation axes, different size motors are used. In the elevation axis, an S-76-35-A type motor with a peak motor current of 8 Amps and a peak motor torque of 2.08 Nm is used whereas in the azimuth axis a bigger S-130-39-A type motor with a peak motor current of 15.2 Amps and a peak motor torque of 9.42 Nm is used.

Figure 4.2: Elmo Digital Servo Drive Unit Used in the Experimental Setup [38]

4.1.3 Motor Drivers

Two Elmo Advanced Whistle motor drivers are used in order to drive the brushless DC motor used in the assembly, one for the azimuth and the other for the elevation axis. These miniature digital servo drives, which can also be seen in Figure 4.2, in spite of their very small size, can supply a peak current of 15 Amps at a DC voltage as high as 100 Volts, which is adequate for both motors of the gimbal. These drivers are used in the so called torque mode in our experimental setup, in which the driver accepts an ±10 V analog reference signal and tries to create a current(and therefore torque) in the motor windings according to the input signal, therefore acts as a torque controller. This enables implementation of speed and position loops outside of the servo drive, most of the time in a real-time computer as it is the case in our experimental setup.

Another key feature of the used servo drive is its ability to emulate encoder signal it reads from the gimbal and output it as an emulated incremental encoder output.

This is an important feature because the real encoder signals come directly to the driver for commutation purposes, and this position signal is also needed for closing the position and speed loops. However, since these loops are not closed inside the driver in our setup, feedback signals have to be provided to the real-time computer somehow. By supplying the emulated encoder output of the drivers to the real-time computer, this is accomplished. This emulated signal has the same resolution with the real encoder signals but it mimics an incremental encoder rather than the original interpolated analog encoders present on the system.

4.1.4 Rotary Sensors: Encoders

To supply the angular position feedback for this high performance gimbal platform, very high resolution, precise encoders are used in both axes which are supplied with the gimbal itself. Analog interpolated encoders (also called as analog sine/cos encoders) are used in both azimuth and elevation axes of the gimbal. Azimuth encoder can count 10 million steps in a single revolution of the azimuth axis while elevation encoder can count 3.6 million steps in a single revolution of the elevation axis. These very high resolution angular position signal makes it possible to control the gimbal platform with high precision in many applications.

In spite of being very reliable and high resolution sensors, encoders mounted on the gimbal are not used as the main feedback sensors in our application of stabilizing the platform. This stems from the fact that stabilization requires controlling the angular position and angular velocity of the platform relative to inertial frame and therefore requires the usage of inertial sensors such as gyroscopes and accelerometers. However, the sensor placement on the gimbal makes it necessary to know at least the relative orientation of elevation axis to azimuth axis since all inertial sensors are mounted on elevation axis and a coordinate transformation is required to correctly measure the motion of the azimuth axis from sensors located on elevation axis. This relative orientation can be obtained from elevation encoder.

4.1.5 Inertial Sensors: Rate Gyros

Tactical grade high precision fiber optic gyros are used for inertial angular velocity measurement of the gimbal platform. These DSP-3000 single axis gyros manufactured by the company KVH can measure angular velocities up to 375 °/s and have low noise characteristics. In addition, these gyros have a relatively high bandwidth(up to several hundred Hz, around 400 Hz) making them suitable for high performance control and stabilization applications and therefore suitable for our application. In order to obtain a full set of angular velocities including all three rotational axes, three mutually perpendicular gyros are mounted on the elevation axis. Signals from these three gyroscopes are first sent to an electronic interface card mounted on the gimbal itself not far from the gyros themselves because this raw signal degrades rapidly while being carried over a wire. From there, signal is sent to the real time computer over a serial communication line, where it is used as the angular velocity feedback for the control of both azimuth and elevation axes.

4.1.6 Inertial Sensors: Accelerometer Array

An array of linear accelerometers are used for the purpose of constructing angular acceleration information of the stabilized platform. The number and orientation of the required linear accelerometers are discussed in great detail in Chapter 2 of this report. As can be seen, discussions have led to an optimal accelerometer placement with one central triaxial accelerometer and three others located at equal distances along the three unit vectors (which are also coincident with accelerometer measurement axes) pointing outwards from this central accelerometer. Once again, as it is discussed in Chapter 2, placing the linear accelerometers away from each other decreases the measurement range of angular acceleration but at the same time it also decreases the amount of noise on angular acceleration signal. Since noise is a very important concern in our application, the accelerometers are placed as far away from each other as the mechanical constraints permit, this distance between accelerometers ending up being 125 mm.

Four ASC5411LN piezo-capacitive triaxial accelerometers of Advanced Sensors Cal-

ibration (ASC) company are used in the experimental setup. These 5g range, high precision sensors are selected to have low output noise characteristics and have a frequency response starting at 0 Hz, meaning that it can measure low frequency inertial accelerations down to DC. This last property has proved to be especially important through the course of accelerometer selection since the main area of usage for accelerometers is the sensing and measurement of shock and vibration and accelerometers designed for this purpose excel at high frequency high amplitude accelerations while being incapable of measuring low frequency acceleration content and therefore should be avoided.

Measured linear acceleration signals are received by the real time computer from the analog input channels of the NI data acquisition card and after the conversion to angular accelerations is done as described in Chapter 2, a full set of three angular accelerations are obtained for the stabilized platform. These signals are used as the angular acceleration feedback for the control of both azimuth and elevation axes.

4.1.7 Data Acquisition Hardware: Serial Interface Card

This card is one of the two data acquisition cards used on the real time computer to establish the interface between the computer and the actuators/sensors. It is a custom electronic card designed and manufactured in ASELSAN which has a programmable FPGA chip on board that can be programmed to accomplish various tasks. In our experimental setup, the duty of this card is to establishes the communication of real time computer with the encoders and gyros, reading the signals coming from these sensors.

4.1.8 Data Acquisition Hardware: Digital/Analog I/O Card

The second data acquisition card being used is National Instruments' 6031E data acquisition card. This card has 64 single-ended or 32 differential 16 bit analog inputs, 2 16 bit analog outputs and 8 programmable digital I/O's. In our application 12 of these differential analog inputs are used to read signals from 12 accelerometers to the real-time computer and the two analog outputs are used in order to send the control

torque reference signals from the real-time computer to the motor drivers.

4.1.9 Real Time Control and Monitoring Hardware and Software

A PC with E8400 dual core 3 Ghz processor and 2 GB RAM, running under Microsoft Windows XP operation system is used as both the real-time control computer and signal monitoring computer thanks to Real Time Windows Target toolbox of Matlab/Simulink software, making it possible to create a kernel for real time applications on a windows based system and enabling the user to monitor the controller and signals using this same computer. Matlab/Simulink version 2009B with Real Time Workshop and Real Time Windows Target toolboxes is used for this purpose.

The controller is implemented in Simulink environment. The controller model runs in real-time with two different sampling rates of 1 kHz and 5 kHz for different parts of the model. Direct access to the controller model for parameter changing and signal monitoring is possible in RTWT environment. This capability enables rapid development and tuning of different controllers in a relatively short amount of time.

4.1.10 Mechanical Interface Parts

Inertial sensors and related electronic cards are required to be mounted on gimbal elevation axis in order to measure angular velocities and accelerations of the platform. Therefore mechanical parts are designed for the mounting of these sensors and cards onto the platform. These parts have to be carefully designed and manufactured with tight tolerances since the relative position and orientation of these sensors are very important in order to get correct measurements. Therefore, a computer aided drawing software, NX I_deas, is used for the design environment. In Figure 4.3, the gimbal platform is shown from two different points of view. In this drawing, the small cyan rectangles can be identified as the accelerometers, while blue rectangles are the gyros, the dark green platform is the Aerotech gimbal itself and the yellow parts are the designed mounting parts.

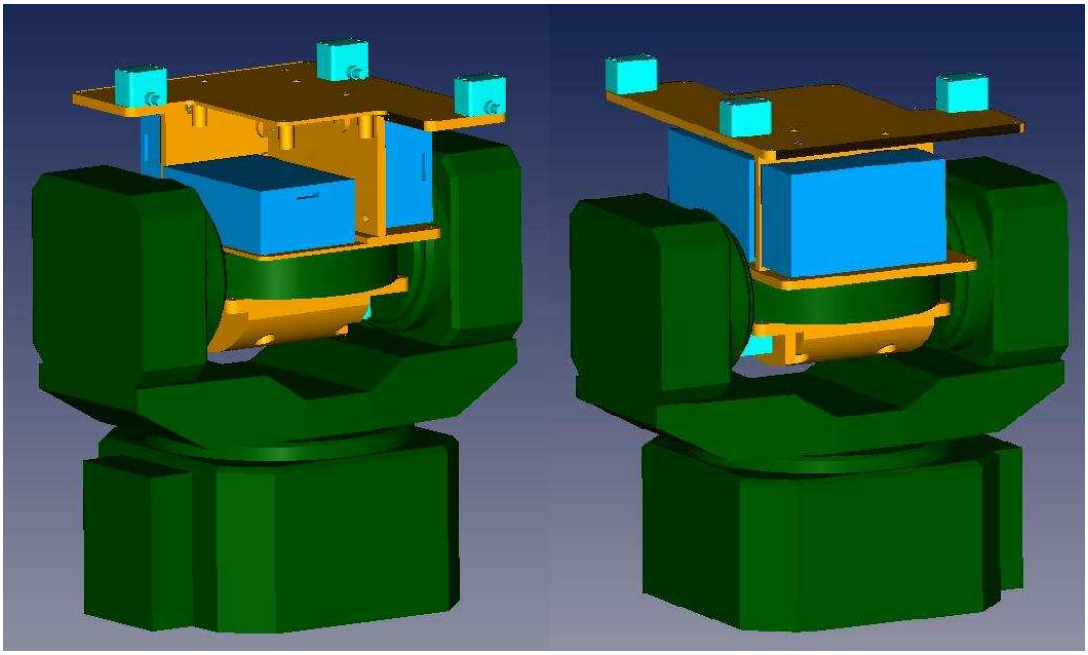

Figure 4.3: Computer Aided Drawing Model of the Gimbal Assembly

4.1.11 6-DOF Motion Simulator Platform

In order to carry out the stabilization tests a controllable disturbance has to be given to the base of the gimbal. For this purpose, a 6-DOF motion simulator, also called as a Stewart platform, is used. This 6-DOF platform, which can also be seen in Figure 4.4, is able to simulate any motion of a platform within its position, speed and acceleration limits. Motion is created by six linear actuators driven with electric motors, which are all connected to a real-time motion control computer which calculates the required motion of individual actuators in order to create the desired platform motion. Therefore the user of the motion simulator only defines the motion profile to be created as a combination of three translational and three rotational motions in platform coordinate frame and the task is executed.

Below, some properties and limits of the motion simulator is given in Table 4.1. Note that, only the yaw and pitch axis motions are made use of in our experiments.

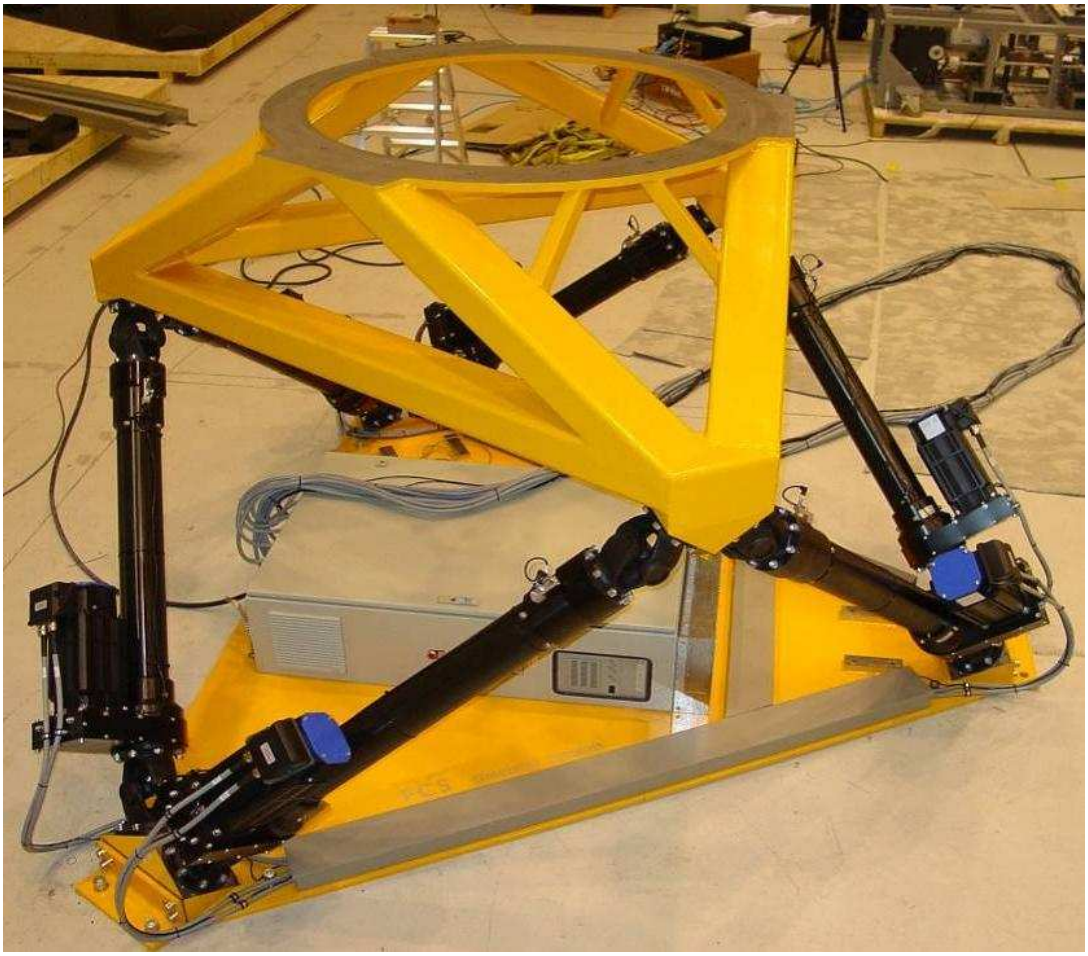

Figure 4.4: 6-DOF Motion Simulator Used in the Experiments

4.2 Experimental Method and Procedure

The aim of the experimental work is to compare the different control algorithms designed and see how stabilization performances vary in the physical setup with different controllers under different disturbance levels. The disturbance level mentioned here is the amount of angular motion of the base of the platform while the performance is identified as how good the controller can reject this motion at the stabilized platform. How good the rejection is done is measured by looking at the angular deviation of the platform position from the intended position measured in the earth-fixed inertial frame while the disturbance is being applied.

For this goal, all four controllers are implemented in the real-time control computer.

Table 4.1: Table showing some properties and limits of the 6-DOF motion simulator used throughout the experiments

Platform height (contracted):	1.15m		
Platform base diameter:	2.4m		
Actuator course:	500mm		
Power consumption (average):	8kW		
MOTION LIMITS Motion	Position	Velocity	Acceleration
Surge	-0.46/0.36m	±0.60 m/s	±7.0 m/s^2
Sway	±0.37m	±0.60 m/s	±7.0 m/s^2
Heave	-0.30/0.35m	±0.56 m/s	±7.0 m/s^2
Roll	±19°	±30°/s	±140°/s^2
Pitch	±19°	±30°/s	±140°/s^2
Yaw	±21°	±30°/s	±140°/s^2

Note that the adjustment required for the controller gains while the simulation model controllers are implemented in the real system are very small which is another measure of how good the simulation model is. Five different disturbance profiles are applied to the base of the platform which is rigidly fixed onto the 6-DOF motion simulator. Since there are two uncoupled axes on the gimbal, two different disturbances are applied, one for each of them; yaw disturbance for the azimuth axis and pitch disturbance for the elevation axis. While giving both disturbances and stabilizing both axes at the same time is possible, each axis is tested separately to obtain more reliable and accurate results.

The five different disturbance profiles are given in Table 3.1 of Section 3.5. As one can see, they are sinusoidal disturbance profiles with known frequencies and amplitudes. The range of disturbance frequencies begins from 0.5 Hz and goes up to 10 Hz. With increasing frequencies the amplitude of the sine wave decreases. The main reason for this is the capabilities of the 6-DOF motion simulator used, as the frequency increase, the maximum amplitude of motion the simulator can create diminishes greatly. In

fact, the amplitudes of the five sinusoidal disturbance profiles that are going to be applied are dictated by the limits of the motion simulator.

The two disturbances that will be applied to the base of the platform are the two rotation disturbances mentioned above, the ones in yaw and pitch axes. Note that although the direction of a yaw motion for example, is known, the center of rotation for a rotational motion is also important. In our experiments, the rotational motions of the simulator are centered as close to the center of rotation of the corresponding axis of the gimbal as possible. This is done so that no translational motion is induced. Translational accelerations and decelerations of the platform will surely cause any unbalance of the mechanical system create a net torque on both axes, therefore adding another disturbance source. By intersecting the center of rotation of both the gimbal and the disturbance, we are able to isolate the gimbal from such effects as much as possible. In spite of these efforts, it will be seen in elevation axis tests that a small translational motion still exists in this axis. However the effect of this disturbance is not totally unwanted because as explained later it substitutes the very low friction torque disturbance for this axis that wouldn't otherwise be sufficient to test the disturbance rejection performance on this axis.

Before the start of any experiment, the analog sensors are monitored and any offsets in the signals are corrected. These offsets can be caused by temperature changes or even slight movements of the sensors even though they are rigidly mounted. Again, before any experiment is conducted, the mechanical parts and the mounting of the sensors are checked to avoid having loose connections that can effect the mechanical plant characteristics and therefore the overall experimental results. Finally, power supplies, electronics and cabling is checked to make sure any faults or misconnection are avoided.

At the beginning of each test run, the gimbal platform is brought to its zero angular position and stabilized there. Then, the motion simulator is engaged and disturbance is given. While being stabilized under the effect of the base disturbance, angular velocity readings from the gyroscopes mounted on the stabilized platform are logged for a long enough time period. After the experiment is conducted, the logged data is analyzed and results are calculated. The integral of angular velocity data collected

from gyros gives the deviation of the gimbal from its zero position under the given disturbance as a function of time. To come up with a number that reflects the stabilization performance, standard deviation of this time data over a 30 second period of time is taken for all experiments. This final value is denoted as the stabilization performance. Note that in a perfectly stabilized platform the gyroscopes should read zero since the angular position of the platform relative to earth fixed inertial frame is kept perfectly unchanged. However, since a perfect stabilization is not possible there always is some deviation and the amount of this deviation is a measure how good the platform is being stabilized, smaller the error better the stabilization performance.

Experiment runs are performed separately for the following two axes of the gimbal;

- Azimuth axis,
- Elevation axis.

Four different controllers designed in the previous chapters are tested. These different controllers can be listed as follows;

- The standard controller,
- Controller utilizing the disturbance observer method,
- Controller utilizing the inner acceleration loop method,
- Controller utilizing the state derivative feedback LQR method.

And these four controllers are tested under five different sinusoidal disturbance profiles covering a frequency range starting form 0.5 Hz and ending at 10 Hz. The amplitudes slightly differ for each axis and can be listed as follows;
For the azimuth axis;

- Frequency of 0.5Hz, peak-to-peak amplitude of 20°,
- Frequency of 1Hz, peak-to-peak amplitude of 9.5°,
- Frequency of 2Hz, peak-to-peak amplitude of 4°,

- Frequency of 5Hz, peak-to-peak amplitude of 0.65°,
- Frequency of 10Hz, peak-to-peak amplitude of 0.08°.

For the elevation axis;

- Frequency of 0.5Hz, peak-to-peak amplitude of 17°,
- Frequency of 1Hz, peak-to-peak amplitude of 8°,
- Frequency of 2Hz, peak-to-peak amplitude of 3.5°,
- Frequency of 5Hz, peak-to-peak amplitude of 0.6°,
- Frequency of 10Hz, peak-to-peak amplitude of 0.1°.

When all possible combinations are taken into consideration it is evident that 40 different experimental runs are needed in total. In the following section, the results of these 40 experiments will be presented.

4.3 Experimental Results

4.3.1 Azimuth Axis Tests

Four different controllers designed and tuned for the azimuth axis are tested under 5 different disturbances. In azimuth axis, the friction torques caused by the relative motion of the base and gimbal are the main disturbance torques whose effects are to be rejected by the controller for good performance. In agreement with various works and publications about the topic and simulation results presented in this report, all three methods utilizing acceleration feedback in control loops shoved improved performances when compared with the standard controller. Among the three controllers making use of acceleration feedback, state derivative feedback LQR has the overall best performance, slightly better than the controller with inner acceleration loop. The disturbance observer method results in the worst performance of this three although still performing much better than the standard controller. Performance improvements can be seen clearly from the resulting stabilization error plots given under each experiment's title.

4.3.1.1 The Standard Controller

The standard controller results in the biggest stabilization errors of all four controllers. This is only expected because the standard controller does not make use of the acceleration feedback as the other controllers do. However, it is important to note that even the stabilization accuracies achieved with this controller are quite impressive thanks to the superior mechanical properties of the gimbal platform and high quality sensors and actuators used.

When the plots for stabilization error are examined, it is relatively easy to spot points where stabilization error suddenly increases. These are the points where the disturbance from the motion simulator changes direction, causing a change in the direction of the friction torque as a result. This sudden change of direction causes a momentary big position error since it takes some time for the controller to react to this sudden change in disturbance. Later, the controller closes this error and keeps it near zero until a new change in disturbance direction is experienced. For higher frequency disturbances, the controller may not be able to bring the error down to zero before a new change in disturbance is experienced, which is also the case in the following plots for high frequency disturbances. At these high frequencies, the controller can only reject some portion of the disturbance and lower the amount of position error.

Frequency 0.5 Hz, Amplitude 20°; Standard deviation of a 30-second stabilization error data obtained by integrating the angular velocity signal is 0.046 mrad. In the following Figure 4.5, a 5-second stabilization error plot is given.

Frequency 1 Hz, Amplitude 9.5°; Standard deviation of a 30-second stabilization error data obtained by integrating the angular velocity signal is 0.062 mrad. In the following Figure 4.6, a 5-second stabilization error plot is given.

Frequency 2 Hz, Amplitude 4°; Standard deviation of a 30-second stabilization error data obtained by integrating the angular velocity signal is 0.073 mrad. In the following Figure 4.7, a 5-second stabilization error plot is given.

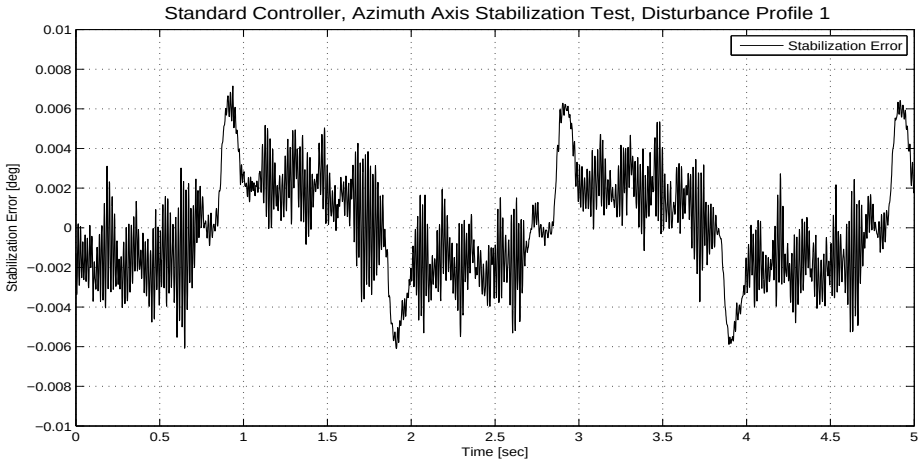

Figure 4.5: Azimuth Axis, Standard Controller, freq. 0.5 Hz, amp. 20°

Frequency 5 Hz, Amplitude 0.65°; Standard deviation of a 30-second stabilization error data obtained by integrating the angular velocity signal is 0.059 mrad. In the following Figure 4.8, a 5-second stabilization error plot is given.

Frequency 10 Hz, Amplitude 0.08°; Standard deviation of a 30-second stabilization error data obtained by integrating the angular velocity signal is 0.049 mrad. In the following Figure 4.9, a 5-second stabilization error plot is given.

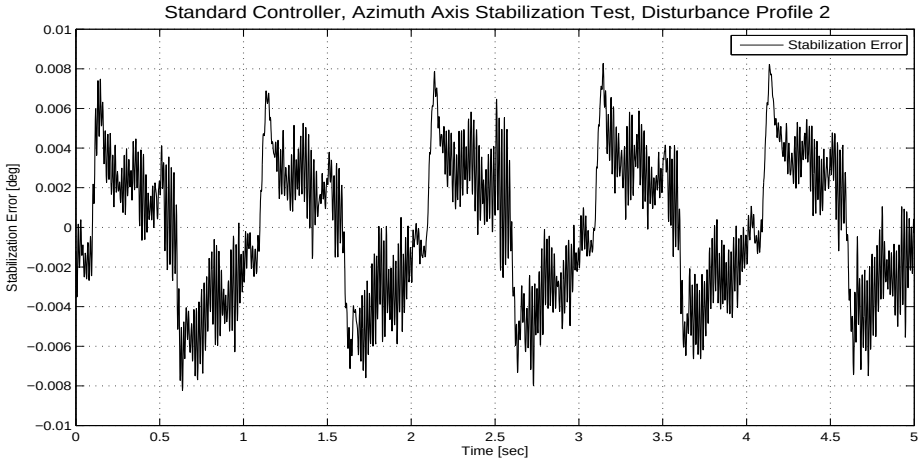

Figure 4.6: Azimuth Axis, Standard Controller, freq. 1 Hz, amp. 9.5°

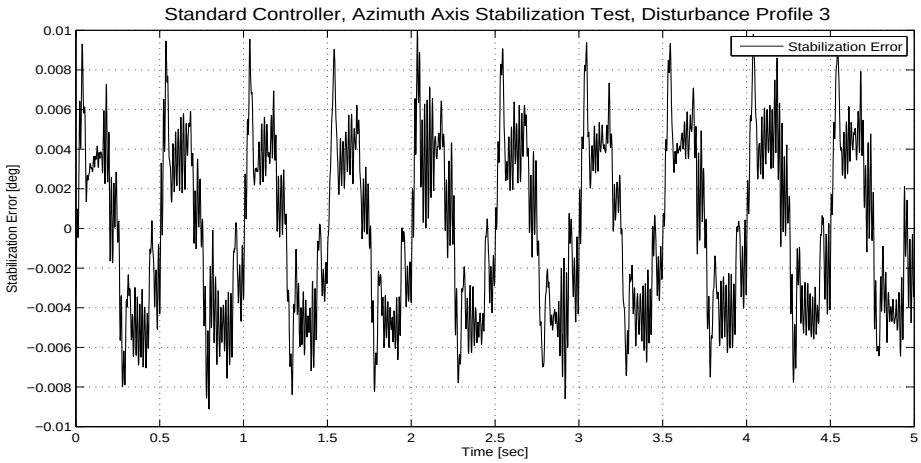

Figure 4.7: Azimuth Axis, Standard Controller, freq. 2 Hz, amp. 4°

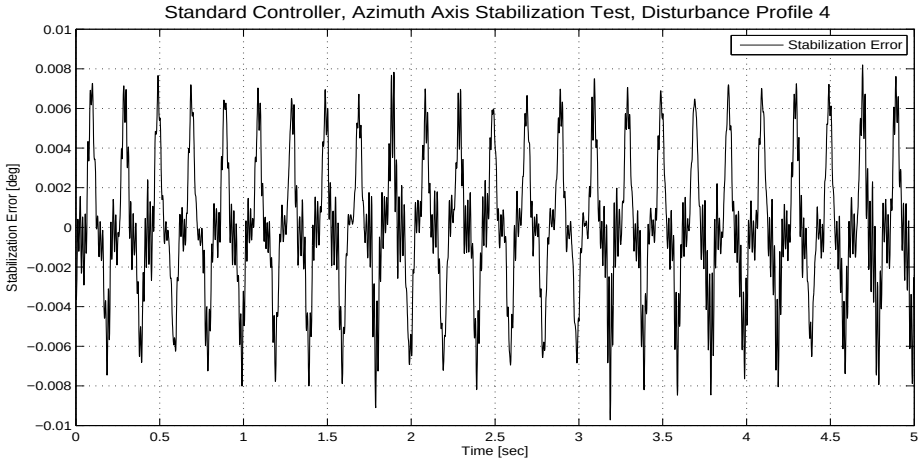

Figure 4.8: Azimuth Axis, Standard Controller, freq. 5 Hz, amp. 0.65°

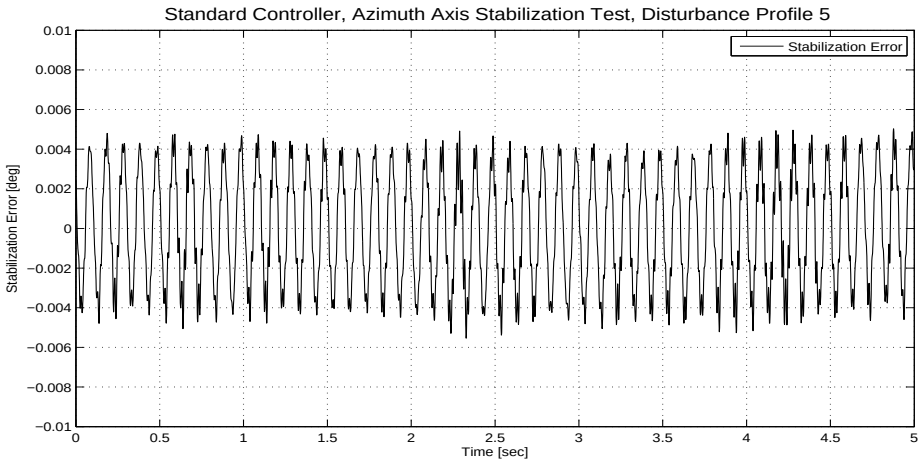

Figure 4.9: Azimuth Axis, Standard Controller, freq. 10 Hz, amp. 0.08°

4.3.1.2 Controller with Load Torque Estimator

The controller with load torque estimator is good at improving stabilization performance as it is expected. An overall decrease in errors for all frequencies is evident from figures. However, once again note that the filtering of calculated disturbance signal to remove the noise content limits the performance of this method. Better performances can be achieved with higher filter bandwidths, however this is possible at the cost of increased noise amplification and vibration of the platform.

In Figure 4.10 below, disturbance torque predicted and fed forward by the disturbance observer is given as a function of time together with the stabilization error signal for a 0.5 Hz disturbance profile. When compared with the friction plot belonging to azimuth axis of the gimbal given in Figure 3.4 of Section 3.1.3.1, one can see that disturbance observer can predict the disturbance value quite accurately, only with a delay which is the result of the filter used.

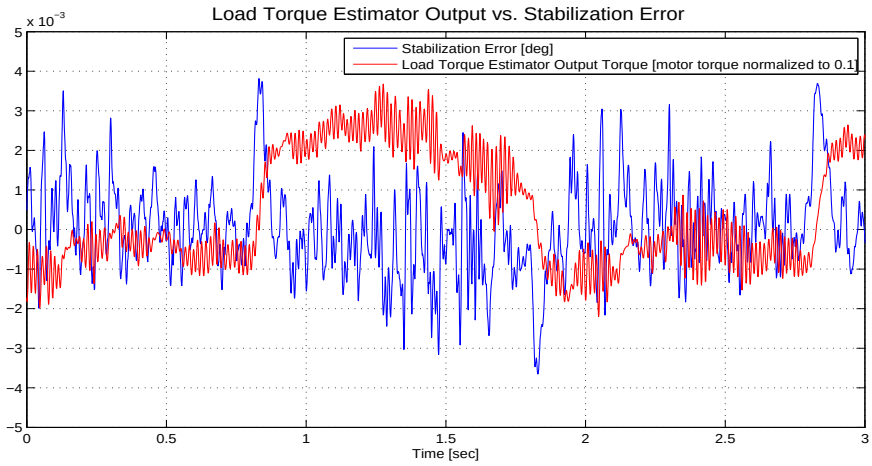

Figure 4.10: Disturbance Torque Predicted by the Load Torque Estimator of Azimuth Axis

Frequency 0.5 Hz, Amplitude 20°; Standard deviation of a 30-second stabilization error data obtained by integrating the angular velocity signal is 0.021 mrad. In the following Figure 4.11, a 5-second stabilization error plot is given.

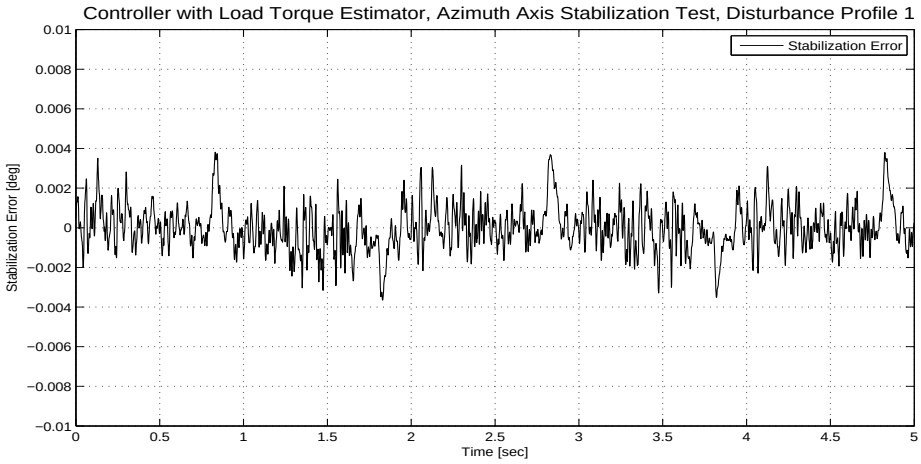

Figure 4.11: Azimuth Axis, Controller with Load Torque Estimator, freq. 0.5 Hz, amp. 20°

Frequency 1 Hz, Amplitude 9.5°; Standard deviation of a 30-second stabilization error data obtained by integrating the angular velocity signal is 0.027 mrad. In the following Figure 4.12, a 5-second stabilization error plot is given.

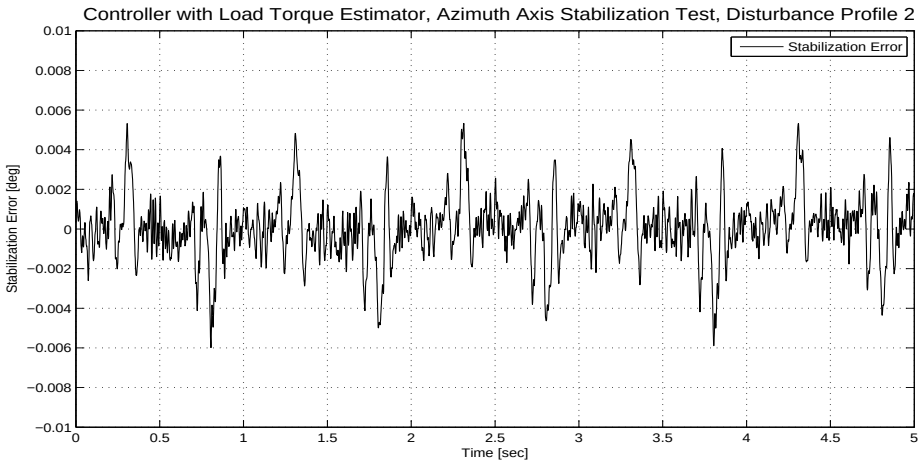

Figure 4.12: Azimuth Axis, Controller with Load Torque Estimator, freq. 1 Hz, amp. 9.5°

Frequency 2 Hz, Amplitude 4°; Standard deviation of a 30-second stabilization error data obtained by integrating the angular velocity signal is 0.035 mrad. In the following Figure 4.13, a 5-second stabilization error plot is given.

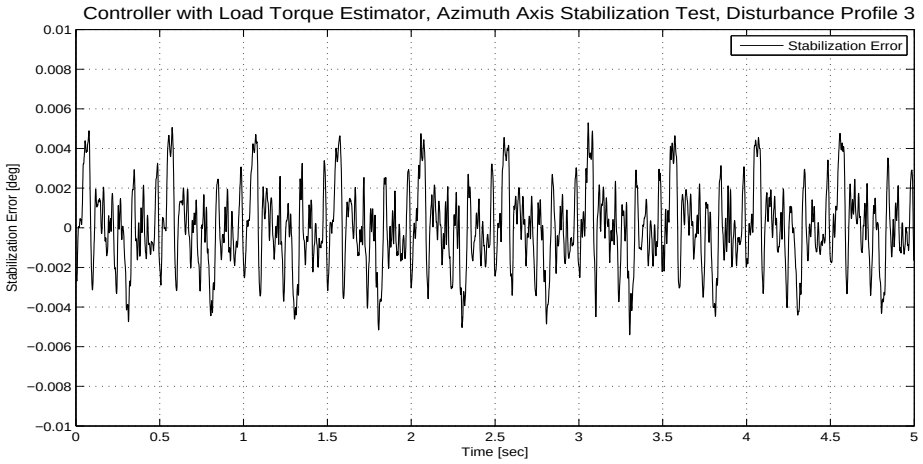

Figure 4.13: Azimuth Axis, Controller with Load Torque Estimator, freq. 2 Hz, amp. 4°

Frequency 5 Hz, Amplitude 0.65°; Standard deviation of a 30-second stabilization error data obtained by integrating the angular velocity signal is 0.035 mrad. In the following Figure 4.14, a 5-second stabilization error plot is given.

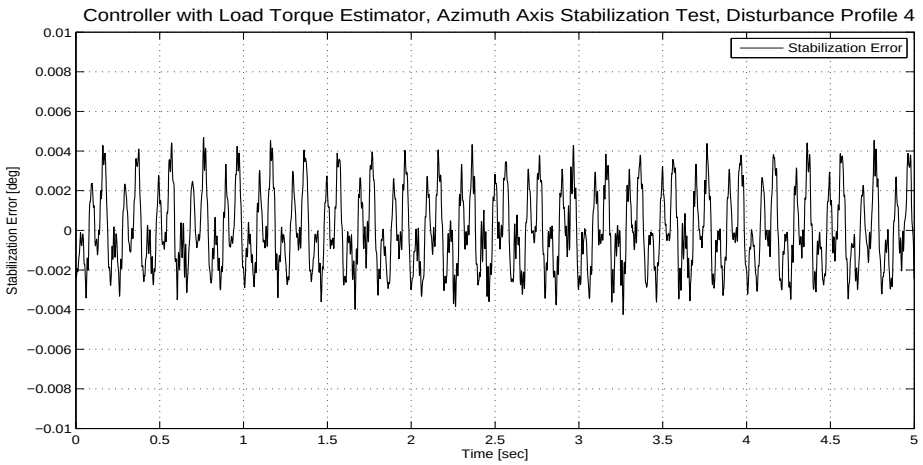

Figure 4.14: Azimuth Axis, Controller with Load Torque Estimator, freq. 5 Hz, amp. 0.65°

Frequency 10 Hz, Amplitude 0.08°; Standard deviation of a 30-second stabilization error data obtained by integrating the angular velocity signal is 0.038 mrad. In

the following Figure 4.15, a 5-second stabilization error plot is given.

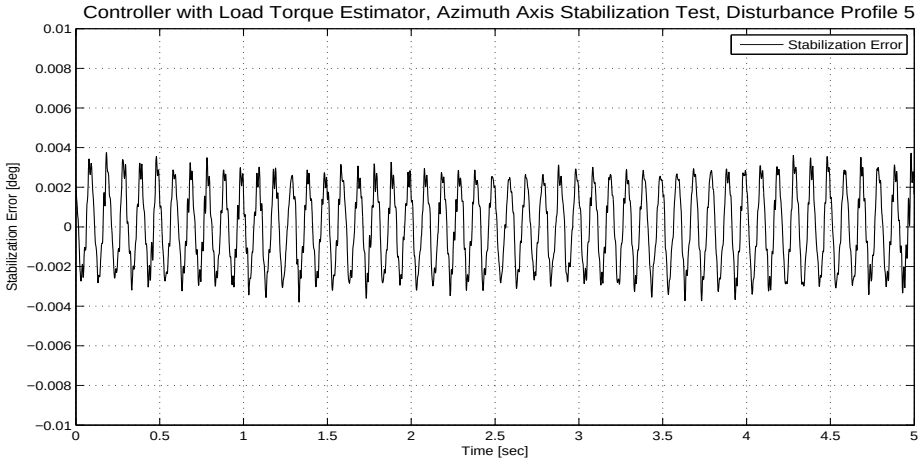

Figure 4.15: Azimuth Axis, Controller with Load Torque Estimator, freq. 10 Hz, amp. 0.08°

4.3.1.3 Controller with Inner Acceleration Loop

Controller with inner acceleration loop shows greatly improved performance when compared with the previous two results. It can be seen from all five plots below that stabilization errors are reduced drastically. Error peaks accurring at disturbance direction changing points are effectively minimized. As already mentioned in previous chapters, this improvement is the result of the faster inner acceleration loop detecting the acceleration error and trying to close it before the acceleration error accumulates and velocity loops can react to this accumulated error.

Frequency 0.5 Hz, Amplitude 20°; Standard deviation of a 30-second stabilization error data obtained by integrating the angular velocity signal is 0.017 mrad. In the following Figure 4.16, a 5-second stabilization error plot is given.

Frequency 1 Hz, Amplitude 9.5°; Standard deviation of a 30-second stabilization error data obtained by integrating the angular velocity signal is 0.023 mrad. In the following Figure 4.17, a 5-second stabilization error plot is given.

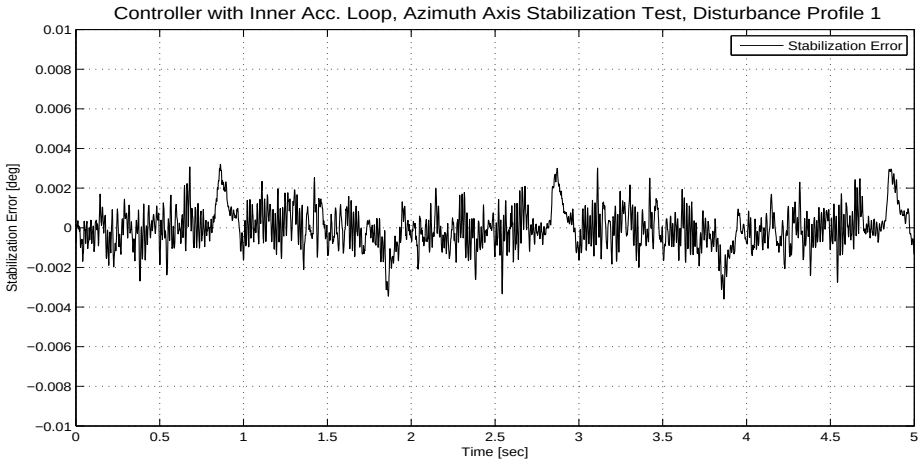

Figure 4.16: Azimuth Axis, Controller with Inner Acc. Loop, freq. 0.5 Hz, amp. 20°

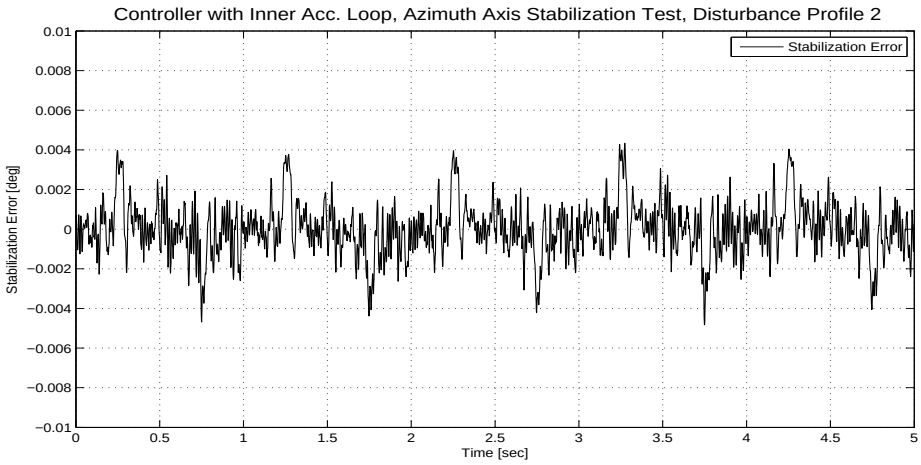

Figure 4.17: Azimuth Axis, Controller with Inner Acc. Loop, freq. 1 Hz, amp. 9.5°

Frequency 2 Hz, Amplitude 4°; Standard deviation of a 30-second stabilization error data obtained by integrating the angular velocity signal is 0.025 mrad. In the following Figure 4.18, a 5-second stabilization error plot is given.

Frequency 5 Hz, Amplitude 0.65°; Standard deviation of a 30-second stabilization error data obtained by integrating the angular velocity signal is 0.026 mrad. In the

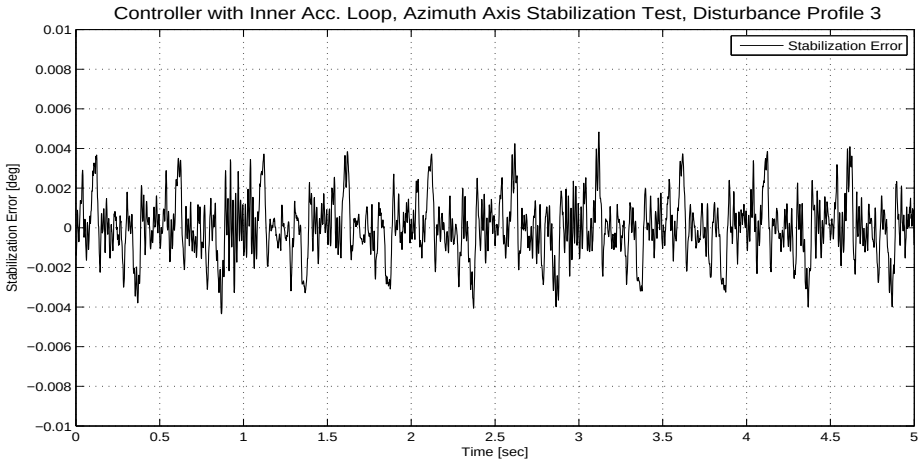

Figure 4.18: Azimuth Axis, Controller with Inner Acc. Loop, freq. 2 Hz, amp. 4°

following Figure 4.19, a 5-second stabilization error plot is given.

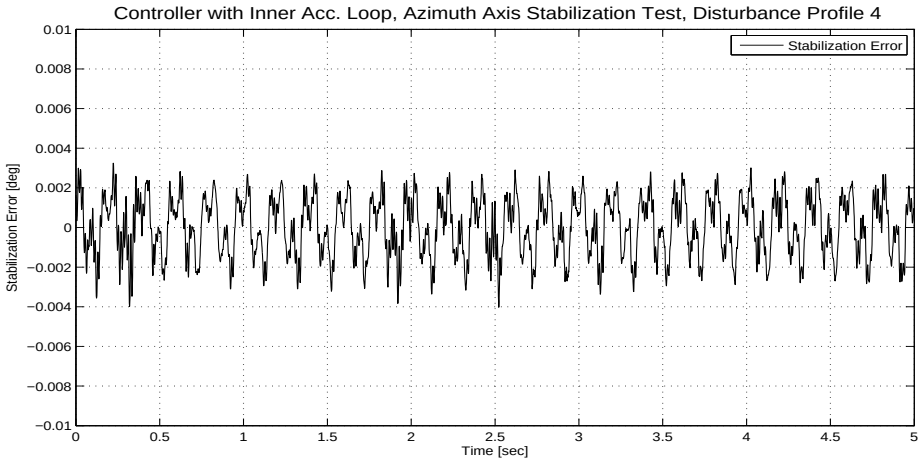

Figure 4.19: Azimuth Axis, Controller with Inner Acc. Loop, freq. 5 Hz, amp. 0.65°

Frequency 10 Hz, Amplitude 0.08°; Standard deviation of a 30-second stabilization error data obtained by integrating the angular velocity signal is 0.027 mrad. In the following Figure 4.20, a 5-second stabilization error plot is given.

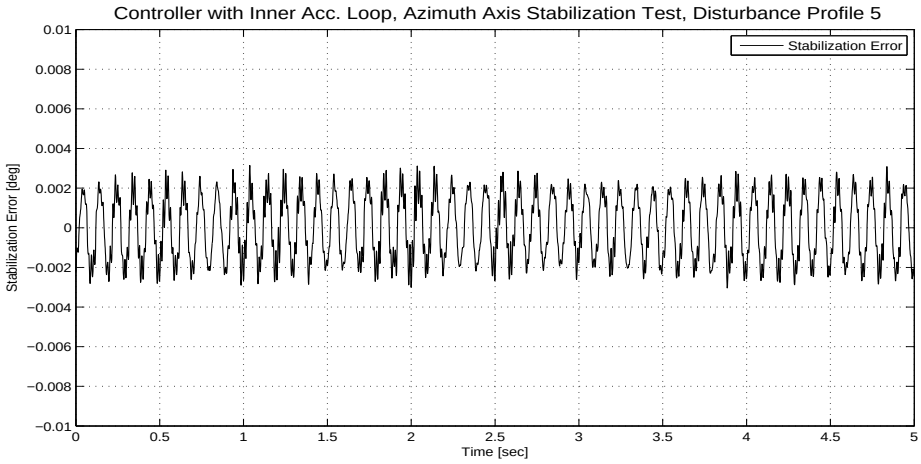

Figure 4.20: Azimuth Axis, Controller with Inner Acc. Loop, freq. 10 Hz, amp. 0.08°

4.3.1.4 State Derivative Feedback LQR Controller

State derivative feedback LQR shows the best performance of all four controllers. This can be seen from both the time plots of stabilization error and from the standard deviation numbers obtained. Error peaks resulting from change of direction of applied disturbance are almost unnoticeable in the time plots. However it is important to note that this controller results in slightly higher noise and vibration when compared to the other controllers, which can also be seen from the time plots below.

Frequency 0.5 Hz, Amplitude 20°; Standard deviation of a 30-second stabilization error data obtained by integrating the angular velocity signal is 0.019 mrad. In the following Figure 4.21, a 5-second stabilization error plot is given.

Frequency 1 Hz, Amplitude 9.5°; Standard deviation of a 30-second stabilization error data obtained by integrating the angular velocity signal is 0.019 mrad. In the following Figure 4.22, a 5-second stabilization error plot is given.

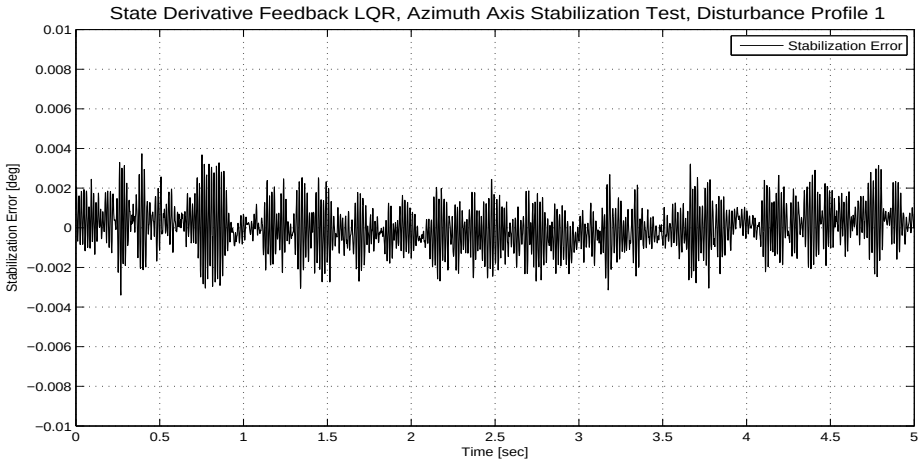

Figure 4.21: Azimuth Axis, State Derivative Feedback LQR, freq. 0.5 Hz, amp. 20°

Frequency 2 Hz, Amplitude 4°; Standard deviation of a 30-second stabilization error data obtained by integrating the angular velocity signal is 0.020 mrad. In the following Figure 4.23, a 5-second stabilization error plot is given.

Frequency 5 Hz, Amplitude 0.65°; Standard deviation of a 30-second stabilization error data obtained by integrating the angular velocity signal is 0.017 mrad. In the following Figure 4.24, a 5-second stabilization error plot is given.

Frequency 10 Hz, Amplitude 0.08°; Standard deviation of a 30-second stabilization error data obtained by integrating the angular velocity signal is 0.017 mrad. In the following Figure 4.25, a 5-second stabilization error plot is given.

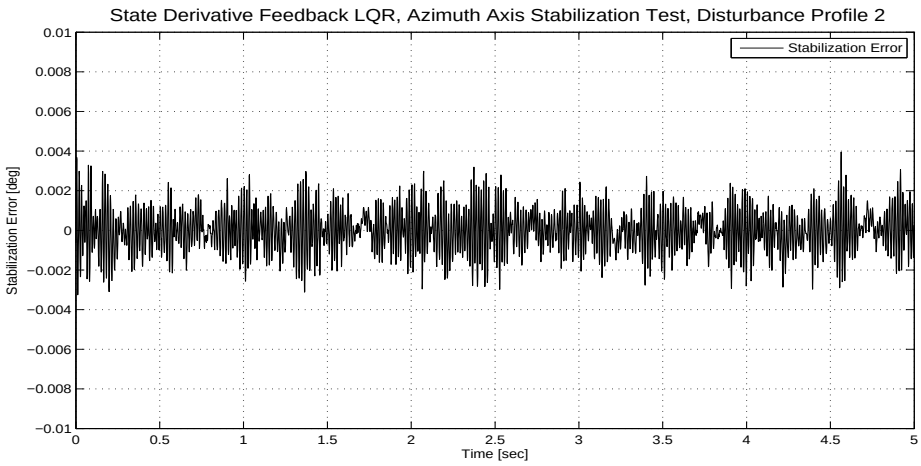

Figure 4.22: Azimuth Axis, State Derivative Feedback LQR, freq. 1 Hz, amp. 9.5°

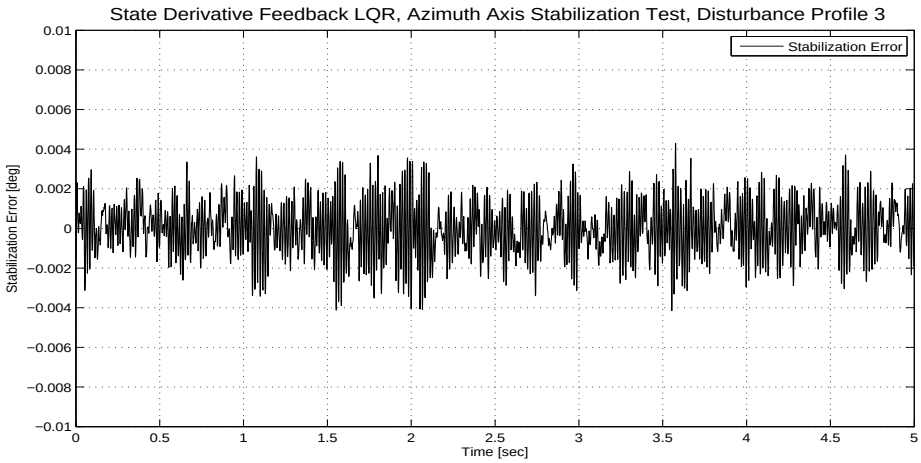

Figure 4.23: Azimuth Axis, State Derivative Feedback LQR, freq. 2 Hz, amp. 4°

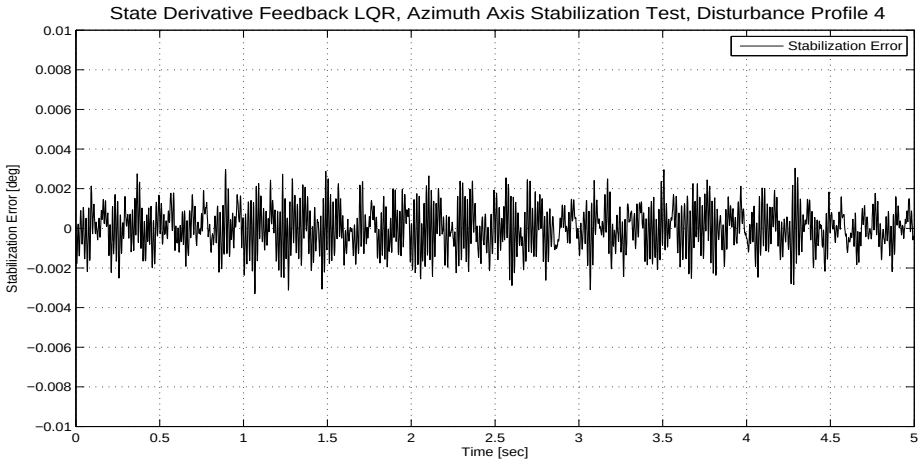

Figure 4.24: Azimuth Axis, State Derivative Feedback LQR, freq. 5 Hz, amp. 0.65°

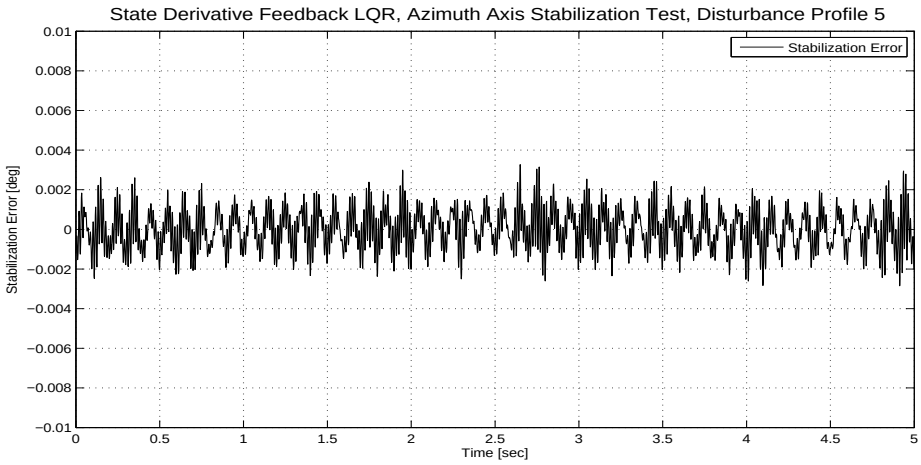

Figure 4.25: Azimuth Axis, State Derivative Feedback LQR, freq. 10 Hz, amp. 0.08°

4.3.2 Elevation Axis Tests

Once again four different controllers this time designed and tuned for the elevation axis are tested under five different disturbances. However, since friction value for elevation axis is extremely low (less than 10% of the already low friction toruqe of the azimuth axis), the effect of friction as a source of disturbance is insignificant. However, stabilization error plots show that another disturbance, this time a sinusoidal torque acts on elevation axis and causes errors. The source of this disturbance is the small translational accelerations in surge axis given to the base of the platform while the pitch motion is simulated. This effect is due to center of rotation of the platform motion not being exactly coincident with the center of rotation of gimbal elevation axis. This accelerations in turn result in a net torque acting on elevation axis since the COG of this axis is located above the center of rotation, meaning that accelerations in surge direction will result in dynamic unbalance torques, as it is the case in following experiments.

In agreement with the previous results, all three methods utilizing acceleration feedback in control loops showed improved performances when compared to the standard controller. Again, among the three controllers making use of acceleration feedback, state derivative feedback LQR has the overall best performance, slightly better than the controller with inner acceleration loop. The disturbance observer method results in the poorest performance of these three although still performing much better than the standard controller. Performance improvements can be seen clearly from the resulting stabilization error plots and standard deviation figures given under each experiment's title.

4.3.2.1 The Standard Controller

The standard controller results in the biggest stabilization errors of all four controllers as expected. This is only expected because the standard controller does not make use of acceleration feedback as the other controllers do. However, it is important to note that even the stabilization accuracies obtained with this controller are quite impressive thanks to the superior mechanical properties of the gimbal platform and high quality

sensors and actuators used.

Different from the azimuth stabilization error plots, when the plots for elevation axis are examined, sinusoidal variations in the error are seen as a result of the sinusoidal surge disturbance which is discussed above. Frequency of these variations are the same as the disturbance frequency of the test. Note that a sinusoidal change in disturbance torque is extremely hard to totally reject due to its continuously changing nature.

Frequency 0.5 Hz, Amplitude 17°; Standard deviation of a 30-second stabilization error data obtained by integrating the angular velocity signal is 0.045 mrad. In the following Figure 4.26, a 5-second stabilization error plot is given.

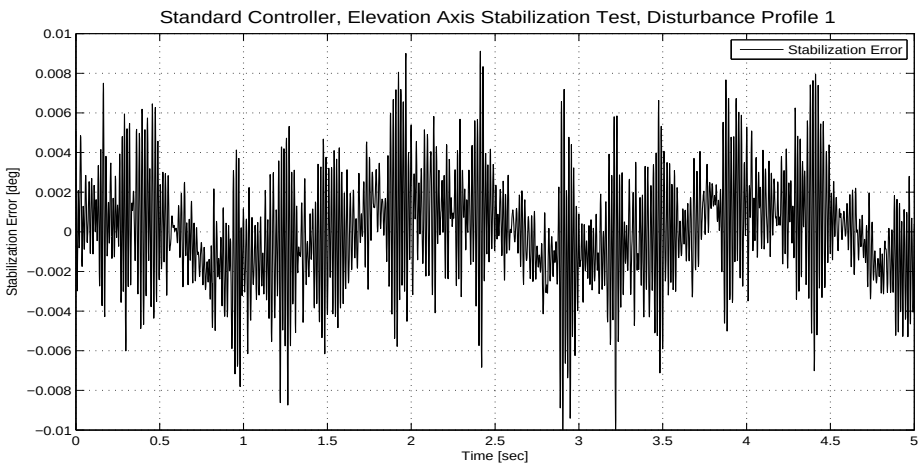

Figure 4.26: Elevation Axis, Standard Controller, freq. 0.5 Hz, amp. 17°

Frequency 1 Hz, Amplitude 8°; Standard deviation of a 30-second stabilization error data obtained by integrating the angular velocity signal is 0.050 mrad. In the following Figure 4.27, a 5-second stabilization error plot is given.

Frequency 2 Hz, Amplitude 3.5°; Standard deviation of a 30-second stabilization error data obtained by integrating the angular velocity signal is 0.064 mrad. In the

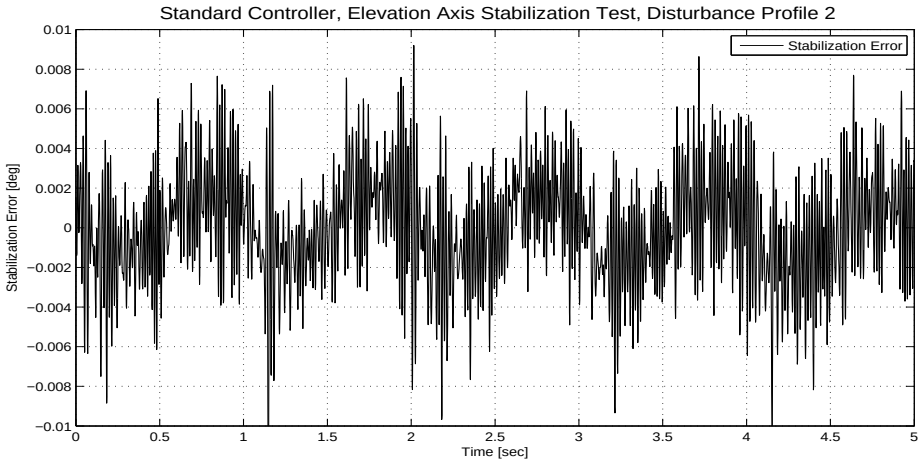

Figure 4.27: Elevation Axis, Standard Controller, freq. 1 Hz, amp. 8°

following Figure 4.28, a 5-second stabilization error plot is given.

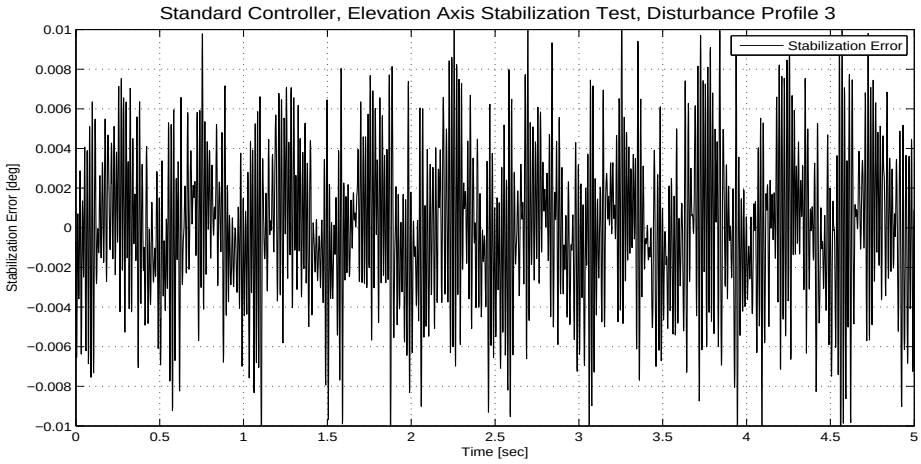

Figure 4.28: Elevation Axis, Standard Controller, freq. 2 Hz, amp. 3.5°

Frequency 5 Hz, Amplitude 0.6°; Standard deviation of a 30-second stabilization error data obtained by integrating the angular velocity signal is 0.045 mrad. In the following Figure 4.29, a 5-second stabilization error plot is given.

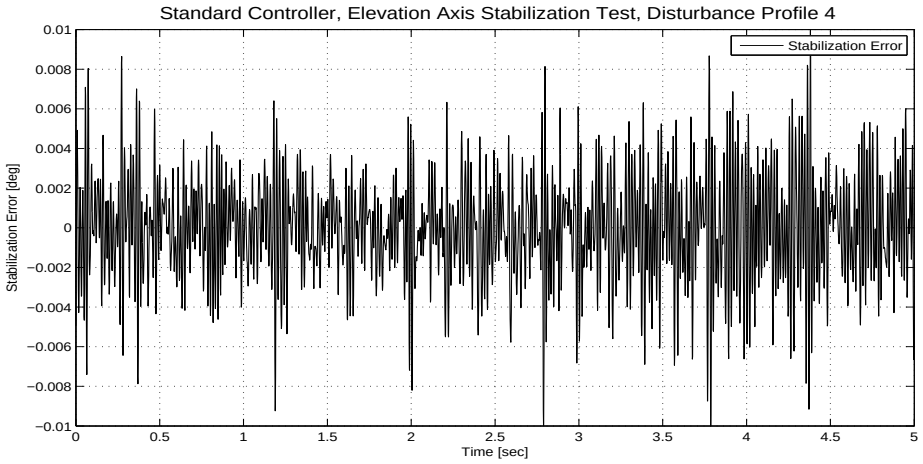

Figure 4.29: Elevation Axis, Standard Controller, freq. 5 Hz, amp. 0.6°

Frequency 10 Hz, Amplitude 0.1°; Standard deviation of a 30-second stabilization error data obtained by integrating the angular velocity signal is 0.041 mrad. In the following Figure 4.30, a 5-second stabilization error plot is given.

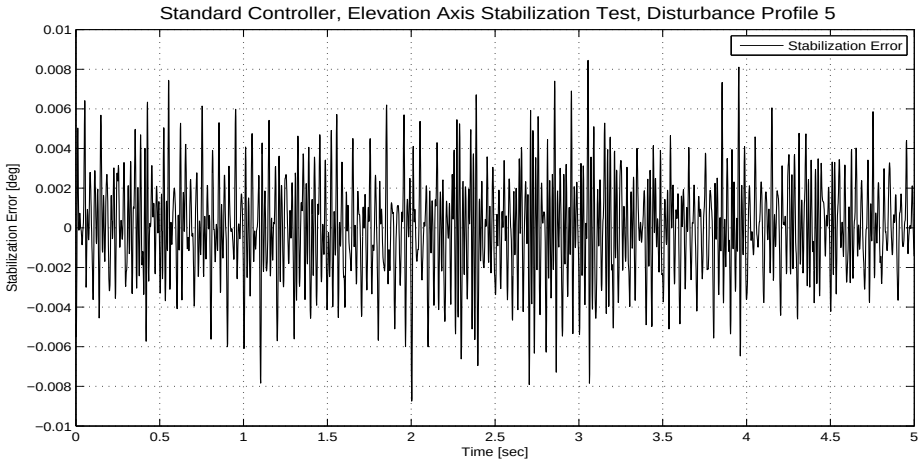

Figure 4.30: Elevation Axis, Standard Controller, freq. 10 Hz, amp. 0.1°

4.3.2.2 Controller with Load Torque Estimator

The controller with load torque estimator is good at improving stabilization performance just as it did in azimuth axis. An overall decrease in errors for all frequencies is evident from figures presented. However, as stated earlier, the filtering of calculated disturbance signal to remove noise limits the performance of this method. Better performances can be achieved with higher filter bandwidths, however this is possible at the cost of increased noise amplification and induced vibrations of the platform.

In the Figure 4.31 below, disturbance torque predicted and fed forward by the disturbance observer is given as a function of time together with the stabilization error signal for a 0.5 Hz disturbance profile. One can see that disturbance observer can predict the disturbance value quite accurately when the sinusoidal disturbance torque acting on the elevation axis as a result of translational accelerations is considered. A delay in the signal is possible though, which is the result of the filter used.

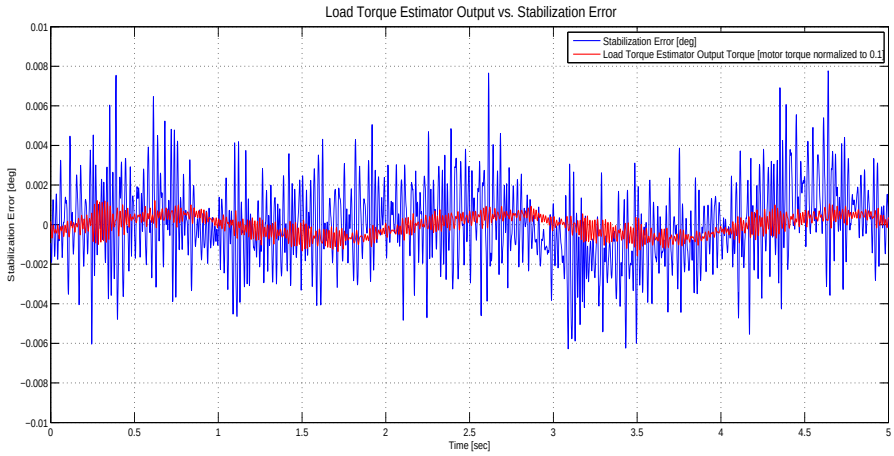

Figure 4.31: Disturbance Torque Predicted by the Load Torque Estimator of Elevation Axis

Frequency 0.5 Hz, Amplitude 17°; Standard deviation of a 30-second stabilization error data obtained by integrating the angular velocity signal is 0.034 mrad. In the following Figure 4.32, a 5-second stabilization error plot is given.

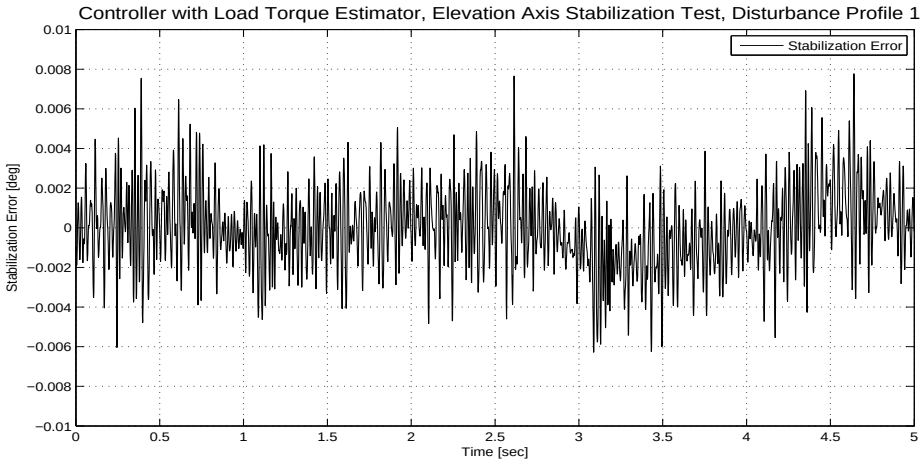

Figure 4.32: Elevation Axis, Controller with Load Torque Estimator, freq. 0.5 Hz, amp. 17°

Frequency 1 Hz, Amplitude 8°; Standard deviation of a 30-second stabilization error data obtained by integrating the angular velocity signal is 0.039 mrad. In the following Figure 4.33, a 5-second stabilization error plot is given.

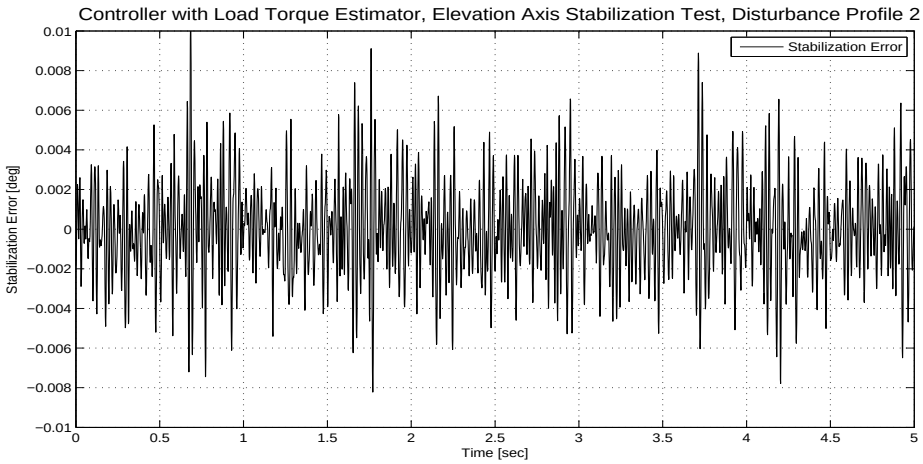

Figure 4.33: Elevation Axis, Controller with Load Torque Estimator, freq. 1 Hz, amp. 8°

Frequency 2 Hz, Amplitude 3.5°; Standard deviation of a 30-second stabilization error data obtained by integrating the angular velocity signal is 0.043 mrad. In the following Figure 4.34, a 5-second stabilization error plot is given.

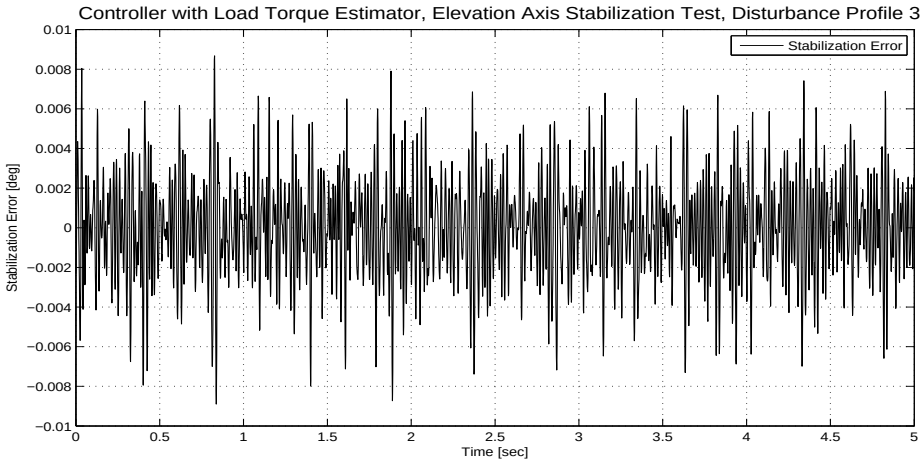

Figure 4.34: Elevation Axis, Controller with Load Torque Estimator, freq. 2 Hz, amp. 3.5°

Frequency 5 Hz, Amplitude 0.6°; Standard deviation of a 30-second stabilization error data obtained by integrating the angular velocity signal is 0.037 mrad. In the following Figure 4.35, a 5-second stabilization error plot is given.

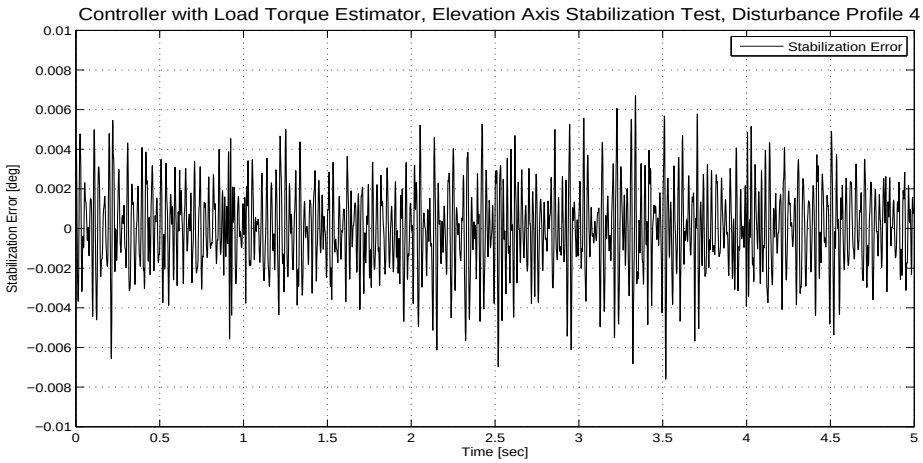

Figure 4.35: Elevation Axis, Controller with Load Torque Estimator, freq. 5 Hz, amp. 0.6°

Frequency 10 Hz, Amplitude 0.1°; Standard deviation of a 30-second stabilization error data obtained by integrating the angular velocity signal is 0.025 mrad. In the

following Figure 4.36, a 5-second stabilization error plot is given.

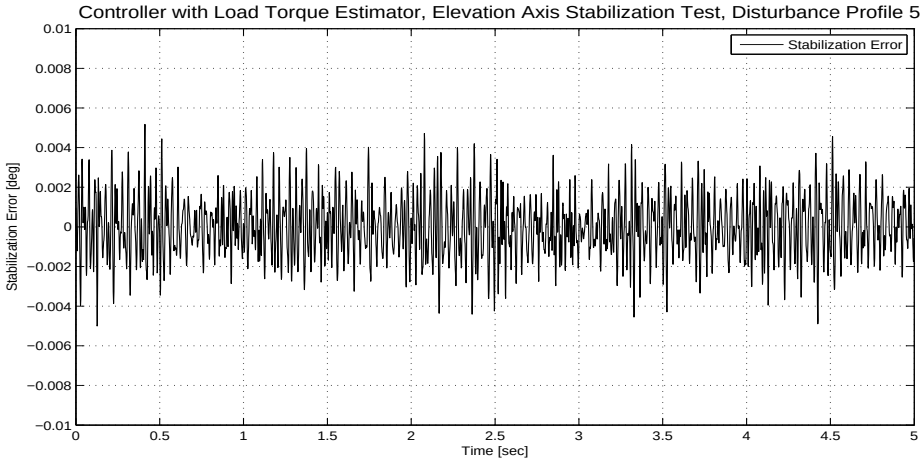

Figure 4.36: Elevation Axis, Controller with Load Torque Estimator, freq. 10 Hz, amp. 0.1°

4.3.2.3 Controller with Inner Acceleration Loop

Controller with inner acceleration loop shows greatly improved performance when compared to the previous two results. It can be seen from all five plots below that stabilization errors are reduced drastically. Amplitude of the sinusoidal variations in the error signal is effectively reduced. Note that the amount of noise is also lower when compared to the last two controllers as an additional benefit. As already mentioned, this improvement is the result of the faster inner acceleration loop detecting the acceleration error and trying to close it before the acceleration error accumulates and velocity loops can react to this accumulated error.

Frequency 0.5 Hz, Amplitude 17°; Standard deviation of a 30-second stabilization error data obtained by integrating the angular velocity signal is 0.016 mrad. In the following Figure 4.37, a 5-second stabilization error plot is given.

Frequency 1 Hz, Amplitude 8°; Standard deviation of a 30-second stabilization error data obtained by integrating the angular velocity signal is 0.021 mrad. In the

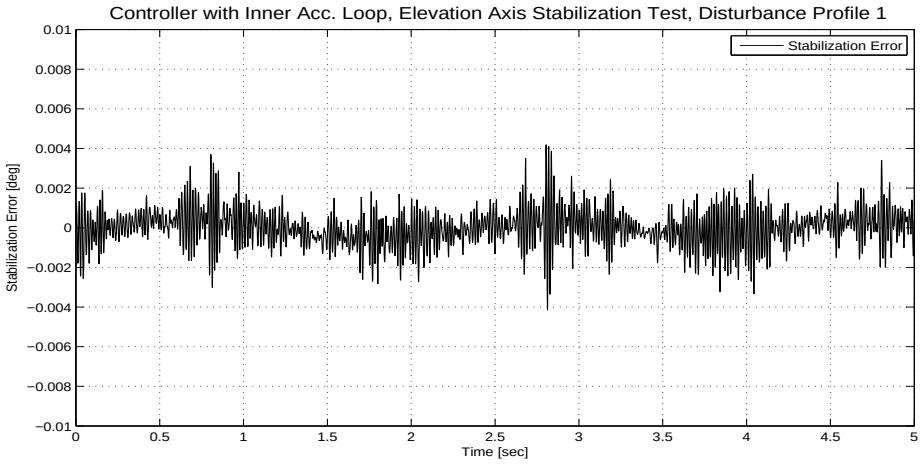

Figure 4.37: Elevation Axis, Controller with Inner Acc. Loop, freq. 0.5 Hz, amp. 17°

following Figure 4.38, a 5-second stabilization error plot is given.

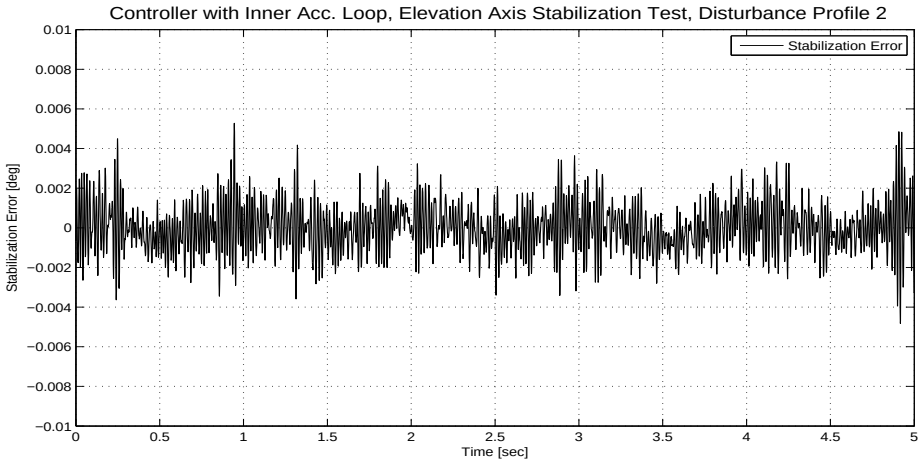

Figure 4.38: Elevation Axis, Controller with Inner Acc. Loop, freq. 1 Hz, amp. 8°

Frequency 2 Hz, Amplitude 3.5°; Standard deviation of a 30-second stabilization error data obtained by integrating the angular velocity signal is 0.025 mrad. In the following Figure 4.39, a 5-second stabilization error plot is given.

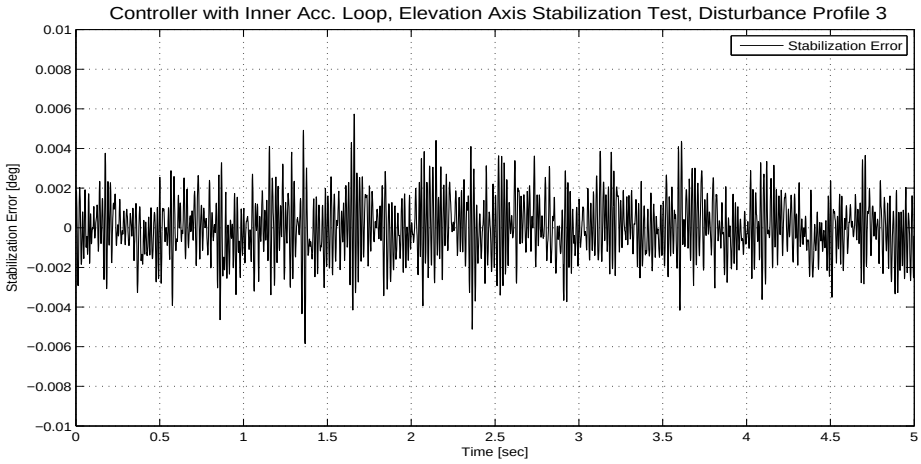

Figure 4.39: Elevation Axis, Controller with Inner Acc. Loop, freq. 2 Hz, amp. 3.5°

Frequency 5 Hz, Amplitude 0.6°; Standard deviation of a 30-second stabilization error data obtained by integrating the angular velocity signal is 0.023 mrad. In the following Figure 4.40, a 5-second stabilization error plot is given.

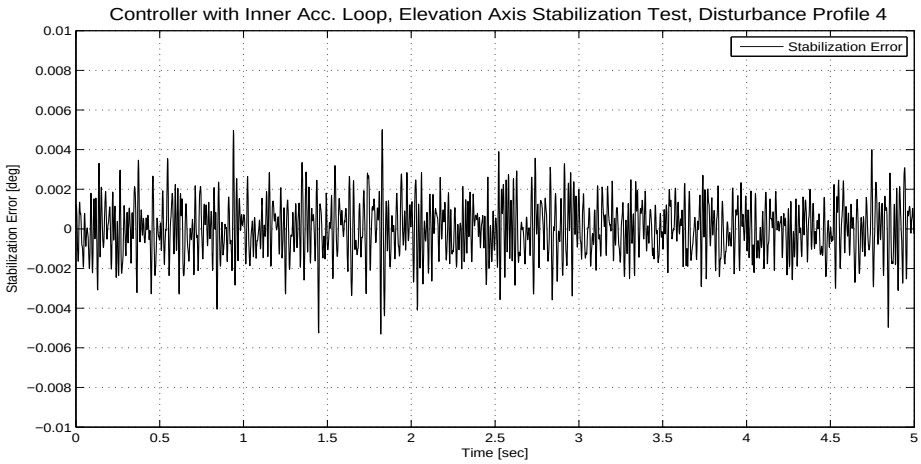

Figure 4.40: Elevation Axis, Controller with Inner Acc. Loop, freq. 5 Hz, amp. 0.6°

Frequency 10 Hz, Amplitude 0.1°; Standard deviation of a 30-second stabilization error data obtained by integrating the angular velocity signal is 0.018 mrad. In the following Figure 4.41, a 5-second stabilization error plot is given.

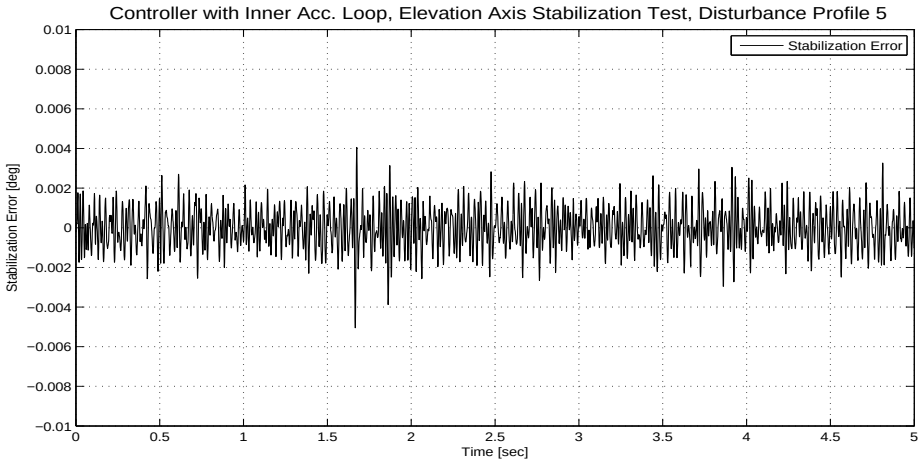

Figure 4.41: Elevation Axis, Controller with Inner Acc. Loop, freq. 10 Hz, amp. 0.1°

4.3.2.4 State Derivative Feedback LQR Controller

Again, state derivative feedback LQR shows the best performance of all controllers. Time plots of stabilization error and standard deviation numbers obtained shows this clearly. The noise levels are somehow bigger when compared to the inner acceleration loop method however still much better than the standard controller.

Frequency 0.5 Hz, Amplitude 17°; Standard deviation of a 30-second stabilization error data obtained by integrating the angular velocity signal is 0.017 mrad. In the following Figure 4.42, a 5-second stabilization error plot is given.

Frequency 1 Hz, Amplitude 8°; Standard deviation of a 30-second stabilization error data obtained by integrating the angular velocity signal is 0.016 mrad. In the following Figure 4.43, a 5-second stabilization error plot is given.

Frequency 2 Hz, Amplitude 3.5°; Standard deviation of a 30-second stabilization error data obtained by integrating the angular velocity signal is 0.021 mrad. In the following Figure 4.44, a 5-second stabilization error plot is given.

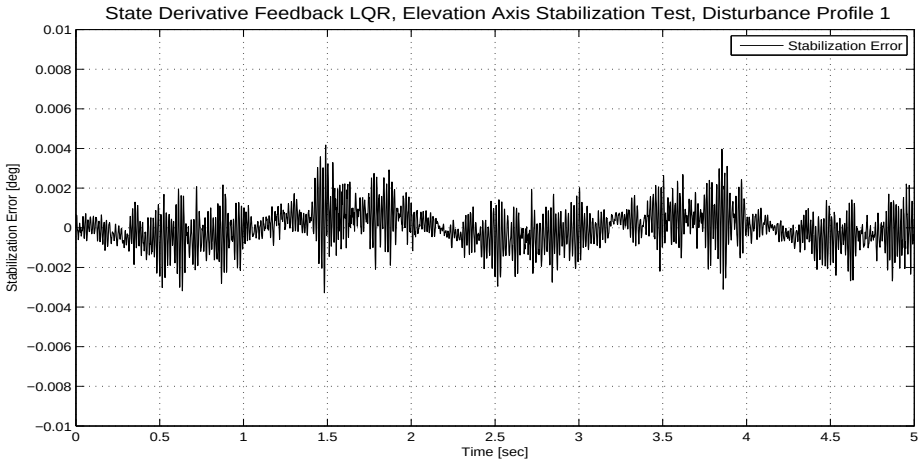

Figure 4.42: Elevation Axis, State Derivative Feedback LQR, freq. 0.5 Hz, amp. 17°

Frequency 5 Hz, Amplitude 0.6°; Standard deviation of a 30-second stabilization error data obtained by integrating the angular velocity signal is 0.017 mrad. In the following Figure 4.45, a 5-second stabilization error plot is given.

Frequency 10 Hz, Amplitude 0.1°; Standard deviation of a 30-second stabilization error data obtained by integrating the angular velocity signal is 0.017 mrad. In the following Figure 4.46, a 5-second stabilization error plot is given.

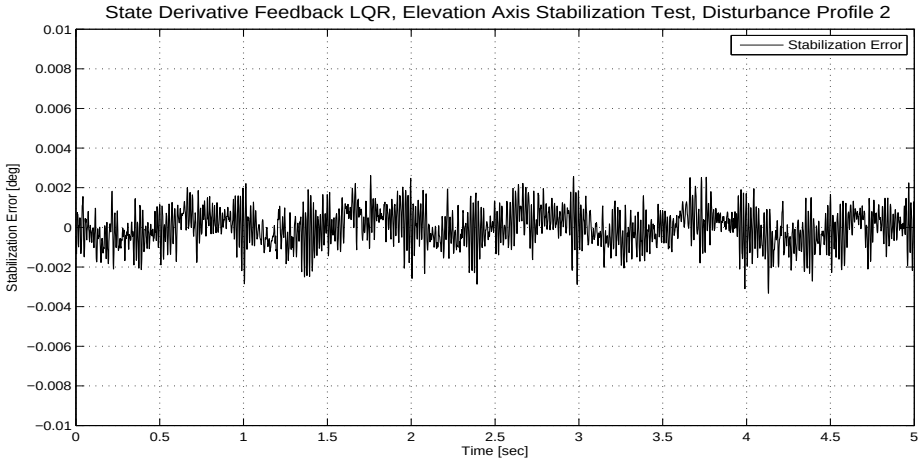

Figure 4.43: Elevation Axis, State Derivative Feedback LQR, freq. 1 Hz, amp. 8°

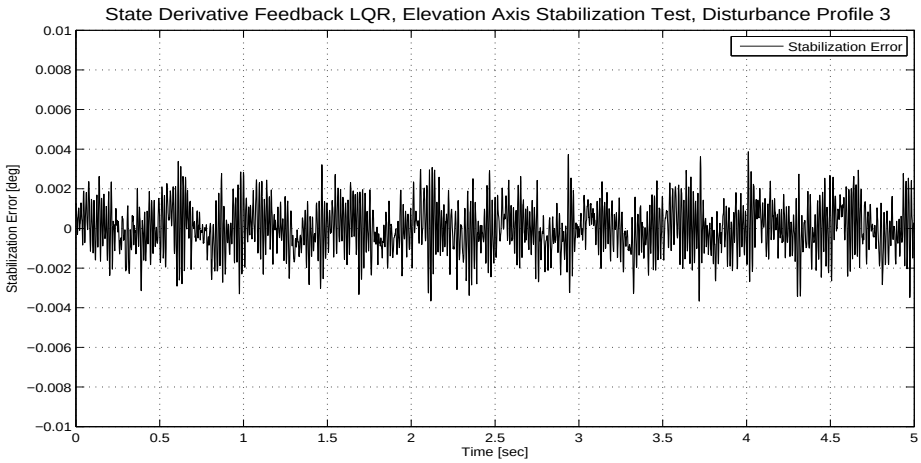

Figure 4.44: Elevation Axis, State Derivative Feedback LQR, freq. 2 Hz, amp. 3.5°

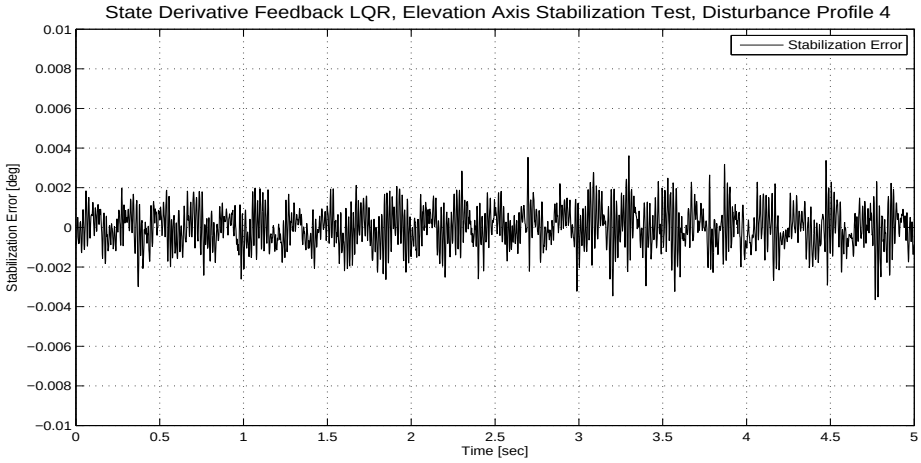

Figure 4.45: Elevation Axis, State Derivative Feedback LQR, freq. 5 Hz, amp. 0.6°

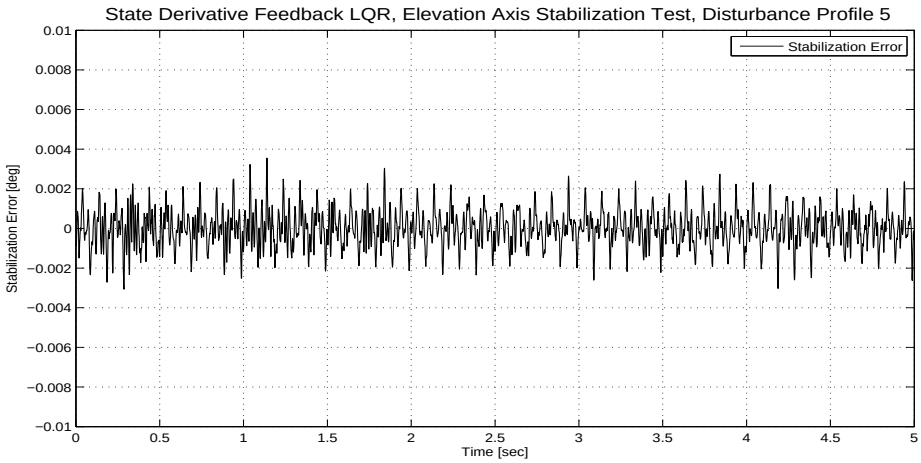

Figure 4.46: Elevation Axis, State Derivative Feedback LQR, freq. 10 Hz, amp. 0.1°

4.4 Conclusion

Below Table 4.2 summarizes obtained experimental results.

Table 4.2: Table showing the standard deviation stabilization errors achieved with all four controllers for both axes under different disturbances

AZIMUTH AXIS	0.5 Hz	1 Hz	2 Hz	5 Hz	10 Hz
Controller 1	46 μrad	62 μrad	73 μrad	59 μrad	49 μrad
Controller 2	21 μrad	27 μrad	35 μrad	35 μrad	38 μrad
Controller 3	17 μrad	23 μrad	25 μrad	26 μrad	27 μrad
Controller 4	19 μrad	19 μrad	20 μrad	17 μrad	17 μrad
ELEVATION AXIS	0.5 Hz	1 Hz	2 Hz	5 Hz	10 Hz
Controller 1	45 μrad	50 μrad	64 μrad	45 μrad	41 μrad
Controller 2	34 μrad	39 μrad	43 μrad	37 μrad	25 μrad
Controller 3	16 μrad	21 μrad	25 μrad	23 μrad	18 μrad
Controller 4	17 μrad	16 μrad	21 μrad	17 μrad	17 μrad

Looking at Table 4.2 and comparing it to the Table 3.2 of simulation test results, following additional observations can be made;

- Improvement due to the use of acceleration feedback in experimental tests is even more remarkable; fifty to seventy percent reduction in stabilization errors compared to the standard controller is achieved. Again the inner acceleration loop controller and the state derivative feedback LQR perform the best, followed by the load torque estimator.

- Experimental results obtained in the tests are very much similar to the results obtained in simulation runs in azimuth axis tests. On the other hand, some discrepancy exists in elevation axis tests which originates from undesired linear

accelerations given to the gimbal in experimental tests. Since the assumption that COG and center of rotation is coincident is not completely valid, this linear accelerations cause disturbance torques on the gimbal elevation axis that are not modeled in the simulation. The final result shows itself as higher stabilization errors in elevation axis in experimental tests.

- Contrary to the simulation results, higher frequency disturbances do not necessarily cause higher stabilization errors in experimental tests. It is considered to be due to stiction in the joints being fully effective when the disturbance frequencies are low and at higher frequencies the stiction phenomenon not happening fully, resulting in a smoother transition of disturbance torque from one direction to the other and lower stabilization errors being seen.

CHAPTER 5

DISCUSSION, CONCLUSION AND FUTURE WORK

The objective of this thesis has been stated as to apply several disturbance rejection algorithms which utilizes acceleration feedback to the platform stabilization problem in order to improve the overall stabilization performance. While this objective is being reached, several different problems have been tackled. This final chapter includes a discussion of these several problems that are addressed throughout the studies and tries to come to a conclusion. Possible future work that could not be covered in the scope of this thesis work is also presented in a separate section.

5.1 Discussion and Conclusion

As discussed in Chapter 1, stabilization can be considered as one of the two main tasks in the more general problem of servo control of a stabilized platform, the other being the positioning and tracking. For satisfactory performance of the whole system, both tasks should be executed successfully. This thesis work focuses on the task of stabilization and disturbance rejection, leaving the problem of positioning and tracking for later studies.

It is also stated in the same chapter that the main emphasis will be on the smaller and more agile platforms for the reason that methods developed results in very dynamic and high bandwidth controllers mainly realizable on these systems. Although methods developed should be applicable to bigger systems, they may cause saturation of the actuators and excessive loading in transmission and structural elements of these bigger platforms.

The platform that is going to be used in the experimental setup and therefore all work done is based on, is a 2-DOF gimbal platform with controllable azimuth and elevation axes. A detailed description of this 2-DOF gimbal is given in Section 4.1.1. One of the most important characteristics of this gimbal platform from servo control point of view is that both axes are driven with direct-drive motors with no transmission elements. Direct-drive systems have several advantages and therefore are widely used for such small and high performance applications. Among these advantages the absence of backlash and very high torsional stiffness between the motor and the driven load, and low friction, high efficiency characteristics achieved by the removal of transmission elements such as gearboxes can be considered as the most important. However, one drawback of such systems is that external forces and torques on the system result in bigger disturbances since removal of the gearbox also removes the resistance it provides against these disturbances. As a result, disturbance rejection algorithms become more important for direct-drive systems.

Disturbance rejection algorithms discussed in this thesis work belong to the important class of algorithms that utilize angular acceleration feedback in addition to the already available measurements of angular velocity or position. Having said that, the first problem that needs to be addressed becomes the construction of a high quality angular acceleration signal. In Section 2.1, it is explained that among different methods such as using angular accelerometers or differentiating the angular velocity signal, use of linear accelerometers for constructing the angular acceleration information is the best one when both performance and availability aspects are taken into account.

Section one of Chapter two deals with the details of angular acceleration calculation from linear accelerometer measurements. It is shown that 4 triaxial accelerometers placed as described in this section is sufficient for identifying the angular accelerations in all three directions. In fact, the array of linear accelerometers can be packed as a single sensor unit and mounted on any platform of which the angular acceleration vector is to be measured. One point that is of importance while putting together such a unit is that, the spacing between the accelerometers define the range of angular accelerations that can be measured and the amount of noise output. While closely placed accelerometers will result in a higher measurement range, sensors placed far apart will give a smaller amount of output noise. However, one should note that linear

accelerations measured by any of these linear accelerometers should not hit the maximum range the accelerometer can measure, otherwise wrong angular acceleration values will be calculated. Therefore, selection of the linear accelerometers and their placement on the system should be done so that saturation of sensors does no occur in operation.

An important assumption is done while angular acceleration of the platform is being calculated from linear accelerometer measurements; it is assumed that the body on which accelerometers are mounted is a rigid body, which is not going to hold true if the sensors are mounted on parts that can move relative to each other or a single body that is not rigid enough and deflect under working loads and motions. Both conditions should be avoided for correct calculation of angular accelerations.

Once the angular acceleration signals are obtained, both angular velocities and angular accelerations of the platform are available for use in control algorithm. It is known that these signals can be obtained from one another by differentiation and integration and measurement of both signals may seem redundant. However, studies also shows that this is not the case.

As it is the case with almost all control applications, both feedback signals are contaminated with noise and need filtering. At this point, instead of applying separate low-pass filters to these feedback signals, both signals are combined in a single Kalman filter. Section 3.2 starts with the inspection of validity conditions for Kalman filter optimality for the application at hand and later continues with the implementation of the filter. It is shown that with the additional measurement of acceleration signal, a great improvement in both velocity and acceleration feedback quality is achieved when compared with the velocity-only measurement case. The improvement in acceleration signal is intuitive since with direct measurement of the acceleration, delays originating from heavy filtering of the otherwise obtained signal from the differentiation of velocity are discarded. However, experiments show that the resulting velocity signal also gets better with usage of acceleration measurement, in the sense that noise on the velocity signal can be reduced greatly with this additional information, making further filtering unnecessary.

In Section 2.2, a full mathematical model of the 2-DOF gimbal is derived starting

from the three dimensional Newton-Euler equations. This detailed model includes all possible disturbance terms, unbalance effects and inertial terms that develop as a result of relative motions of the two gimbal axes. However, such a detailed model results in very complex equations of motion and therefore needs to be simplified in order to be suitable for usage in controller design phase. Therefore, Section 2.2 continues with this simplification process and it is shown that recognizing the 2-DOF gimbal platform as two separate uncoupled axes is possible. Later work on controller design is based on this simplified model.

Based on this simplified model, three different controllers that utilize acceleration feedback are designed. First one of these controllers tries to improve the stabilization accuracy by making use of a load torque estimator, which uses Newton's second law of motion to calculate the disturbance torque on the system from acceleration and motor torque signals. Calculated disturbance torque is added to the torque command in order to compensate for the actual disturbance torques.

A second method relies on improved disturbance rejection characteristics achieved with a fast inner acceleration loop inside the present velocity loop. Effects of any disturbance torque is first sensed in the acceleration signal before any significant velocity error can build up and velocity controller can respond to it. A fast acceleration loop therefore can respond faster and reduce stabilization errors.

Finally, a last method is proposed which is similar to the second method but this time acceleration is used in a state feedback structure. To be more precise, an optimal controller which is very much similar to the LQR is formulated. This new optimal controller, called as the state derivative feedback LQR, uses the acceleration, velocity, and position feedbacks in order to produce the optimal controller output that will stabilize the platform.

All three controllers are compared with a standard controller that uses angular velocity feedback only. Comparisons are done on both simulation model and experimental setup. Simulation model of the setup is created using Matlab/Simulink software, making use of SimMechanics blockset for modeling the physical system. Both in the simulation model and experimental setup yaw and pitch motions are given to the base of the gimbal which is mounted on the 6-DOF motion simulator and the gimbal

is stabilized under these disturbances. This is done for azimuth and elevation axes separately and the amount of angular deviation from the intended position, which is defined as the stabilization error, is recorded as a function of time for all tests.

In tests done, the main source of disturbance is the friction torques originating from relative motion of gimbal axes in the course of stabilization. However, the effects of unbalanced mass center is also recognized as an important source of disturbance in results obtained from elevation axis test done on the experimental setup. Even though a pure rotational disturbance around the center of rotation is tried to be given by the motion simulator, the effects of COG not being on the axis of rotation cannot be fully negated. This is also the explanation for the somewhat larger discrepancy between simulation and experimental tests results obtained for the elevation axis.

In Section 3.1.4, "Friction to System Inertia Ratio" is defined as an important index related to the achievable stabilization performance for a mechanical system. A lower ratio means that the system will inherently perform better in stabilization applications, independent from the controller used. This is indeed confirmed in tests, especially in simulation tests where friction is the only source of disturbance. Elevation axis which has a lower friction to inertia ratio performs much better than the azimuth axis for all disturbance profiles.

Other than the already mentioned linear acceleration effects in elevation axis tests, simulation runs and experimental tests give comparable results, especially for frequencies in the range of 1-5 Hz. This also confirms the validity of the simulation model built. Higher and lower frequency tests show somewhat larger differences but again even at these frequencies differences are not great and general trends in both simulation and experimental tests are in agreement. Sections 3.5 and 4.3 gives details of tests done on simulation model and experimental setup, respectively.

Assessment of performances of the different controllers can be done by looking at the results of these tests. To start with, it is important to note that stabilization accuracies obtained even with the standard controller are very good considering the heavy disturbance profiles that are applied to the system. This is partially due to the superior mechanical design of the gimbal platform and high quality sensors used in the application. However it should be noted that the improvement achieved in the velocity

signal with sensor fusion, as discussed in Section 3.2.4, is another factor improving the stabilization performance of the base controller.

Improvements achieved by the usage of acceleration feedback can be seen from both simulation and experimental test results clearly. All three methods achieve some improvement while the amount of improvement changes from method to method. Although better than the standard controller, the load torque observer method results in the smallest of improvements. The reason for the limited performance is considered to be the filtering required to remove the high noise content resulting from the direct feed-forward of the estimated load torque.

Methods such as the inner acceleration loop and state derivative feedback LQR which use the acceleration signal in a feedback structure proves to be better, achieving even smaller errors. Among these two, state derivative feedback LQR results in better stabilization accuracies in both azimuth and elevation axes. However, this higher accuracies comes with slightly reduced stability margins, which can be seen from the open loop Bode plots given in Section 3.4.

Tests conducted on the experimental setup showed that stabilization accuracies better than 20 μrad can be achieved with the last two methods. When similar gimbal platforms that are being used in military applications listed in Chapter 1 are investigated, it is seen that a stabilization accuracy this high cannot be reached even with the highest performance systems showing that acceleration feedback methods used are extremely successful.

In conclusion, it is shown that measurement and use of angular acceleration of a stabilized platform greatly improves the stabilization performance once the system meets certain specifications such as high structural rigidity, no backlash or very low backlash in the driveline, low noise and delay in sensor measurements etc. which are also key requirements for designing high performance stabilized platforms. Therefore, instead of very high cost methods such as two-stage stabilization or use of very sensitive navigation grade sensing equipment, measurement and usage of angular acceleration can be utilized for achieving the highest grade stabilization required for these extremely demanding applications.

5.2 Future Work

Use of linear accelerometers is advantageous for measuring the angular acceleration of the platform for the reasons given in Section 2.1. Depending on the platform and disturbance profiles the platform will be subjected to, certain problems can be experienced with linear accelerometers used.

The most important of these problems is the sensor saturation problem. Equations starting from 2.44 through 2.46 gives the expressions for angular accelerations of the platform. Note that each angular acceleration term is the summation of four linear accelerations directly measured from linear accelerometers. In case any of these accelerometers are saturated, this will cause the angular acceleration calculation not to be saturated but to be wrong. Furthermore, for platforms such as the ones mounted on land vehicles, very high linear accelerations may exist on the system, causing one or more sensors saturate. In order to avoid this, very high measurement range sensors must be selected but high range sensors have the disadvantage of higher noise. Therefore a net degradation in performance is inevitable in platforms where high linear accelerations are present.

In order to avoid these problems, the usage of angular accelerometers should also be investigated as a future work. These sensors use completely different technologies for measuring angular accelerations and they are not effected by linear accelerations, making them suitable for use in environments described above. Instrumentation and integration of such sensors should be done on the test platform and similar test should be repeated with these sensor. Performance assessment can later be done by looking at the results obtained and if satisfactory results are obtained use of such sensors can be considered a viable option, too.

REFERENCES

[1] Mitsutomi, T., *"Characteristics and Stabilization of an Inertial Platform"*, IRE Transactions on Aeronautical and Navigational Electronics, Vol. ANE-5, Issue 2, 1958.

[2] Bigley, W. J., *"Wideband Base Motion Isolation Control for a Mobile Platform"*, Proceedings of the American Control Conference, 1987.

[3] Benett, W. H. and Musser, K., *"Pointing and Stabilization of Weapon Platforms"*, Proceedings of the American Control Conference, San Francisco, CA, 1993.

[4] Ovaska, S. J. and Valiviita, S., *"Angular Acceleration Measurement: A Review"*, Proceedings of the IEEE Instrumentation and Measurement Technology Conference, St. Paul, Minnesota, 18-21 May 1998.

[5] Hori, Y., *"Disturbance Suppression On an Acceleration Control Type DC Servo System"*, 19th Annual IEEE Power Electronics Specialists Conference, 1988.

[6] Hori, Y., *"Position and Mechanical Impedance Control Method of Robot Actuators Based on the Acceleration Control"*, 20th Annual IEEE Power Electronics Specialists Conference, 1989.

[7] Schmidt, P. B. and Lorenz, R. D., *"Design Principles and Implementation of Acceleration Feedback to Improve Performance of dc Drives"*, IEEE Transactions on Industry Applications, Vol 28, No 3, May/June 1992.

[8] Komada, S., Ishida, M., Ohnishi, K., and Hori, T., *"Disturbance Observer-Based Motion Control of Direct Drive Motors"*, IEEE Transactions on Energy Conversion, September 1991.

[9] Ginsberg, J. H., *Advanced Engineering Dynamics*, Second Edition, Cambridge University Press, New York, 1998.

[10] Nusholtz, G. S., *"Geometric Methods in Determining Rigid-body Dynamics"*, Experimental Mechanics, June 1993.

[11] Cardou, P. and Angeles, J., *"Angular Velocity Estimation From the Angular Acceleration Matrix"*, ASME Journal of Applied Mechanics, Vol. 75, March 2008.

[12] Cardou, P. and Angeles, J., *"Linear Estimation of the Rigid-Body Acceleration Field From Point-Acceleration Measurements"*, ASME Journal of Dynamic Systems, Measurement and Control, Vol. 131, July 2009.

[13] Genin, J., Hong, J., and Xu, W., *"Accelerometer Placement for Angular Velocity Determination"*, Transactions of the ASME, Vol. 119, September 1997.

[14] Costello, M. and Jitpraphai, T., *"Determining Angular Velocity and Angular Acceleration of Projectiles Using Triaxial Acceleration Measurements"*, Journal of Spacecraft and Rockets, Vol. 39, No. 1, January-February 2002.

[15] Zappa, B., Legnani, G., van den Bogert, A. J., and Adamini, R., *"On the Number and Placement of Accelerometers for Angular Velocity and Acceleration Determination"*, Transactions of the ASME, Vol. 123, September 2001.

[16] Qin, Z., Baron, L., and Birglen, L., *"Robust Design of Inertial Measurement Units Based on Accelerometers"*, ASME Journal of Dynamic Systems, Measurement and Control, Vol. 131, May 2009.

[17] Padgaonkar, A. J., Krieger, K. W., and King, A. I., *Measurement of Angular Acceleration of a Rigid Body Using Linear Accelerometers"*, Transactions of the ASME, September 1975.

[18] Waldmann, J., *"Line-of-Sight Rate Estimation and Linearization Control of an Imaging Seeker in a Tactical Missile Guided by Proportional Navigation"*, IEEE Transactions on Control Systems Technology, Vol. 10, No. 4, July 2002.

[19] Kennedy, P. J. and Kennedy, R. L., *"Direct Versus Indirect Line of Sight (LOS) Stabilization"*, IEEE Transactions on Control Systems Technology, Vol. 11, No. 1, January 2003.

[20] Perez, C., Rubio, F. R., *"Implementation of an Inertial Controller for a 2-DOF Platform"*, Proceedings of the 2001 IEEE International Conference on Control Applications, Mexico City, Mexico, September 5-7 2001.

[21] Simon, D., *Optimal State Estimation*, John Wiley and Sons Inc., New Jersey, 2006.

[22] Han, Y., Lu, Y., and Qiu, H., *"An Improved Control Scheme of Gyro Stabilization Electro-Optical Platform"*, Proceedings of the IEEE International Conference on Control and Automation, Guangzhou, China, May 30-June 1, 2007.

[23] de Joger, B., *"Acceleration Assisted Tracking Control"*, IEEE Control Systems, October 1994.

[24] Deur, J., *"A Comparative Study of Servosystems with Acceleration Feedback"*, Proceedings of IEEE IAS, 2000.

[25] Kobayashi, H., Katsura, S., and Ohnishi, K., *"An Analysis of Parameter Variations of Disturbance Observer for Motion Control"*, IEEE Transactions on Industrial Electronics, Vol. 54, No. 6, December 2007.

[26] Katsura, S., Irie, K., and Ohnishi, K., *"Wideband Force Control by Position-Acceleration Integrated Disturbance Observer"*, IEEE Transactions on Industrial Electronics, Vol. 55, No. 4, April 2008.

[27] Han, J. D., He, Y. Q., and XU, W. L., *"Angular Acceleration Estimation and Feedback Control: An Experimental Investigation"*, Mechatronics, Vol. 17, Issue 9, November 2007.

[28] Tan, K. K., Lim, S. Y., Lee, T. H., and Dou, H., *"High-Precision Control of Linear Actuators Incorporating Acceleration Sensing"*, Robotics and Computer-Integrated Manufacturing, Vol. 16, Issue 5, October 2000.

[29] Anderson, B. D. O. and Moore, J. B., *Optimal Control: Linear Quadratic Methods*, Prentice-Hall Inc., New Jersey, 1989.

[30] Kirk, D. E., *Optimal Control Theory: An Introduction*, Prentice-Hall Inc., New Jersey, 1970.

[31] Ogata, K., *Modern Control Engineering*, Fourth Edition, Prentice-Hall Inc., New Jersey, 2002.

[32] Tseng, Y. W. and Yedavalli, R. K., *"Control Design of Linear Dynamic System with Matrix Differential Equations for Aerospace Applications"*, Columbus: The Ohio State University, 1997.

[33] Yedevalli, R. K., Tseng, Y. W., Kbot, N. S., and Veley, D., *"Aeroelastic Control Using Smart Structures and Acceleration Feedback"*, Presented at Smart Strucutres and Materials, San Diego, CA, 1997.

[34] Kwak, S. K., Washington, G., and Yedevalli, R. K., *"Full State Derivative Feedback Control Based on the Reciprocal State Space Framework Using Smart Materials"*, Proceedings of SPIE, Vol. 3984, 2000.

[35] Abdelaziz, T. H. S. and Valasek, M., *"State Derivative Feedback by LQR for Linear Time-Invariant Systems"*, Proceedings of the 16th IFAC World Congress, Vol. 16, Part 1, 2005.

[36] Schlotter, M., *"Multibody System Simulation with SimMechanics"*, May 2003.

[37] Aerotech, Inc., www.aerotech.com, last visited in July 2010.

[38] Elmo Motion Control Ltd., www.elmomc.com, last visited in July 2010.